

國立臺灣大學工學院化學工程學研究所



碩士論文

Department of Chemical Engineering

College of Engineering

National Taiwan University

Master Thesis

金屬沸石咪唑骨架材料衍生物應用於

染料敏化太陽能電池及超級電容器

Zeolitic Imidazolate Framework-derived Composite Materials
for Dye-sensitized Solar Cells and Supercapacitors

簡秀玲

Siou-Ling Jian

指導教授：何國川 博士

Advisor: Kuo-Chuan Ho, Ph.D.

中華民國 107 年 6 月

June, 2018

**Zeolitic Imidazolate Framework-derived Composite Materials
for Dye-sensitized Solar Cells and Supercapacitors**

by

Siou-Ling Jian



A thesis submitted to the
National Taiwan University
for the degree of **Master**

Supervised by

Professor Kuo-Chuan Ho

Department of Chemical Engineering

College of Engineering

National Taiwan University

Taipei, Taiwan

June, 2018

致謝



感謝我的指導教授何國川老師當初願意讓學生進入實驗室學習，在何老師實驗室有機會完成許多具有挑戰性的研究，不論是實驗室 seminar 以英文報告實驗成果，或是出國參加國際研討會，讓學生在這過程中學習與成長了許多。感謝老師在研究上給予學生完全的支持，透過老師的指導，讓學生學習到如何以正確的態度從事研究工作，也要感謝老師鼓勵我們參加國際研討會，這些經驗大幅提升學生的國際視野。

感謝台大應力所陳建彰教授、北科大化工林律吟教授、北市大應用物化系李權倍教授百忙之中撥冗擔任論文口試委員，因您們的指導與建議，得以讓此篇論文更加完備。

感謝台大化工系光電材料研究室的諸位學長姐們(Dr. Vittal、Dr. Sydam、旻鑫、廷祥、妙璇、奕鈞、鑫福、芳賢、昕則、旻翰、馮浩、怡琳、奕廷)在 seminar 上提供意見與討論，讓我的研究能夠更加完整。感謝仲偉學長、權倍學長、君婷學姊與宜鋒學長願意分享他們的經驗與知識為我解惑。也感謝研究上一起努力的同屆同學彥鈞、力尹、偉婷，在研究與生活上的協助與討論。感謝承泰、皓禎、泰螢、彥安、皓瑋、旻軒、柏勳、程勛、冠逸、語彤、書銘、漢庭、芳宇、宣百、宛霓平時在實驗室討論會中和大家分享與討論研究成果，讓我學到更多自身研究主題外的學術知識。

最後要感謝我的父母在我的求學生涯中，不斷地給予我支持與鼓勵，你們一路上的支持是我求學生涯中最重要的精神支柱。之後我會懷著這份感恩繼續努力，迎接下一個人生階段。謹以此論文獻給我摯愛的家人，以及所有曾經幫助過我的同仁們。

簡秀玲

2018 年 6 月

中文摘要

本論文旨在研究金屬沸石咪唑骨架材料衍生物作為電極材料，用以發展低成本、高性能的能源領域(染料敏化太陽能電池和超級電容器)。本論文主要分為兩大部分：金屬沸石咪唑骨架衍生之硒化鋅摻雜氮碳材複合物作為對電極應用於染敏電池(第三章)，和奈米碳管/金屬沸石咪唑骨架衍生之硫化鈷複合材料應用於超級電容器(第四章)。

在第三章中，以金屬沸石咪唑骨架衍生之硒化鋅摻雜氮碳材複合物作為染敏電池電催化材料，其表現出極佳的電催化特性和導電性。利用不同的碳化溫度及硒化溫度來合成金屬沸石咪唑骨架衍生複合材料，分別克服材料之導電性不佳的缺點和提升其電催化性。在此複合材料中，金屬沸石咪唑骨架碳化後之氮摻雜碳材有利於電催化及電子傳導；同時，鑲嵌在碳材中的硒化鋅則扮演加速催化三碘化物離子之活性催化點。最適化後之複合材料，其光電轉化效率為 8.69%，高於傳統使用的鉑對電極(8.26%)。而在較弱光強度下，此複合材料仍有 7.99%的光電轉換效率。此研究成果顯示此複合材料具有作為染敏電池之電觸媒的潛力。

在第四章中，合成了奈米碳管/金屬沸石咪唑骨架衍生之硫化鈷奈米複合材料作為超級電容器之電極材料。利用不同濃度的奈米碳管和金屬沸石咪唑骨架之前驅物合成不同粒徑大小的複合物。經過硫化過後，此奈米複合材料能同時具備高導電性及良好的電化學特性。此奈米複合材料中，奈米碳管扮演電子快速傳遞的通道，克服了硫化鈷導電性不佳的缺點。電化學實驗結果顯示，其可在 5 A g^{-1} 的充放電電流密度下達到 2173 F g^{-1} 的比電容值，同時在 1000 圈的充放電循環後，仍可維持 91%的初始比電容值，顯示此奈米複合材料具有作為超級電容器之電極材料的潛力。

關鍵詞： 硫化鈷、染料敏化太陽能電池、電觸媒、超級電容器、金屬沸石咪唑骨架、硒化鋅。

Abstract

This thesis mainly focuses on two different but related parts, namely, discussing about the application of a zeolitic imidazolate framework-derived ZnSe/N-doped carbon cube hybrid electrocatalyst as the counter electrode for dye-sensitized solar cells (Chapter 3) and carbon nanotube/zeolitic imidazolate framework-derived cobalt sulfide hybrid composites for supercapacitors (Chapter 4). The overview of these two applications will be displayed in introduction (**Chapter 1**). Moreover, the experimental procedures (**Chapter 2**) includes the chemical reagent, material characterization and the principle of electrochemical analysis.

In Chapter 3, a zinc selenide decorated N-doped carbonaceous hybrid material (ZIF-ZnSe-NC) derived from a zeolitic imidazolate framework (ZIF-7) used as the electrocatalyst for the counter electrode in DSSCs exhibited excellent electrocatalytic performance and electrical conductivity. Carbonization and selenization at different temperatures for synthesizing ZIF-ZnSe-NC electrocatalyst were carried out step by step to enhance the electrocatalytic performance and electrical conductivity of the material. In the ZIF-ZnSe-NC hybrid electrocatalyst, the N-doped carbon cube is beneficial to the electrocatalytic performance and the electrical conductivity. Meanwhile, embedded ZnSe in the carbon matrix also serves as the additional active site for facilitating I_3^- reduction. The DSSCs with the optimized ZIF-ZnSe-NC-11 wt% CEs exhibited a photovoltaic conversion efficiency (η) of $8.69 \pm 0.13\%$, which is higher than that of the cells with Pt CEs ($8.26 \pm 0.02\%$). A reasonable cell efficiency of $7.99 \pm 0.01\%$ was still attained for the DSSCs with CEs of ZIF-ZnSe-NC-11 wt% at a dim light intensity of 10 mW cm^{-2} . Thus, it could be concluded that the ZIF-ZnSe-NC is a promising material to replace the expensive Pt in DSSCs, especially for the indoor application.

In Chapter 4, a hybrid structure of carbon nanotubes interconnected zeolitic imidazolate framework (ZIF) derived cobalt sulfide (CNT/CoS) nanocage was designed and synthesized as the electrode material in SCs. The carbon nanotubes/ZIF-67 (CNT/ZIF-67) nanocomposites with

controlled ZIF-67 particle sizes have been systematically studied by varying the mass ratio of CNT to ZIF-67 under reaction process, then followed by subsequent sulfurization with thioacetamide. Benefiting from the porous nanocage architecture and conductive CNTs, the optimized CNT/CoS nanocage exhibits excellent electrochemical performance with an outstanding specific capacitance (2173.1 F g^{-1} at 5 A g^{-1}), good rate capacity (65% retention at 20 A g^{-1}), and long-term stability (91% retention over 1000 cycles), demonstrating a great potential in energy applications. The method developed in this work can be extended to the construction of other metal sulfide electrode materials for a variety of energy storage applications.

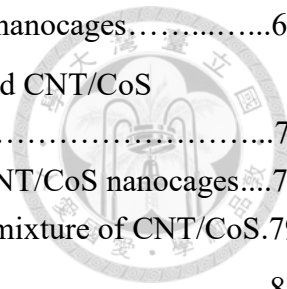
Keywords: cobalt sulfide, dye-sensitized solar cell, electrocatalyst, supercapacitor, zeolitic imidazolate framework, zinc selenide.

Table of contents



致謝.....	I
中文摘要.....	II
Abstract	III
Table of contents.....	V
List of tables.....	VIII
List of figures.....	IX
Chapter 1 Introduction.....	1
1-1 Overview of zeolitic imidazolate framework (ZIFs).....	1
1-2 Introduction of dye-sensitized solar cells (DSSCs).....	6
1-2-1 Counter electrodes (CEs) in DSSCs.....	11
1-3 Introduction of supercapacitors (SCs).....	16
1-4 Motivation and scope of this thesis.....	20
Chapter 2 Experimental procedures.....	22
2-1 Materials.....	22
2-2 Experiments relating to a zeolitic imidazolate framework-derived ZnSe/N-doped carbon cube hybrid electrocatalyst as the counter electrode for dye-sensitized solar cells.....	23
2-2-1 Synthesis of ZIF-7 and ZIF-7-derived catalysts.....	23
2-2-2 Preparation of counter electrodes.....	24
2-2-3 Preparation of photoanode and the DSSC assembly.....	24
2-3 Experiments relating to designing a carbon nanotube interconnected ZIF-derived cobalt sulfide nanocage for supercapacitors.....	25
2-3-1 Synthesis of ZIF-67, CNT/ZIF-67 nanocomposite, and hybrid CNT/CoS nanocage.....	25
2-3-2 Preparation of electrode with electroactive materials for SCs.....	26

2-4 Analytic techniques.....	27
2-4-1 Material characterizations.....	27
2-4-2 Photovoltaic properties for DSSCs.....	27
2-4-3 Electrochemical properties for DSSCs.....	30
2-4-4 Electrochemical properties for SCs.....	33
Chapter 3 A zeolitic imidazolate framework-derived ZnSe/N-doped carbon cube hybrid electrocatalyst as the counter electrode for dye-sensitized solar cells.....	34
3-1 Introduction and motivation.....	34
3-2 Results and discussions.....	39
3-2-1 Characterization of the as-synthesized ZIF-7.....	39
3-2-2 Characterization of carbonized ZIF-7 at various calcination temperatures	40
3-2-3 Characterization of the selenized ZIF-NC at various calcination temperatures	45
3-2-4 Electrochemical analyses of ZIF-7 and ZIF-derived materials.....	47
3-2-5 Optimization of the ZIF-ZnSe-NC weight percentage for a highly efficient counter electrode.....	50
3-2-6 Comparison of DSSCs with CEs of commercial Pt and the optimized ZIF-ZnSe- NC.....	53
3-3 Conclusions.....	59
Chapter 4 Designing a carbon nanotube interconnected ZIF-derived cobalt sulfide nanocage for supercapacitors.....	60
4-1 Introduction and motivation.....	60
4-2 Results and discussions.....	63
4-2-1 Characterization of the as-synthesized ZIF-67.....	63
4-2-2 Characterization of CNT/ZIF-67 nanocomposites.....	65



4-2-3 Characterization of CoS nanocage and hybrid CNT/CoS nanocages.....	67
4-2-4 Electrochemical performance of CoS nanocage and hybrid CNT/CoS nanocages.....	71
4-2-5 Electrochemical analyses of CoS nanocage and hybrid CNT/CoS nanocages....	77
4-2-6 Comparison of hybrid CNT/CoS nanocage and physical mixture of CNT/CoS.	79
4-3 Conclusions.....	85
Chapter 5 Conclusions and suggestions.....	86
5-1 General conclusions.....	86
5-2 Suggestions.....	86
5-2-1 Suggestions for Chapter 3.....	86
5-2-2 Suggestions for Chapter 4.....	87
References.....	88

List of tables

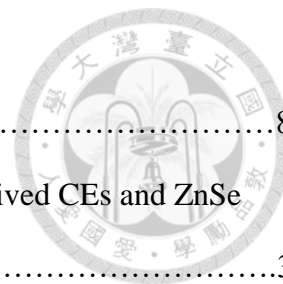
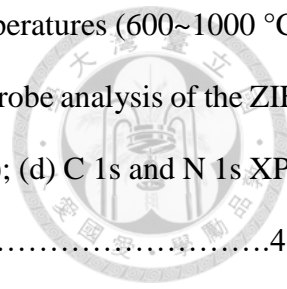


Table 1-1 The mechanism and related chemical reaction of a DSSC.....	8
Table 3-1 The performance of the reported DSSCs using various ZIF-derived CEs and ZnSe CEs, as compared to that obtained in this work.....	38
Table 3-2 The photovoltaic parameters of the DSSCs with ZIF-NC CEs prepared under different carbonization temperatures, measured at 100 mW cm^{-2}	43
Table 3-3 The photovoltaic parameters of the DSSCs with ZIF-ZnSe-NC CEs prepared under different selenization temperatures, measured at 100 mW cm^{-2}	47
Table 3-4 The photovoltaic parameters of the DSSCs with various CEs of ZIF-7, ZIF-NC, and ZIF-ZnSe-NC, measured at 100 mW cm^{-2}	49
Table 3-5 The photovoltaic parameters of the DSSCs with ZIF-ZnSe-NC CEs under different slurry concentrations (5~13 wt%), measured at 100 mW cm^{-2}	53
Table 3-6 The photovoltaic parameters of the DSSCs with CEs of ZIF-ZnSe-NC-11 wt% and Pt, measured at 100 mW cm^{-2}	56
Table 3-7 The electrochemical parameters <i>via</i> CV and RDE; charge transfer parameters <i>via</i> EIS and Tafel for the electrocatalytic films of ZIF-ZnSe-NC-11 wt% and Pt.....	56
Table 3-8 The photovoltaic parameters of the DSSCs with the CEs of ZIF-ZnSe-NC-11 wt% and Pt, measured under $10\text{-}100 \text{ mW cm}^{-2}$	58
Table 4-1 A list of MOF-derived cobalt sulfide and carbon/cobalt sulfide materials in the application of supercapacitors, compared to that obtained in this work.....	82

List of figures



Figure 1-1 The bridging angles in ZIFs (left) and zeolites (right).....	2
Figure 1-2 The imidazolate linkers used in ZIFs.....	2
Figure 1-3 Crystal structures of ZIFs grouped according to their topology.....	3
Figure 1-4 (a) The corresponding particle sizes of the ZIF-90 materials synthesized in different systems, and (b) the measured viscosity of each H ₂ O/alcohol system.....	4
Figure 1-5 The cell constructions and mechanisms involved in a DSSC.....	8
Figure 1-6 The categories of the electrocatalysts as CEs in DSSCs.....	12
Figure 1-7 The transition metallic cations (blue part) and the anions (green part with black line) that can be combined to prepare the TMC type CEs for the DSSCs.....	15
Fig. 1-8 Specific power against specific energy, also called a Ragone plot, for various electrical energy storage devices.....	17
Figure 1-9 Schematic illustration of the charge and discharge of electrochemical double layer capacitor.....	18
Figure 1-10 Schematic representation of electrical double layer structures according to (a) the Helmholtz model, (b) the Gouy-Chapman model, and (c) the GouyChapman-Stern model.....	19
Figure 1-11 The flowchart of this thesis.....	20
Figure 2-1 Air mass (AM) definition and the equation corresponding to zenith angle.....	28
Figure 2-2 Illustrate the parameters of the <i>J-V</i> curves.....	29
Figure 2-3 The equivalent circuit of a symmetric cell of an electrocatalytic film.....	32
Figure 3-1 The sketch of the process from ZIF-7 to ZIF-derived materials.....	37
Figure 3-2 (a) Schematic illustration, (b) FE-SEM image, (c) XRD pattern, and (d) N ₂ adsorption-desorption isotherms of as-synthesized ZIF-7.....	39
Figure 3-3 (a) TGA plot of ZIF-7 at a temperature rate of 10 °C min ⁻¹ in an N ₂ atmosphere; the	



pictures of ZIF-NC powder with different carbonization temperatures (600~1000 °C) are shown in the inset; (b) Raman spectra and (c) four-point probe analysis of the ZIF-NC with different carbonization temperatures (600~1000 °C); (d) C 1s and N 1s XPS spectra of ZIF-NC-900 °C.....41

Figure 3-4 (a) N₂ adsorption-desorption isotherms and (b) XRD pattern of ZIF-NC-900 °C powder42

Figure 3-5 (a) Photocurrent density-voltage curves of the DSSCs with the CEs of different carbonization temperatures (600~1000 °C) of ZIF-NC films, (b) FE-SEM images of ZIF-NC-900 °C and ZIF-NC-1000 °C.....44

Figure 3-6 (a) XPS survey scan of ZIF-NC before and after selenization at 450 °C, and XPS of ZIF-NC after selenization for Se 3d spectra; (b) XRD patterns and (c) EDS analysis on the weight percentage of ZIF-ZnSe-NC with different selenization temperatures (300~600 °C); (d) *J-V* curves of the DSSCs with the CEs of ZIF-ZnSe-NC under different selenization temperatures (300~600 °C).....46

Figure 3-7 (a) *J-V* curves of the DSSCs with the CEs of ZIF-7, ZIF-NC, and ZIF-ZnSe-NC; (b) K-L plots for ZIF-7, ZIF-NC, and ZIF-ZnSe-NC composite electrodes.....49

Figure 3-8 (a) FE-SEM images of the ZIF-ZnSe-NC films with different weight percentages of ZIF-ZnSe-NC (5~13 wt%) and pristine ZIF-ZnSe-NC film (W/O: without PEDOT:PSS); (b) *J-V* curves and (c) Photovoltaic parameters of the DSSCs with the CEs of ZIF-ZnSe-NC films with different weight percentages (5~13 wt%).....51

Figure 3-9 (a) EDS spectrum, and (b) the corresponding EDS elemental mapping images of ZIF-ZnSe-NC-11 wt% film.....52

Figure 3-10 (a) *J-V* curves of the DSSCs with the CEs of ZIF-ZnSe-NC-11 wt% and Pt (inset: IPCE curves of the corresponding devices); (b) CV curves, (c) K-L plots, and (d) EIS spectra (inset: Tafel polarization plots) of the electrodes with ZIF-ZnSe-NC-11 wt% and

Pt.....	55
Figure 3-11 <i>J-V</i> curves of the DSSCs with the CEs of (a) ZIF-ZnSe-NC-11 wt% and (b) Pt under different incident light intensities (10~100 mW cm ⁻²).....	57
Figure 4-1 Schematic illustration of the synthesis of CNT/CoS nanocages.....	62
Figure 4-2 (a) Schematic illustration, (b) FE-SEM image, (c) XRD pattern, and (d) N ₂ adsorption-desorption isotherms (inset: pore size distribution) of as-synthesized ZIF-67.....	64
Figure 4-3 (a) FE-SEM image of CNT and CNT/ZIF-67 nanocomposites with different mass ratios of CNT to ZIF-67, (b) growth schematic and (c) XRD patterns of ZIF-67 crystal size with different ratio of CNT to ZIF-67.....	66
Figure 4-4 (a) FE-SEM image of CoS nanocage and hybrid CNT/CoS nanocages with various sizes of ZIF-67 as templates, (b) XPS spectra of Co 2p and S 2p for CNT/CoS 1:2 nanocages, and (c) N ₂ adsorption-desorption isotherms of CoS nanocage and CNT/CoS 1:2 nanocages.....	68
Figure 4-5 FE-SEM images of (a) ZIF-67 nanoparticles, and (b) CoS nanocages.....	69
Figure 4-6 The schematic illustration of the collapsed CoS via sulfurization.....	69
Figure 4-7 XRD patterns of CoS cage and hybrid CNT/CoS nanocages with various sizes of ZIF-67 as templates.....	70
Figure 4-8 (a) Cyclic voltammograms (CVs) at a scan rate of 100 mV s ⁻¹ , (b) galvanostatic charge-discharge (GCD) curves at a current density of 5 A g ⁻¹ of CoS, CNT/CoS 1:1, CNT/CoS 1:2, and CNT/CoS 1:8 nanocage electrodes, (c) CVs of CNT/CoS 1:2 electrodes at different scanning rates, (d) GCD curves of CNT/CoS 1:2 nanocage electrodes at different current densities, (e) comparison of the specific capacitance performance of CoS, CNT/CoS 1:1, CNT/CoS 1:2, and CNT/CoS 1:8 nanocage electrodes at a current density of 5 A g ⁻¹ , and (f) comparison of the specific capacitance values at various current densities of the nanocages.....	74

Figure 4-9 CVs of (a) CoS nanocage, (b) CNT/CoS 1:1 nanocage, (c) CNT/CoS 1:8 nanocage, and (d) CNT/CoS mixture electrodes at different scan rates.....75

Figure 4-10 GCD curves of (a) CoS nanocage, (b) CNT/CoS 1:1 nanocage, (c) CNT/CoS 1:8 nanocage, and (d) CNT/CoS mixture electrodes at different current densities.....76

Figure 4-11 (a) Nyquist plots (magnified plot in high frequency range and electrical equivalent circuit was also included as the inset), and (b) R_{ct} values of CoS, CNT/CoS 1:1, CNT/CoS 1:2 and CNT/CoS 1:8 nanocages with the frequency range from 100 kHz to 0.1 Hz.....78

Figure 4-12 (a) FE-SEM image, (b) GCD curves, (c) Nyquist plots, (d) cycling performance of CNT/CoS nanocage and CNT/CoS mixture nanocages, and (e) Ragone plot of CoS nanocage, CNT/CoS nanocage and CNT/CoS mixture under various current densities.81

Chapter 1

Introduction



1-1 Overview of Zeolitic imidazolate frameworks (ZIFs)

For a long time, porous materials have continuously been the research focus not only in fundamental investigations but also in practical applications due to their intrinsic properties such as high surface areas, large pore volumes and tuneable pore sizes.¹ During the last decade, much effort has been devoted to developing a new class of porous materials based on hybrid metal-organic frameworks (MOFs). The term MOFs was introduced for the first time by Yaghi and his co-workers in 1995.² MOFs are constructed by joining metal-containing units with organic linkers, using strong bonds (reticular synthesis) to create open crystalline frameworks with permanent porosity. MOFs have rapidly developed by the prospects of finding new structures, enhancing their functionalities, exploring new gas sorption and catalytic properties and expanding pore sizes.

Recently, Zeolitic imidazolate frameworks (ZIFs) as a subclass of MOFs have attracted large scientific interests due to their high porosity, excellent mechanical stability, tunable surface properties, and their exceptional chemical and thermal stabilities.³ ZIFs are a class of porous crystals with extended three-dimensional structures constructed from tetrahedral metal ions (*e.g.*, Zn, Co) bridged by imidazolate (Im). The fact that the M-Im-M angle is similar to the Si-O-Si angle (145°) (**Figure 1-1**) preferred in zeolites has led to the synthesis of a large number of ZIFs with zeolite-type tetrahedral topologies. **Figure 1-2** shows the various imidazolate linkers used in ZIFs. The synthesis of ZIFs essentially depends on the coordination ability of the metal centers and organic linkers, which offers a greater flexibility and controllability than conventional zeolites. The pore size and the adsorption properties of ZIFs can be tailored by changing or chemically modifying the anionic imidazolate linker. As of today, more than 90 ZIF structures have been reported, some of which share the same topology as zeolites, while others exhibit crystal structures which are different from

zeolites.⁴ A variety of ZIFs have been synthesized that possess the zeolite topologies ANA, BCT, DFT, GIS, GME, LTA, MER, RHO and SOD, as shown in **Figure 1-3**.

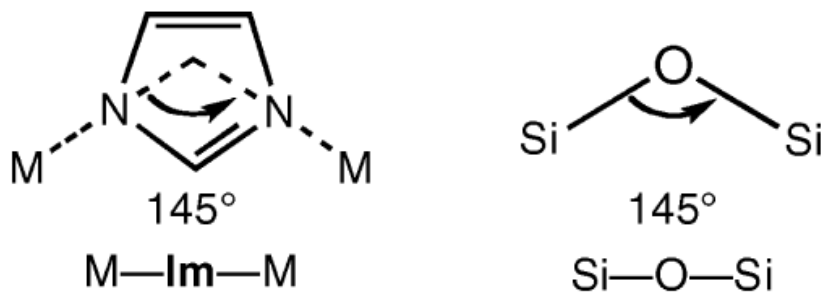


Figure 1-1 The bridging angles in ZIFs (left) and zeolites (right).⁵

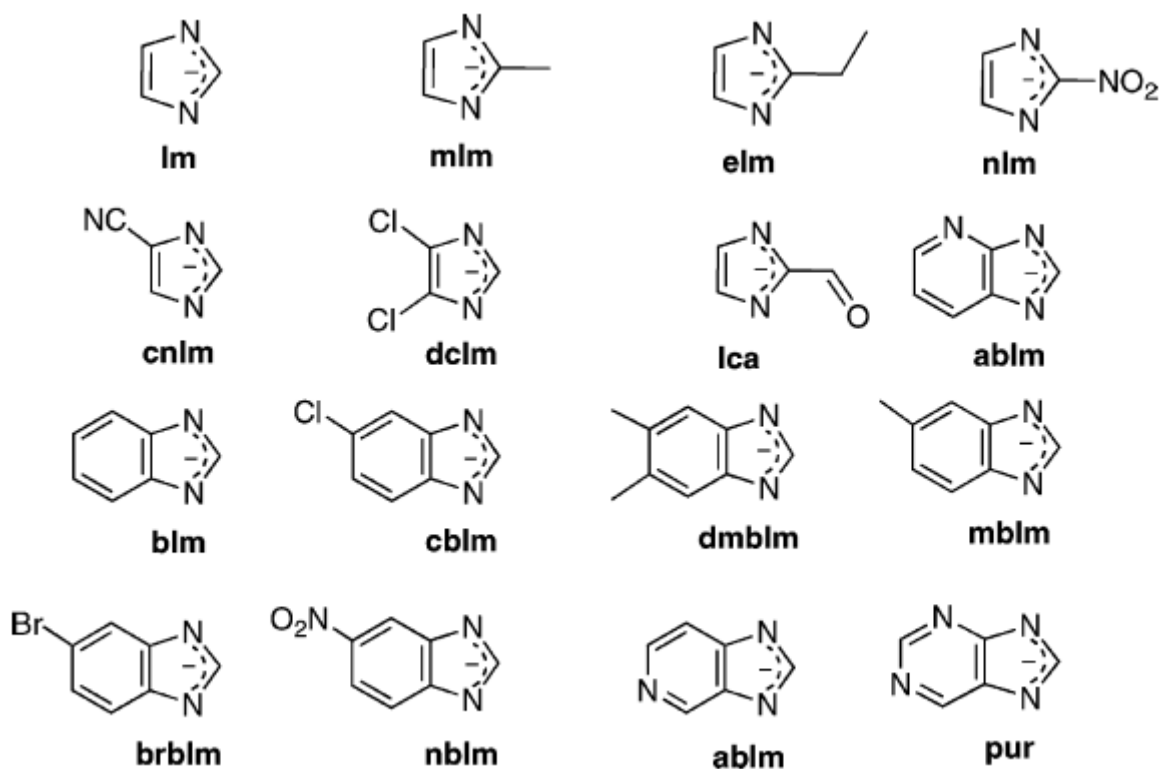


Figure 1-2 The imidazolate linkers used in ZIFs.⁵

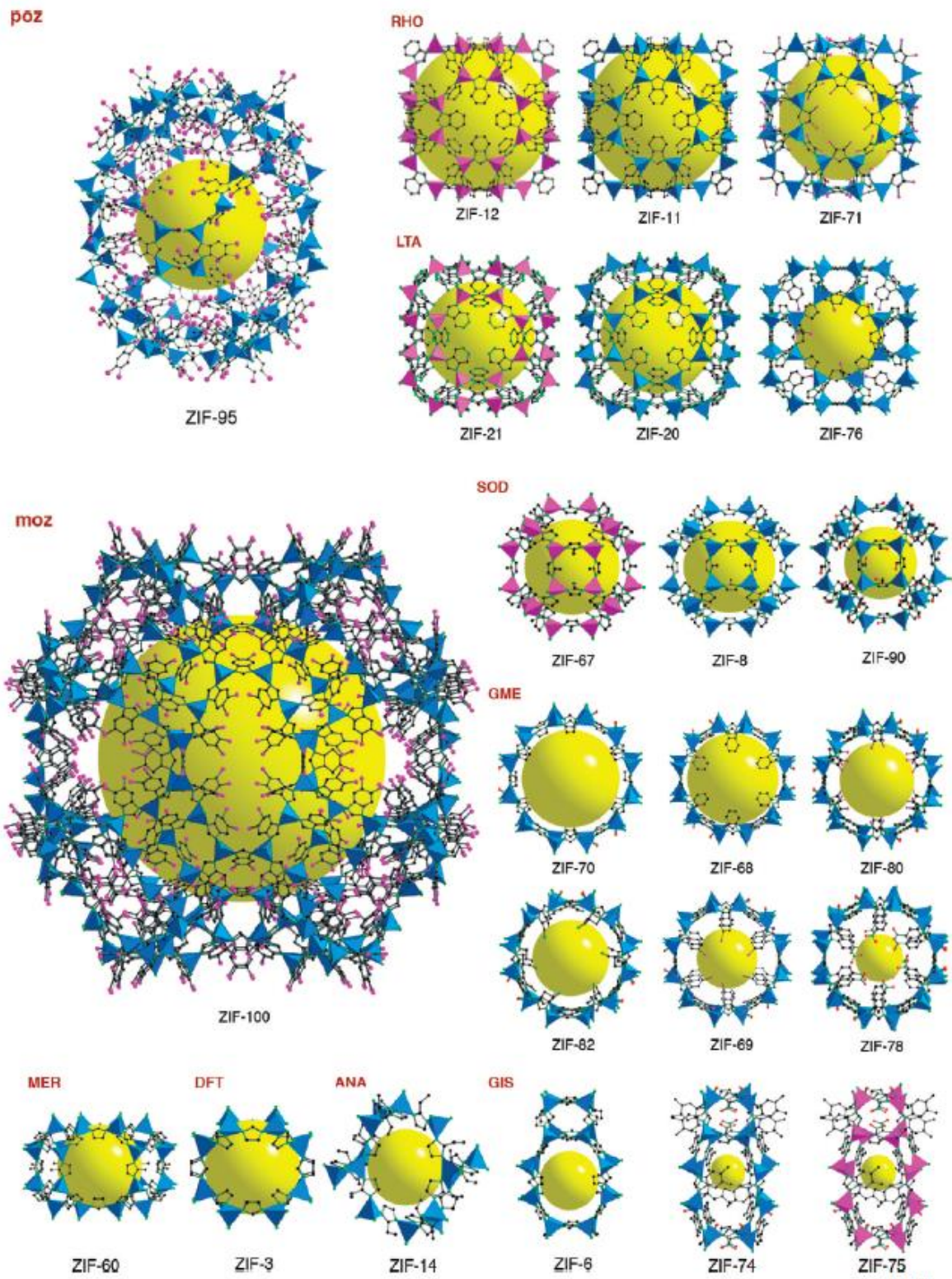


Figure 1-3 Crystal structures of ZIFs grouped according to their topology.⁵

ZIF materials are conventionally prepared through solvothermal methods where selected organic solvents act as the reaction medium. In 2006, Yaghi *et al.* pioneered the synthesis of twelve ZIF crystals, termed as ZIF-1 to -12, in organic solvent systems such as *N,N*-dimethylformamide (DMF), *N,N*-diethylformamide (DEF) and *N*-methylpyrrolidine (NMP).⁶ Also, methanol is another important organic solvent widely used in the synthesis of ZIFs. In 2006, Chen's group generated, for the first time, ZIF crystals using methanol as the reaction medium, where 2-methylimidazole or 2-ethylimidazole-containing methanol solution was slowly and carefully layered onto the aqueous ammonia solution containing Zn(OH)₂ for one month.⁷ Moreover, other alcohols such as ethanol⁸ and isopropyl alcohol⁹ were also successfully used as organic solvents in ZIFs synthesis. The particle sizes and morphology of ZIFs can be also controlled using different solvents.¹⁰ For example, Shieh *et al.* investigated the properties of ZIF-90 using different solvents,¹¹ as shown in **Figure 1-4**.

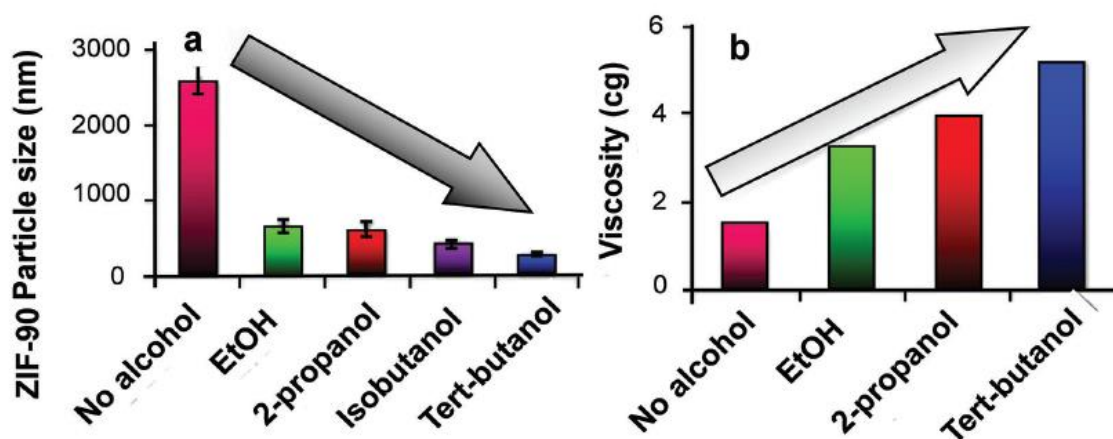


Figure 1-4 (a) The corresponding particle sizes of the ZIF-90 materials synthesized in different systems, and (b) the measured viscosity of each H₂O/alcohol system.¹¹

Due to the above mentioned characteristics of ZIFs, they have been considered as one of the most promising candidates for the applications in photovoltaic conversion and energy storage, such as dye-sensitized solar cells¹² and supercapacitors.¹³ However, most of the ZIFs are insulators, resulting from the poor overlapping between the d orbitals of the metals and π orbital of the insulating organic ligand.¹⁴ Poor electrochemical conductivities and unsuitable pore size distribution of ZIFs are two major drawbacks for its applications in photovoltaic conversion and energy storage.

1-2 Introduction of dye-sensitized solar cells (DSSCs)

In 1991, Brian O'Regan and Michael Grätzel made a breakthrough (~7% cell efficiency) on dye-sensitized solar cells (DSSCs) using a mesoporous titanium dioxide (TiO₂) film as the dye-derived wide-band semiconductor, thus facilitating the intensive investigation on this type of solar cells, which were considered as one of the most potential renewable power sources due to their remarkable advantages such as the low-cost production, simple fabrication processes in ambient conditions, semi-transparent and colorful appearances, possible plasticity, and high efficiencies (especially under indoor illumination or dim-light irradiation). Recently, Professor M. Grätzel and C. Y. Yeh's group incorporated a novel zinc porphyrin dye, YD2-o-C8, co-sensitized with Y123 dye, the pertinent DSSC worked with a novel cobalt (Co²⁺/Co³⁺) redox couple and gave an efficiency of 12.3%, which is the highest record of the efficiency of DSSC in 2011.¹⁵ In 2014, the DSSC with the zinc porphyrin dye and Co^(II/III) tris(bipyridine)-based redox electrolyte reached an excellent efficiency record of 13.00%,¹⁶ and soon after, the highest efficiency record of 14.30% was achieved by a DSSC with the co-sensitization of two metal-free organic dyes and Co^(II/III) tris(phenanthroline)-based redox electrolyte in 2015.¹⁷ These breakthroughs further encouraged research studies on developing economical photovoltaic devices based on DSSCs and made DSSCs more competitive in the solar cell markets. Besides, the DSSCs are believed to have versatile applications due to several advantages, e.g., colorful patterns for green building, low-cost roll-to-roll printing process, high performance under dim light intensity, under high temperature conditions.

The basic components of a DSSC include photoanode, electrolyte, and counter electrode. A photoanode consists of a conductive substrate, a mesoporous metal oxide semiconductor film adsorbed with a photo-sensitized dye. A conductive substrate generally include highly transparent fluorine-doped tin oxide glass (FTO), indium tin oxide (ITO), ITO/polyethylene terephthalate (PET) film, ITO/polyethylene naphthalate (PEN) film, *etc.*, are used for the applications of front-illuminated DSSCs; while other non-transparent conductive substrates, e.g., stainless steel and titanium foil, are used for the applications of back-illuminated DSSCs.¹⁸ A mesoporous metal oxide semiconductor film generally contains crystalline metal oxides with high energy band gaps, including titanium

dioxide (TiO₂), zinc oxide (ZnO), *etc.* A photo-sensitized dye generally contains metal complex dyes and metal-free organic dyes;^{19,20} metal complex dyes includes ruthenium dyes (N3, N719, Z907, *etc.*) and zinc dyes (YD2-o-C8, SM315, *etc.*), while metal-free organic dyes includes various species, *e.g.*, D149, C219, WS-9, JK-216, Y123, SQ1, SQ2. An electrolyte contains the redox species and supporting electrolytes. The redox species normally is iodide/triiodide (I⁻/I₃⁻) redox couple and selenocyanate-based redox couple (SeCN⁻/(SeCN)₂). Many alternative redox mediators were investigated, including halogen redox mediators (*i.e.*, bromide), pseudohalogen redox mediators (*i.e.*, cyanide, cyanate, thiocyanate), polysulfide redox mediators (S_n²⁻/S_{n+1}²⁻), metal complexes redox mediators (*i.e.*, Co, Fe, Cu, Ni-complex), and organic redox mediators (*i.e.*, 2,2,6,6-tetramethylpiperidin N-oxyl free radicals (TEMPO), disulfide/thiolate, tetramethylthiourea derivatives, 2-mercapto-5-methyl-1,3,4-thiadiazole derivatives, L-cysteine/L-cystine, quinone derivatives).²¹ A counter electrode (CE) is an electrocatalytic thin film on a conducting substrate. The electrocatalytic thin film generally is platinum (Pt), the details about electrocatalytic materials will be discussed in **Section 1-3**. Irradiated under sunlight with a standard solar radiation spectrum (air mass 1.5 global (AM 1.5G), equals to 100 mW cm⁻²), the working mechanism of a DSSC functions as the following steps, as shown in **Figure 1-5** and **Table 1-1**.

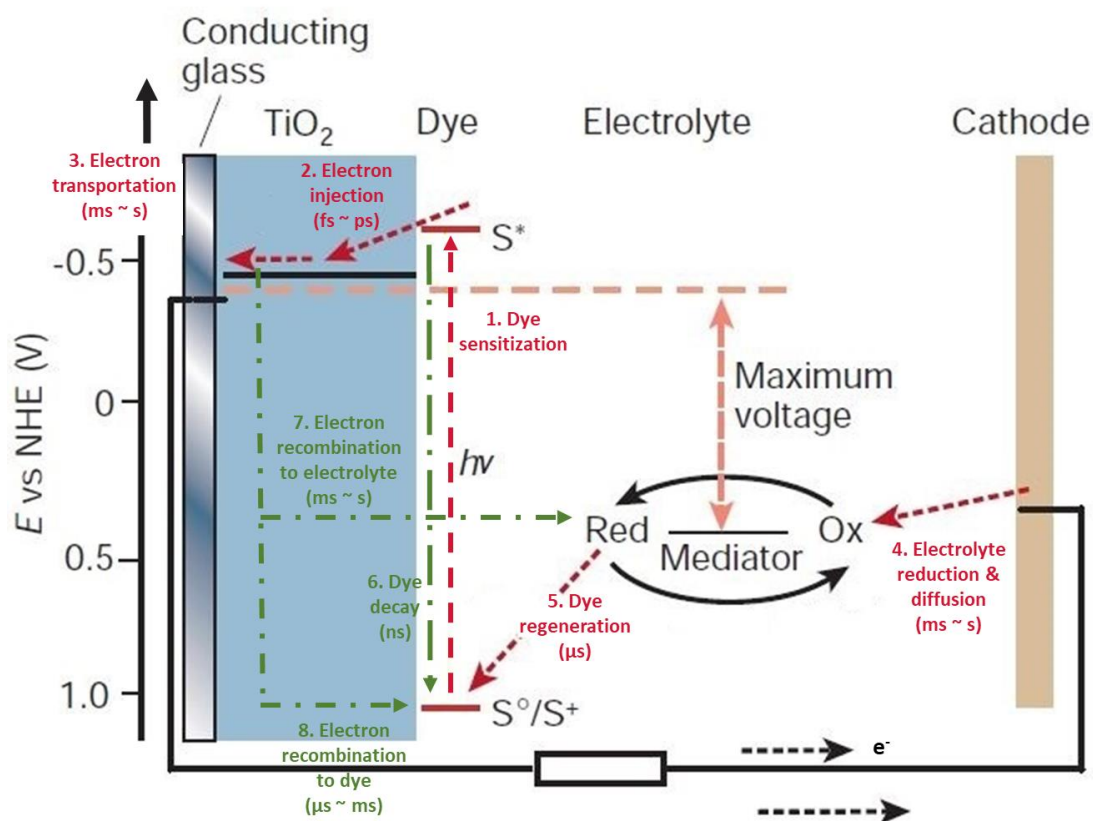
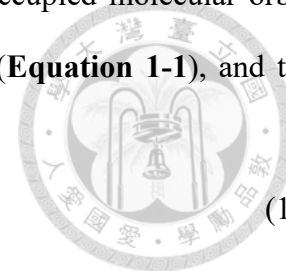


Figure 1-5 The cell constructions and mechanisms involved in a DSSC.²²

Table 1-1 The mechanism and related chemical reaction of a DSSC.

Forward reaction		
1. Dye sensitization	$\text{TiO}_2 \text{Dye} \rightarrow \text{TiO}_2 \text{Dye}^*$	(1-1)
2. Electron injection	$\text{TiO}_2 \text{Dye}^* \rightarrow \text{TiO}_2 \text{Dye}^+ + e^- (\text{TiO}_2)$	(1-2)
3. Electron transportation	$e^- (\text{TiO}_2) \rightarrow e^- (\text{FTO})$	(1-3)
4. Electrolyte reduction	$1/2 \text{I}_3^- + e^- (\text{Pt}) \rightarrow 3/2 \text{I}^-$	(1-8)
5. Dye regeneration	$3/2 \text{I}^- + \text{TiO}_2 \text{Dye}^+ \rightarrow 1/2 \text{I}_3^- + \text{TiO}_2 \text{Dye}$	(1-9)
Backward reaction		
6. Deactivation of Dye	$\text{TiO}_2 \text{Dye}^* \rightarrow \text{TiO}_2 \text{Dye}$	(1-10)
7. Recombination by electrolyte	$e^- (\text{TiO}_2) + 1/2 \text{I}_3^- \rightarrow 3/2 \text{I}^-$	(1-11)
8. Recombination by dye	$e^- (\text{TiO}_2) + \text{TiO}_2 \text{Dye}^+ \rightarrow \text{TiO}_2 \text{Dye}$	(1-12)

- (1) **Dye sensitization:** the dye molecule is sensitized from its highest occupied molecular orbital (HOMO) to its lowest unoccupied molecular orbital (LUMO) state (**Equation 1-1**), and then generates the photo-induced electrons.



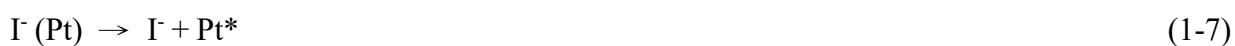
- (2) **Electron injection:** the photo-induced electrons are injected into the conduction band of the semiconductor (**Equation 1-2**). The rate of this electron injection reaction is ultrafast, typically occurring at the order of hundreds of femtoseconds to tens of picoseconds.



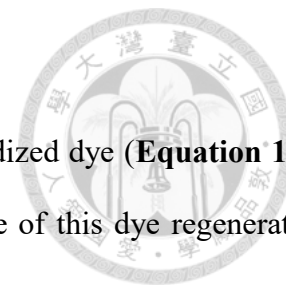
- (3) **Electron transportation:** the photo-induced electron percolates through the TiO_2 film, and is thought to move by a “hopping” mechanism, and is driven by a chemical diffusion gradient (rather than an electric field), and is collected at a transparent conductive substrate (usu. FTO) as **Equation 1-3**. The rate of this electron transportation occurs at the order of miniseconds to seconds.



- (4) **Electrolyte reduction and diffusion:** after passing through an external circuit, the electron is reintroduced into the DSSC at the CE (usu. Pt), where the oxidized redox species (usu. I_3^-) has the reduction reaction, where general consensus of mechanism can be described as **Equation 1-4~1-7** and the overall reaction can be written as **Equation 1-8**.^{23, 24} Then the reduced redox species (I^-) diffuses to the photoanode. The rate of step occurs at the order of miniseconds to seconds.



where * represents the free site on the electrode surface.



- (5) **Dye regeneration:** the reduced redox species (I^-) regenerates the oxidized dye (**Equation 1-9**), thereby completing the circuit with no net chemical change. The rate of this dye regeneration occurs at the order of microseconds.



Also, three deleterious back reactions would occur and compete with the above-mentioned forward reactions, as shown in **Figure 1-5**; these back reactions cause the decrease in the electron lifetime in a DSSC, and thereby make an energy loss and the limitation the cell efficiency.

- (6) **Dye decay:** once the dye sensitization occurs, the generated photo-induced electrons may directly recombine with the oxidized dye (Dye^+) as **Equation 1-10**. The rate of step occurs at the order of nanoseconds.



- (7) **Electron recombination to electrolyte:** once the electron injection occurs, the photo-induced electrons may directly recombine with the oxidized redox species (usu. I_3^-) as **Equation 1-11**. The rate of step occurs at the order of miniseconds to seconds.



- (8) **Electron recombination to dye:** once the electron injection occurs, the photo-induced electrons may directly recombine with the oxidized dye (Dye^+) as **Equation 1-12**. The rate of step is typically occurring at the order of microseconds to miniseconds.



1-2-1 Counter electrodes (CEs) in DSSCs

In the progress of DSSCs, achieving a high efficiency and reducing their fabrication cost are great challenges faced by scientists today. To achieve a high efficiency, a counter electrode (CE) plays an crucial role as an electrocatalyst to trigger the reduction of the oxidized redox species (usu. I_3^-). In accordance with the above-mentioned mechanism of a DSSC, the reduction of I_3^- is one of the rate determine-steps in a DSSC. Consequently, an electrocatalytic material as a CE is designed to facilitate the heterogeneous charge transfer rate at the CE/electrolyte interface. Namely, an electrocatalytic material aims to speed-up the reaction shown in **Equation 1-8**. Besides, the I_3^- is strongly electron-deficient and highly reactive; a slow electrocatalytic reduction of I_3^- can cause serious energy loss in a DSSC due to their susceptibility for recombination reactions with the photo-induced electrons at photoanode/electrolyte interface (**Equation 1-11**). To prevent the electron recombination and the pertinent energy loss in a DSSC, a fast consumption (reduction) of I_3^- using an effective electrocatalytic material is the key issue to obtain a highly efficient DSSC. Generally, a CE requires excellent electrocatalytic ability, good charge transfer capability, good conductivity, high corrosion resistivity, and good electrochemical stability.²⁵

Platinum (Pt) usually works as the best electro-catalyst due to its outstanding electrocatalytic ability toward I_3^- reduction, and thereby Pt is the most frequently used counter electrode in the DSSCs. However, the long-term stability of the counter electrode is limited because Pt is easily poisoned by the iodide.²⁶ Besides, Pt metal is expensive and scarce in nature. The limited supply of Pt cannot meet the increasing demand for its broad applications. In addition, Pt is not effective as a CE for redox couples such as cobalt-complexes, T_2/T^- , and polysulfide electrolytes used in solar cells.²⁷⁻²⁹ Especially, Pt used for Co-mediated DSSC has a large dispute due to the electrochemical characteristics of the Co^{3+}/Co^{2+} redox couple containing various ligands such as bipyridine-, terpyridine- and phenanthroline.³⁰ In this regard, an effective strategy in order to overcome the challenges associated with Pt-based electrodes is to develop high-performance Pt-free CE catalytic materials, which should provide high electrical conductivity and superior catalytic activity simultaneously. Thus, industrialization of DSSCs would benefit from replacing Pt electrode with low-

cost Pt-free CE catalytic material. In recent decade, plenty of researchers try to reduce the usage of Pt or to develop substitutions of Pt. Several types of materials have been investigated, *i.e.*, (1) metals, (2) conducting polymers, (3) transition metallic compounds, and (4) carbon materials, as summarized in **Figure 1-6**.

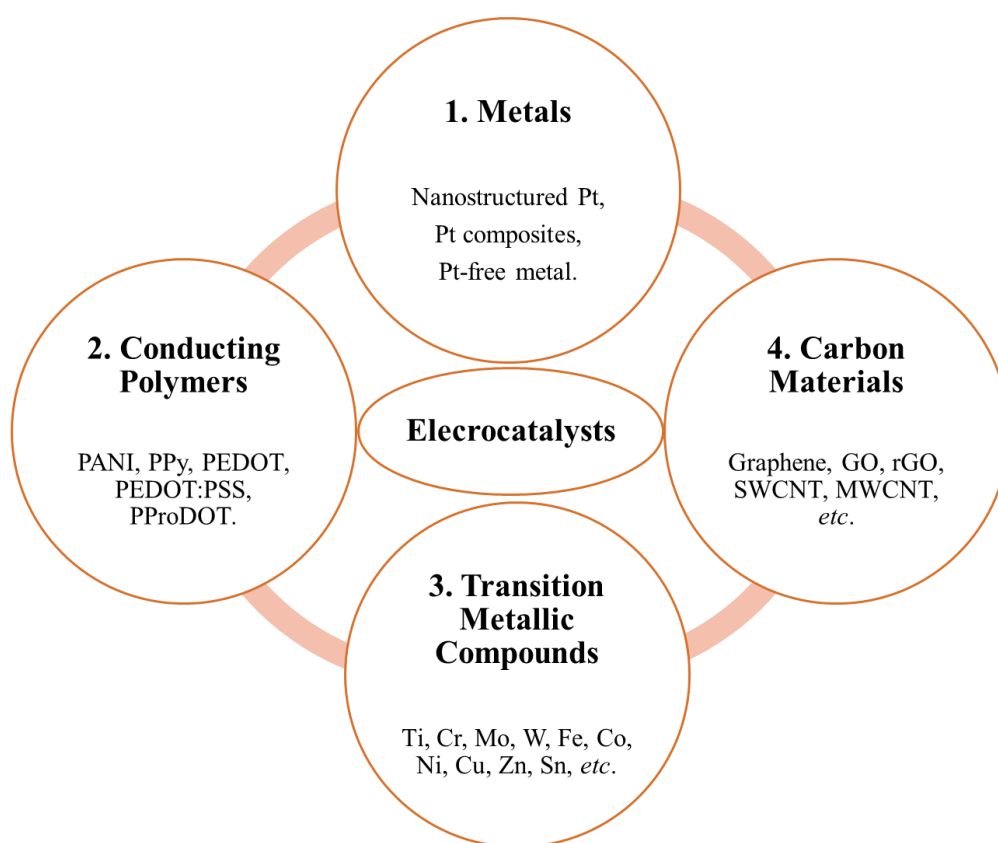
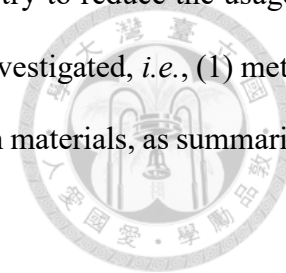


Figure 1-6 The categories of the electrocatalysts as CEs in DSSCs.

Metal type materials are intensively developed in the last two decades due to its superior conductivity and electrochemical activity for the regeneration of various redox species. Among all the metal type materials, Pt-based materials are the most frequently used; therefore, the researches on the metal type materials can be divided into three parts: (1) nanostructured Pt, (2) Pt composite, and (3) Pt-free metal, considering their approaches. The cost problem still remained, because the usage of the expensive Pt.^{31,32}

Conducting polymers (CPs) can fast conduct the electrons using their conjugated polymer chains. Generally, the CPs are the promising replacements for Pt owing to their excellent electrocatalytic

ability, high electrical conductivity, low-cost (suitable for roll-to-roll fabrication process), and good electrochemical stability for the regeneration of the redox species.³³ Furthermore, the high transparency of the CPs benefits the composing of the bifacial DSSCs illuminated by the both sides of the cells, indicating that the CPs have great flexibility for the multiple applications of DSSCs. So far, several highly efficient CPs have been developed *via* simple electro-polymerization processes, *e.g.*, polyaniline (PANI), polypyrrole (PPy), poly(3,4-ethylenedioxythiophene) (PEDOT), poly(3,4-ethylenedioxythiophene):poly (styrene-sulfonate) (PEDOT:PSS), poly(3,4-propylenedioxythiophene) (PProDOT), poly(3,3-dimethyl-3,4-dihydro-2*H*-thieno(3,4-*b*)(1,4)dioxepine) (PProDOT-Me₂), poly(3,3-diethyl-3,4-dihydro-2*H*-thieno(3,4-*b*)(1,4)dioxepine) (PProDOT-Et₂). However, the CPs often have the flat morphologies, demonstrating the unfavorable electrochemical surfaces without directional electron pathways.³⁴⁻³⁶

Several carbonaceous materials have become potential materials to substitute Pt because of their low cost, high conductivity, and good catalytic ability for the reduction of the redox species. Generally, carbonaceous materials are constructed by the carbon atoms connected with a sp^2 planar or a sp^3 tetrahedron arrangements. The mostly attractive sp^2 planar-arranged carbonaceous material is graphite due to its metal-like conductivity. Therefore, plenty of graphite-based materials were extensively explored, *e.g.*, graphene, graphene oxide (GO), reduced graphene oxide (rGO), single-walled carbon nanotube (SWCNT), multi-walled carbon nanotube (MWCNT), and fullerene (C₆₀). On the other hand, many sp^3 tetrahedron-arranged carbonaceous materials with were also studied as the CEs for DSSCs, *e.g.*, carbon nanofiber, activated carbon, and carbon black. However, dispersants were usually used for preparing the crack-free carbon-based electrocatalytic film on conducting substrate. Thus, the electrocatalytic ability and conductivity of the carbonaceous type CE would be limited by the addition of the surfactant.^{37, 38}

Transition metallic compound (TMC) type materials have several advantages, *i.e.* low-cost, high electrical conductivity, reasonable thermal conductivity, high electrocatalytic ability, large effective surface area, and good stability for the regeneration of the redox species. TMCs are usually composed of various transition metallic cations and non-metal anions.³⁹ In the case of transition metallic cations,

titanium (Ti), iron (Fe), cobalt (Co), nickel (Ni), copper (Cu), zinc (Zn), silicon (Si), and tin (Sn) compounds, *etc.*, have been widely investigated as shown in **Figure 1-7** (highlighted with the blue background). In the case of anions, IV-A, V-A, VI-A groups of elements are mostly used as shown in **Figure 1-7** (highlighted with the green background and circled by the black line), including carbides, nitrides, oxides, sulfides, selenides and tellurides, have been successfully established. Generally, the DSSCs with efficient TMC type CEs generally reach η of 7~8%, which are about 80~90% to the η of their Pt-based DSSCs, and thus TMC type CEs were considered as the potential catalysts for replacing Pt CE in DSSCs. However, even though some TMC type materials have good electrocatalytic ability for I^-/I_3^- , they may be suffered from aggregation and thus lack of large surface area, good conductivity, directional electron pathways, or attachment toward the conducting substrate. From which, a low short-circuit current density (J_{sc}) and a poor fill factor (FF) can be obtained from the pertinent DSSCs. Therefore, many researches introduced other materials (including TMCs, CPs, or carbonaceous) to make up composites, and thereby the idea of using a TMC-based composite film as a CE in a DSSC was raised. Highly efficient TMC materials are often synthesized *via* a high-cost process (e.g., high vacuum or high temperature). Some of the TMCs are even rare on earth and are toxic to environment. Therefore, a highly efficient, earth abundant, non-toxic TMCs are needed for the future development of DSSCs.

1 H 1.008 Hydrogen																	2 He 4.002602 Helium	
3 Li 6.94 Lithium	4 Be 9.0121831 Beryllium											5 B 10.81 Boron	6 C 12.011 Carbon	7 N 14.007 Nitrogen	8 O 15.999 Oxygen	9 F 18.998403163 Fluorine	10 Ne 20.1797 Neon	
11 Na 22.98976928 Sodium	12 Mg 24.305 Magnesium											13 Al 26.9815385 Aluminum	14 Si 28.086 Silicon	15 P 30.973761998 Phosphorus	16 S 32.06 Sulfur	17 Cl 35.45 Chlorine	18 Ar 39.948 Argon	
19 K 39.0983 Potassium	20 Ca 40.078 Calcium	21 Sc 44.955908 Scandium	22 Ti 47.867 Titanium	23 V 50.9415 Vanadium	24 Cr 51.9961 Chromium	25 Mn 54.938044 Manganese	26 Fe 55.845 Iron	27 Co 58.933194 Cobalt	28 Ni 58.6934 Nickel	29 Cu 63.546 Copper	30 Zn 65.38 Zinc	31 Ga 69.723 Gallium	32 Ge 72.630 Germanium	33 As 74.921595 Arsenic	34 Se 78.971 Selenium	35 Br 79.904 Bromine	36 Kr 83.798 Krypton	
37 Rb 85.4678 Rubidium	38 Sr 87.62 Strontium	39 Y 88.90584 Yttrium	40 Zr 91.224 Zirconium	41 Nb 92.90637 Niobium	42 Mo 95.94 Molybdenum	43 Tc 98 Technetium	44 Ru 101.07 Ruthenium	45 Rh 102.90550 Rhodium	46 Pd 106.42 Palladium	47 Ag 107.8682 Silver	48 Cd 112.414 Cadmium	49 In 114.818 Indium	50 Sn 118.710 Tin	51 Sb 121.760 Antimony	52 Te 127.60 Tellurium	53 I 126.90447 Iodine	54 Xe 131.29 Xenon	
55 Cs 132.90545196 Cesium	56 Ba 137.327 Barium	57 La 138.90547 Lanthanum	71 Lu 174.9668 Lutetium	72 Hf 178.49 Hafnium	73 Ta 180.94788 Tantalum	74 W 183.84 Tungsten	75 Re 186.207 Rhenium	76 Os 190.23 Osmium	77 Ir 192.217 Iridium	78 Pt 195.084 Platinum	79 Au 196.966569 Gold	80 Hg 200.592 Mercury	81 Tl 204.38 Thallium	82 Pb 207.2 Lead	83 Bi 208.98040 Bismuth	84 Po 209 Polonium	85 At 210 Astatine	86 Rn 222 Radon
87 Fr 223 Francium	88 Ra 226 Radium	89 Ac 227 Actinium	103 Lr 260 Lawrencium	104 Rf 261 Rutherfordium	105 Db 262 Dubnium	106 Sg 263 Seaborgium	107 Bh 264 Bohrium	108 Hs 265 Hassium	109 Mt 266 Meitnerium	110 Ds 267 Darmstadtium	111 Rg 268 Roentgenium	112 Cn 269 Copernicium	113 Nh 270 Nihonium	114 Fl 271 Flerovium	115 Mc 272 Moscovium	116 Lv 273 Livermorium	117 Ts 274 Tennessine	118 Og 274 Oganesson
Lanthanide Series			57 La 138.90547 Lanthanum	58 Ce 140.116 Cerium	59 Pr 140.90766 Praseodymium	60 Nd 144.242 Neodymium	61 Pm 145 Promethium	62 Sm 150.36 Samarium	63 Eu 151.964 Europium	64 Gd 157.25 Gadolinium	65 Tb 158.92535 Terbium	66 Dy 162.500 Dysprosium	67 Ho 164.93033 Holmium	68 Er 167.259 Erbium	69 Tm 168.93422 Thulium	70 Yb 173.054 Ytterbium	71 Lu 174.9668 Lutetium	
Actinide Series			89 Ac 227 Actinium	90 Th 232.0377 Thorium	91 Pa 231.03688 Protactinium	92 U 238.02891 Uranium	93 Np 237 Neptunium	94 Pu 244 Plutonium	95 Am 243 Americium	96 Cm 247 Curium	97 Bk 247 Berkelium	98 Cf 251 Californium	99 Es 252 Einsteinium	100 Fm 257 Fermium	101 Md 258 Mendelevium	102 No 259 Nobelium	103 Lr 260 Lawrencium	

Figure 1-7 The transition metallic cations (blue part) and the anions (green part with black line) that can be combined to prepare the TMC type CE for the DSSCs.

1-3 Introduction of supercapacitors (SCs)

Due to the rapidly increasing human activities, the fossil fuels gradually depleted and the climate severely changed. The environmental problems urgently make the society move toward the next-generation energy resources which are renewable, sustainable and environmental-friendly. As a result, there has been an ever-increasing and urgent demand for the development of not only clean, renewable, and sustainable alternative energies (solar, wind, and tide), but also advanced, low-cost, and environmentally friendly energy conversion and storage devices to satisfy the needs of modern society.⁴⁰

From the beginning of the last century, energy storage systems have become increasingly ingrained in our daily life, including lithium-ion batteries and electrochemical capacitors. In 1990s, the first commercial lithium-ion batteries were introduced by Sony, and series of pioneering works were successively done by M. Armand.⁴¹ These rechargeable batteries, although costly, show the best performance in energy densities. Even though numerous efforts have been put into the improvement for further higher performance in Li-ion and other rechargeable batteries, the low power density still limits their commercial applicability. Another important problem is the short cycle life. Because of the lack of highly reversible redox reaction, damage on the electrode during the charge-discharge process is inevitable and therefore cause severe reduction in cycle lives. Based on the foregoing reasons, the role of energy storage systems with high power delivery was given to the electrochemical capacitors.

The electrochemical capacitors, also called supercapacitors, demonstrate numerous advantages such as remarkable power performance, excellent reversibility, long cycle life, simplicity of operation, and ease of integration into electronics. Besides, due to the simpler charge/discharge mechanisms of the supercapacitors, less thermochemical heat will be generated during the charge-discharging cycles compared to the batteries.⁴² Therefore, supercapacitors have been widely employed in consumer electronics, memory back-up systems, industrial power and energy management.⁴³

Figure 1-8 shows the plot of power density against energy density, which is also called the Ragone plot, for several kinds of electric energy storage devices.⁴⁴ The power density describes how fast the energy can be delivered by the storage devices, and the energy density describes how much energy is available from the devices. The times indicated beside the oblique lines are the time constants of the devices, which are obtained by the fraction of the energy density to the power density. It can be observed that the electrochemical capacitors (supercapacitors) just locate at a unique position which fill the gap between the conventional capacitors and batteries. Although, the energy density of the supercapacitors is an order of the magnitude lower than that of the batteries, they usually demonstrate two order of magnitude higher power density than batteries. This give the supercapacitors an important role in complementing or even replacing batteries in the energy storage application. A recent report proposed by the US Department of Energy assigns equal status to supercapacitors and batteries for future energy storage systems. These show that this topic have gained an increasing interest from the general public.

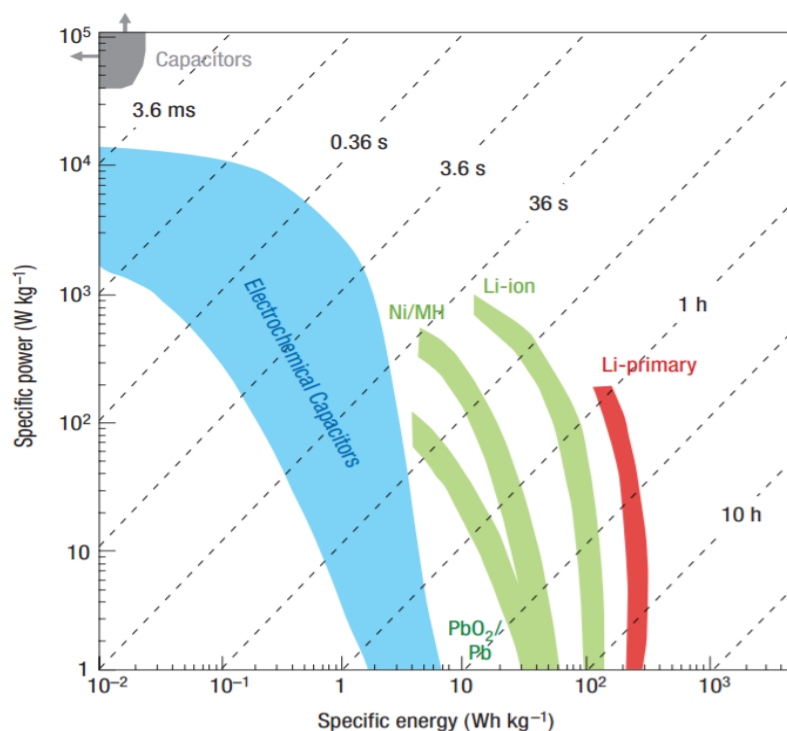


Figure 1-8 Specific power against specific energy, also called a Ragone plot, for various electrical energy storage devices.⁴⁴

Depending on their charge storage mechanism, supercapacitors can be classified into two categories: electric double-layer capacitors (EDLCs) and pseudocapacitors (PCs). Firstly, EDLCs are electrochemical capacitors that store the charge electrostatically using reversible adsorption of ions of the electrolyte onto active materials with high accessible specific surface area (**Figure 1-9**). The earliest model of the electric double layer can be traced back to Helmholtz in 1853, and thus the electric double layer is also called the Helmholtz layer.⁴⁵ Thereafter, the Gouy–Chapman model,^{46, 47} Stern model⁴⁸ and Grahame model⁴⁹ were subsequently proposed in order to more precisely describe the detailed structure of the electric double layer (**Figure 1-10**).

As a result of the electrostatic charge storage, there is no faradaic reaction and thus charge transfer across the electrodes of EDLCs. This major difference from batteries indicates that it allows very fast energy storage and delivery, which provides better power performance. The absence of faradaic reactions also eliminates the swelling effect in the electroactive material that exhibits in batteries during charge-discharging cycles, which make EDLCs be able to sustain millions of cycles, while it is only a few thousand at best in batteries. However, as a consequence of the electrostatic surface charging mechanism, EDLCs suffer from the limited energy density.

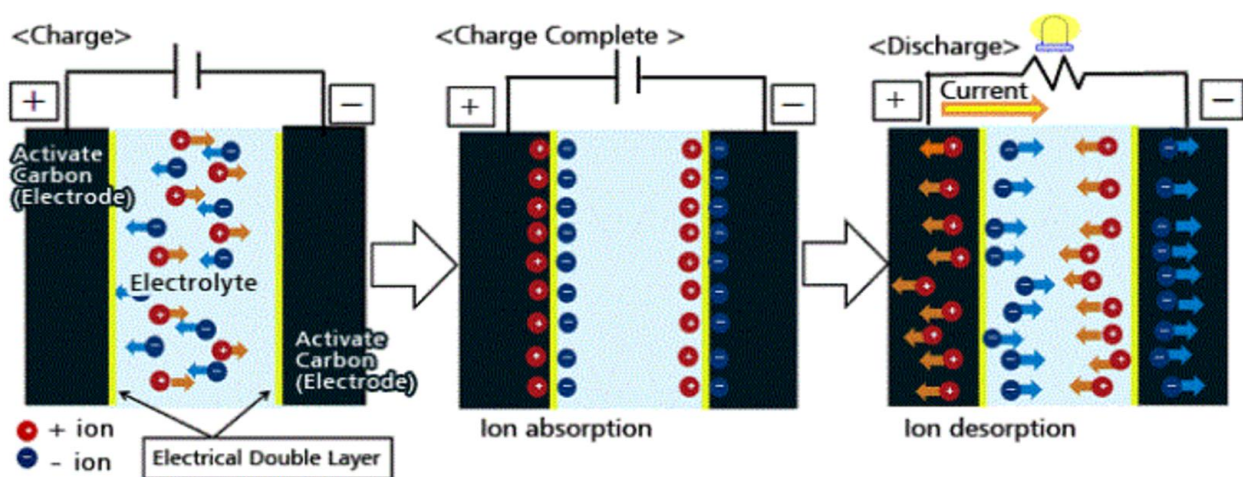


Figure 1-9 Schematic illustration of the charge and discharge of electrochemical double layer capacitor. (from Power Electronic, <https://www.powerelectronicstips.com/fundamentals-supercapacitor-balancing/>)

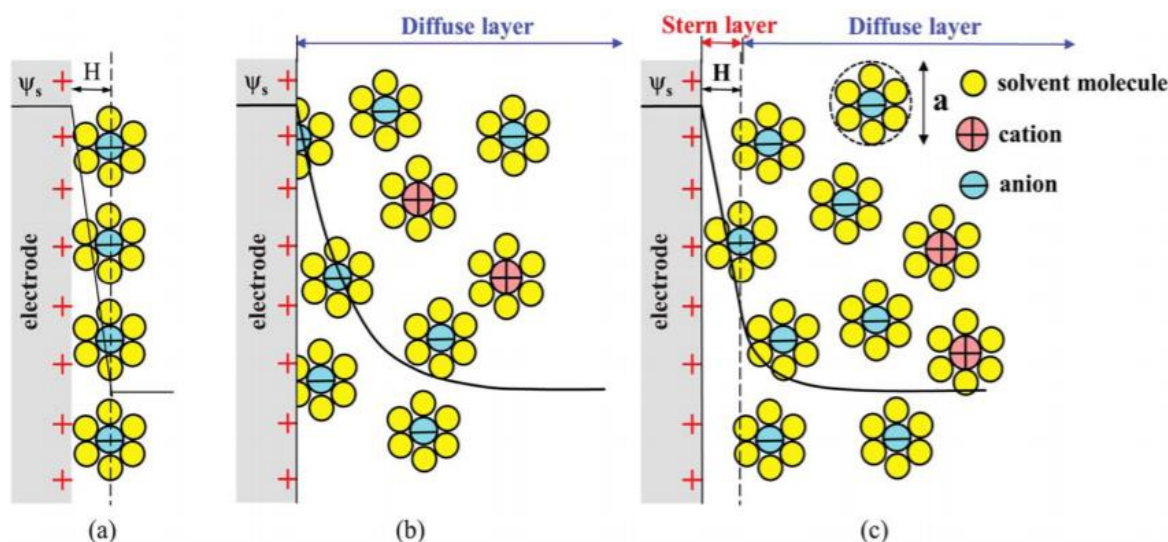


Figure 1-10 Schematic representation of electrical double layer structures according to (a) the Helmholtz model, (b) the Gouy-Chapman model, and (c) the Gouy-Chapman-Stern model. The double layer distance in the Helmholtz model and the Stern layer thickness are denoted by H while ψ_s is the potential at the electrode surface.⁵⁰

Another type of electrochemical capacitors use fast and reversible redox reactions at the surface of electroactive materials as the energy storage mechanism, which is much different from the typical electrostatic charges separation, thus is defined as what is called the pseudocapacitors. Transition metal oxides,^{51,52} metal hydroxides,⁵³ and conducting polymers,⁵⁴ which possess numerous oxidation states, have been extensively studied in the past decades. Recently, transition metal sulfides, *i.e.* cobalt sulfide, molybdenum disulfide, nickel sulfide and so on, have received widespread attention as appealing electrode materials for SCs in view of their outstanding electrochemical properties.⁵⁵⁻⁵⁹ Among the reported materials of metal sulfides, cobalt sulfide has emerged as a promising electrode material for SCs due to its higher mechanical, thermal stability and richer redox reactions with various crystalline phases compared with its cobalt oxide or hydroxide counterparts.^{57,60} Owing to the further faradaic reaction on the surface, the energy density of the pseudocapacitors is able to exceed that of the carbon materials which use electric double-layer charge storage. However, pseudocapacitors, similar to the batteries, suffer from the lower stability and power density which is limited by the rate of the electrochemical kinetics during cycling charge-discharging.

1-4 Motivation and scope of this thesis

In this thesis, except for the introduction (Chapter 1), experimental procedure (Chapter 2), and conclusions and suggestions (Chapter 5), in the rest of the thesis, we will focus our effort on the electrochemical applications of zeolitic imidazolate frameworks. There are two different but related chapters, discussing about the application of a zeolitic imidazolate framework-derived ZnSe/N-doped carbon cube hybrid electrocatalyst as the counter electrode for dye-sensitized solar cells (Chapter 3) and carbon nanotubes interconnected zeolitic imidazolate framework-derived cobalt sulfide hybrid composites for supercapacitors (Chapter 4). The flowchart of this thesis is illustrated in **Figure 1-11**. In the following paragraphs, the motivations and the expected research goals for Chapter 3 and Chapter 4 will be introduced.

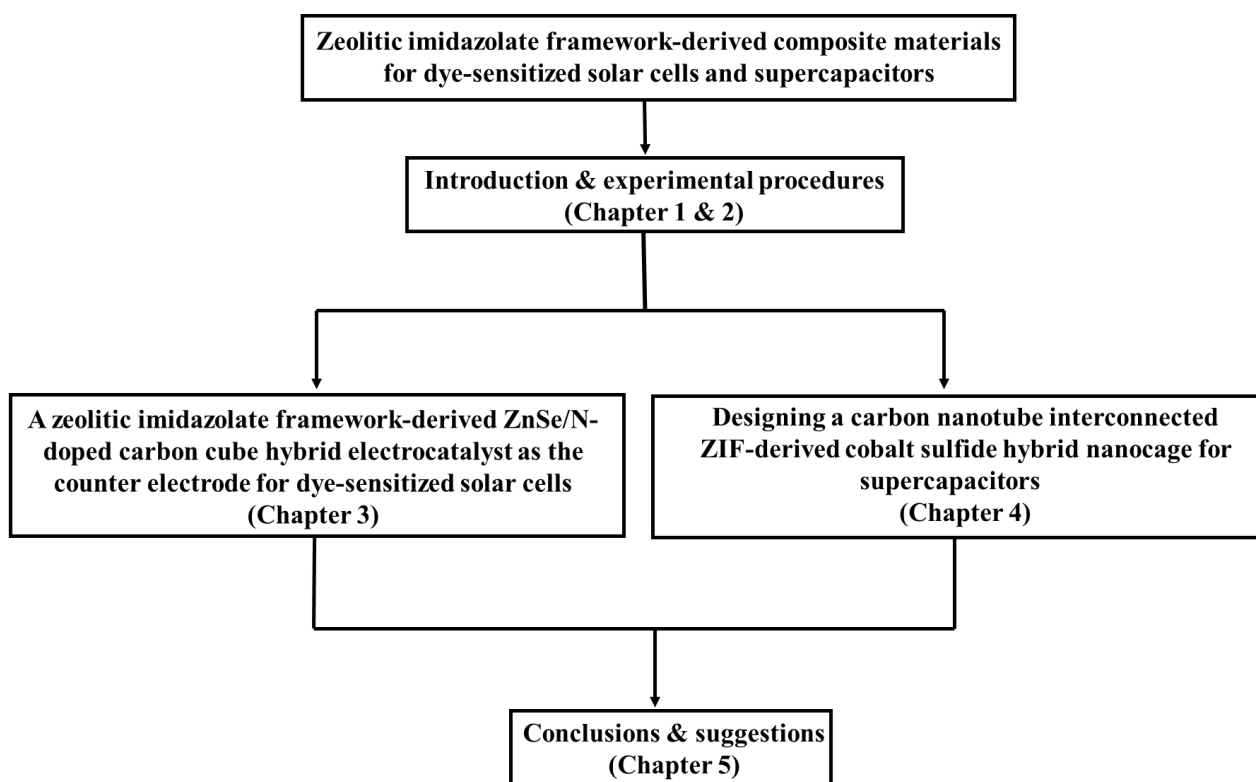


Figure 1-11 The flowchart of this thesis.

In Chapter 3, a zinc selenide decorated N-doped carbonaceous hybrid material (ZIF-ZnSe-NC) derived from a zeolitic imidazolate framework (ZIF-7) used as the electrocatalyst for the counter electrodes in DSSCs exhibited excellent electrocatalytic performance and electrical conductivity. Carbonization and selenization at different temperatures for synthesizing ZIF-ZnSe-NC electrocatalyst were carried out step by step to enhance the electrocatalytic performance and electrical conductivity of the material. In the ZIF-ZnSe-NC hybrid electrocatalyst, the N-doped carbon cube is beneficial to the electrocatalytic performance and the electrical conductivity. Meanwhile, embedded ZnSe in the carbon matrix also serves as the additional active site for facilitating I_3^- reduction. The DSSCs with the optimized ZIF-ZnSe-NC-11 wt% CEs exhibited a photovoltaic conversion efficiency (η) of $8.69 \pm 0.13\%$, which is higher than that of the cells with Pt CEs ($8.26 \pm 0.02\%$). A reasonable cell efficiency of $7.99 \pm 0.01\%$ was still attained for the DSSCs with CEs of ZIF-ZnSe-NC-11 wt% at a dim light intensity of 10 mW cm^{-2} . Thus, it could be concluded that the ZIF-ZnSe-NC is a promising material to replace the expensive Pt in DSSCs, especially for the indoor application.

In Chapter 4, a hybrid structure of carbon nanotubes interconnected zeolitic imidazolate framework (ZIF) derived cobalt sulfide (CNT/CoS) nanocage was designed and synthesized as the electrode material in SCs. The carbon nanotubes/ZIF-67 (CNT/ZIF-67) nanocomposites with controlled ZIF-67 particle sizes have been systematically studied by varying the mass ratio of CNT to ZIF-67 under reaction process, then followed by subsequent sulfurization with thioacetamide. Benefiting from the porous nanocage architecture and conductive CNTs, the optimized CNT/CoS nanocage exhibits excellent electrochemical performance with an outstanding specific capacitance (2173.1 F g^{-1} at 5 A g^{-1}), good rate capacity (65% retention at 20 A g^{-1}), and long-term stability (91% retention over 1000 cycles), demonstrating a great potential in energy applications. The method developed in this work can be extended to the construction of other metal sulfide electrode materials for a variety of energy storage applications.

Chapter 2

Experimental procedures



In Chapter 2, we will start to discuss the experimental details regarding Chapter 3 and 4 described in this thesis. The general experimental materials will be introduced firstly in Section 2-1, and the details about Chapter 3 and Chapter 4 will be discussed in Sections 2-2 and 2-3. Finally, the corresponding analytic techniques will be introduced in Section 2-4.

2-1 Materials

Anhydrous methanol (MeOH, 99.8%), ethanol (EtOH, 99.5%), isopropyl alcohol (IPA, 99.5%), lithium perchlorate (LiClO_4 , $\geq 98.0\%$), titanium(IV) tetraisopropoxide (TTIP, $> 98\%$), tetrabutylammoniumtriiodide (TBAI_3 , $> 97\%$), 2-methoxyethanol, 2-methylimidazole (2-mlm, 99%), nafion[®] 117 solution (~5% in a mixture of lower aliphatic alcohols and water), thioacamide (TAA, $\geq 99.0\%$), and selenium pellets were purchased from Sigma Aldrich. Benzimidazole (bIM, 99%) and cobalt nitrate hexahydrate ($\text{Co}(\text{NO}_3)_2 \cdot 6\text{H}_2\text{O}$, 98%) were obtained from Alfa Aesar. Lithium iodide (LiI, synthetic grade), poly(ethylene glycol) (PEG, MW~20,000), and iodine (I_2 , synthetic grade) were received from Merck. Poly(3,4-ethylenedioxythiophene):poly(styrenesulfonate) aqueous solution (PEDOT:PSS, PH 500) was supplied by UniRegion Bio-Tech Co., Hsinchu, Taiwan. 4-tert-butylpyridine (tBP, 96%), tert-butyl alcohol (tBA, 96%) and polyvinylpyrrolidone (PVP, M.W. 58,000) were procured from Acros. 3-Methoxypropionitrile (MPN, 99%) was bought from Fluka. 1,2-Dimethyl-3-propylimidazolium iodide (DMPII), Surlyn[®] (SX1170-25, 25 μm), transparent TiO_2 paste (TL paste, Ti-nanoxide T/SP, with an average particle size = 20 nm), and cis-diisothiocyanato-bis(2,2'-bipyridyl-4,4'-dicarboxylato) ruthenium (II) bis (tetrabutylammonium) (N719 dye) were received from Solaronix (S.A., Aubonne, Switzerland). Zinc nitrate hexahydrate ($\text{Zn}(\text{NO}_3)_2 \cdot 6\text{H}_2\text{O}$, 99%), ammonium hydroxide (NH_4OH , 28.0%), acetonitrile (ACN, 99.99%) and nitric acid (HNO_3 ,

ca. 65% solution in water) were supplied by J. T. Baker. The commercial light scattering TiO₂ particles, ST-41 (average particle size = 200 nm), were acquired from Ishihara Sangyo, Ltd. Fluorine-doped tin oxide (FTO) conducting glasses ($7 \Omega \text{ sq}^{-1}$, UR-ITO007-0.7 mm) were obtained from NSG America, Inc., New Jersey, USA. Functionalized carbon nanotube (CNT-COOH modified, >98.0%) was purchased from Golden Innovation Business Co. Ltd., Taipei, Taiwan.

2-2 Experiments relating to a zeolitic imidazolate framework-derived ZnSe/N-doped carbon cube hybrid electrocatalyst as the counter electrode for dye-sensitized solar cells

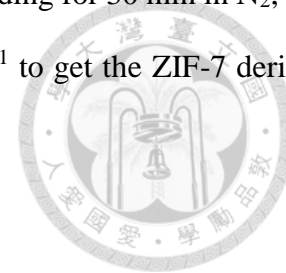
In this section, the specific experiments about the zeolitic imidazolate framework-derived ZnSe/N-doped carbon cube hybrid electrocatalyst as the counter electrode for dye-sensitized solar cells (Chapter 3) is discussed. We will introduce the synthesis steps of the ZIF-7-derived catalysts utilized in Chapter 3.

2-2-1 Synthesis of ZIF-7 and ZIF-7-derived catalysts

The ZIF-7 sample was synthesized according to the procedure reported previously.⁸ Zinc nitrate hexahydrate ($\text{Zn}(\text{NO}_3)_2 \cdot 6\text{H}_2\text{O}$, 0.90 g, 3 mmol) was dissolved in ethanol (12.67 mL); benzimidazole (bIM, 0.72 g, 6 mmol) was dissolved in ethanol (38.02 mL), followed by the addition of ammonia hydroxide solution (3.18 mL, 48 mmol NH_3). The solution turned white immediately, and the resultant mixture was stirred for 10 min at room temperature to complete the crystallization. The product, ZIF-7, was collected by centrifugation and was washed with ethanol for three times, then dried at room temperature under atmosphere overnight.

The as-prepared ZIF-7 was annealed in a furnace with a heating rate of $3 \text{ }^\circ\text{C min}^{-1}$, maintaining at a given temperature (600, 700, 800, 900, 1000 $^\circ\text{C}$) for 1 h under a flow of N_2 , and cooled down to room temperature with a cooling rate of $10 \text{ }^\circ\text{C min}^{-1}$ afterwards to get ZIF-7 derived N-doped carbon cube (ZIF-NC). After that, the carbonized sample was further selenized with a heating rate of $10 \text{ }^\circ\text{C}$

min⁻¹, maintaining at a given temperature (300, 400, 450, 500, 600 °C) holding for 30 min in N₂, and then cooled down to room temperature with a cooling rate of 10 °C min⁻¹ to get the ZIF-7 derived ZnSe/N-doped carbon cube (ZIF-ZnSe-NC).



2-2-2 Preparation of counter electrodes

In this work, the substrate of the photoanodes and CEs was fluorine-doped tin oxide (FTO). The FTO was sequentially cleaned with a neutral cleaner, deionized water, acetone, and isopropanol. In order to compare the performances of various electrocatalytic films, four types of films were prepared as follows: (1) a Pt film (30 nm-thick) was obtained on an FTO by sputtering; (2) films of ZIF-NC with different carbonization temperatures (600~1000 °C) were prepared on 1 cm² controlled FTO substrate by a drop-coating technique with 50 μL of the PEDOT:PSS/EtOH mixing solution containing 5 wt% of synthesized powders; (3) films of ZIF-ZnSe-NC with different selenization temperatures (300~600 °C) were prepared on the FTO by the same drop-coating technique and recipe as mentioned above; (4) films of ZIF-ZnSe-NC with different weight percentage concentration of ZIF-ZnSe-NC (5, 7, 9, 11, 13 wt%) were prepared on 1 cm² controlled FTO substrate by a drop-coating technique with 50 μL of the PEDOT:PSS/EtOH mixing solution containing various weight percentages of ZIF-ZnSe-NC. (wt% = $W_{\text{ZIF-ZnSe-NC}} / (W_{\text{ZIF-ZnSe-NC}} + W_{\text{PEDOT:PSS}} + W_{\text{ethanol}})$)

2-2-3 Preparation of photoanode and the DSSC assembly

The TiO₂ film in the photoanode was consisted of a 100 nm compact layer, a 10 μm transparent layer, and a 4 μm scattering layer. The compact layer was coated on a cleaned FTO conducting surface via a spin-coating process using a mixture of titanium tetraisopropoxide (TTIP) and 2-methoxyethanol (weight ratio=1/3). A doctor-blade technique was used to obtain the transparent and scattering layers on the compact layer. The transparent layer was coated on the compact layer using the above-mentioned commercial transparent paste (Ti-nanoxide T/SP), while the scattering layer was further coated on the transparent layer using a home-made scattering paste. Each TiO₂ layer was sintered at 500 °C for 30 min in an air atmosphere, and then the sintered TiO₂ film with an active area

of 0.20 cm² was immersed in a 5×10⁻⁴ M N719 dye solution for 24 h at room temperature using a mixed solvent of tBA and ACN (volume ratio = 1/1). Thus, a dye-adsorbed TiO₂ film was prepared as the photoanode of a DSSC. Finally, a photoanode and a CE were assembled using a 25 μm-thick Surlyn[®] as the spacer. The electrolyte, which contained 0.1 M LiI, 0.05 M I₂, 0.6 M DMPII, and 0.5 M tBP in MPN/ACN (volume ratio = 1/1), was injected into the cell gap between these two electrodes.

The above-mentioned scattering paste was made in-house by a four-step process, as follows: (1) The TiO₂ colloid was prepared by adding 0.5 M titanium tetraisopropoxide aqueous solution to 0.1 M nitric acid aqueous solution with stirring at 88 °C for 8 h. (2) The solution was cooled down to room temperature, transferred to an autoclave (PARR 4540, USA), slowly heated to 240 °C and maintained at this temperature for 12 h; the TiO₂ nanoparticles reach an average diameter of 20 nm at this stage. (3) The autoclaved TiO₂ colloid was concentrated to contain 8 wt% of TiO₂ nanoparticles. (4) The scattering layer paste (SL paste) was acquired by the addition of 25 wt% PEG and 100 wt% of commercial scattering TiO₂ particles (ST-41) (both with respect to the weight of TiO₂) into the concentrated TiO₂ colloid. Here, PEG was used for preventing the aggregation of TiO₂ nanoparticles and for controlling the pore size among the TiO₂ nanoparticles. The scattering layer is required for light scattering to increase the utilization of light by the dye.

2-3 Experiments relating to designing a carbon nanotube interconnected ZIF-derived cobalt sulfide nanocage for supercapacitors

In this section, the specific experiments about the carbon nanotubes interconnected zeolitic imidazolate framework-derived cobalt sulfide hybrid composites as the electrode materials for supercapacitor (Chapter 4) is discussed. We will introduce the synthesis steps of the ZIF-67-derived nanocomposites utilized in Chapter 4.

2-3-1 Synthesis of ZIF-67, CNT/ZIF-67 nanocomposite, and hybrid CNT/CoS nanocage

The ZIF-67 sample was synthesized according to the procedure reported previously.⁶¹ Cobalt

nitrate hexahydrate ($\text{Co}(\text{NO}_3)_2 \cdot 6\text{H}_2\text{O}$, 0.722 g, 2.48 mmol) was dissolved in methanol (25 mL) and 2-methylimidazole (2-mlm, 1.629 g, 19.84 mmol) was dissolved in methanol (25 mL) separately. When both reagents were entirely dissolved in methanol, the solution consisted of 2-methylimidazole was rapidly added into the solution of $\text{Co}(\text{NO}_3)_2 \cdot 6\text{H}_2\text{O}$. The solution turned purple immediately, and the resultant mixture was stirred for 2 h at room temperature. The product was collected by centrifugation and was washed with methanol for three times to remove excess 2-mlm, and then dried at room temperature under vacuum overnight.

To synthesize the CNT/CoS nanocages, 50 mg CNTs were preprocessed with polyvinylpyrrolidone (PVP, 300 mg) in methanol (42.85 mL) for achieving good dispersion of CNTs first. At the same time, $\text{Co}(\text{NO}_3)_2 \cdot 6\text{H}_2\text{O}$ and 2-mlm were both dissolved in methanol separately. Then, the solution consisted of $\text{Co}(\text{NO}_3)_2 \cdot 6\text{H}_2\text{O}$ was added into CNTs solution, followed by the addition of 2-mlm solution. The mass ratio of CNT to ZIF-67 was controlled from 1:1 to 1:8 under reaction process. After stirring for 2 h at room temperature, centrifuged the resultant mixture and washed with methanol for three times. Then dried the sample at room temperature under vacuum overnight. The samples were labelled as CNT/ZIF-67 1:1, CNT/ZIF-67 1:2, CNT/ZIF-67 1:8, respectively. The as-prepared ZIF-67 and CNT/ZIF-67 with various mass ratios were transferred into a round-bottomed flask containing thioacetamide with a molar ratio of 1 to 5, dissolved in ethylene glycol. Then the mixture was refluxed with stirring at 180 °C for 2 h. Finally, the black product was collected by centrifugation, washed with ethanol for three times, and dried at 180 °C under vacuum overnight. The products were denoted as CoS, CNT/CoS 1:1, CNT/CoS 1:2, and CNT/CoS 1:8, which correspond to the mass ratio of CNT to CoS, 0, 1, 1/2, 1/8, respectively. Also, CNT/CoS mixture was prepared by physical mixing of CNTs and CoS directly with a mass ratio of 1 to 2 for comparison.

2-3-2 Preparation of electrode with electroactive materials for SCs

Ni foam (Fucell energy Co. Ltd., Taoyuan, Taiwan, thickness = 1.7 mm, porosity = 110 pores

per inch (PPI)) served as the substrate and the current collector of the SCs. Therefore, before the deposition, it should be completely cleaned to avoid the impurities that could affect the experiment. Firstly, the received pristine Ni foam was cut into pieces with a size of 1 cm × 2.5 cm. Then the small pieces of Ni foam were ultrasonically cleaned in 1.0 M HCl and DIW sequentially for 25 and 15 minutes, respectively. After cleaning, the substrates were dried at 90 °C on a hot plate, followed by plasma treatment with an argon plasma cleaner (Electronic diener, FEMTO Beispiel Variante 3, Ebhausen, Germany). The epoxy tapes (3M Company, 60 μm thick) were used to control the active electrode area of 1 cm × 1 cm. The modified electrodes were drop-coated with as-prepared slurries (2.5 mg mL⁻¹) and then dried at 90 °C with a hot plate. Each electrode contained 1 mg cm⁻² of electroactive material.

2-4 Analytic techniques

2-4-1 Material characterizations

Surface morphology of the films was observed by a field-emission scanning electron microscope (FE-SEM, Nova NanoSEM 230, FEI, Oregon, USA), equipped with an energy dispersive X-ray spectroscopy (EDS, model 7021-H, Horiba, Kyoto, Japan). Surface chemical analysis of the films were performed by X-ray photoelectron spectroscopy (XPS, Thermo Scientific Theta Probe, East Grinstead, UK). X-ray diffraction (XRD) patterns of the powders were obtained by an X-ray diffractometer (Rigaku, Japan). The sheet resistance (R_{sh} , relating the electrical conductivity) was measured by a four-point probe (Keithley 2400, Keithley Instruments Inc., Beaverton, Oregon, USA). The decomposition temperature was measured by a thermogravimetric analyzer (TGA, Perkin-Elmer, Waltham, Massachusetts, USA). The Raman spectra were analyzed by Dimension Raman System (Lambaba Solution, Inc.; P2 type, Waltham, Massachusetts, USA). N₂ adsorption-desorption was measured via a Micromeritics ASAP 2020 instrument (Micromeritics, Norcross, Georgia, USA).

2-4-2 Photovoltaic properties for DSSCs

(1) Definition of air mass (AM)

The solar spectrum and irradiance is based on the air mass (AM), which is defined as the path length of light normalized to its shortest path length in the atmosphere. As shown in **Figure 2-1**, the radiation of sunlight, which is overhead to the horizontal line, is called AM 1. AM 1.5 is a typical solar spectrum on the Earth's surface which is commonly used for the measurement of solar cells and modules. Moreover, the light intensity of AM 1.5 is estimated approximately about 100 mW cm^{-2} which is often used to represent AM 1.5 in literatures.

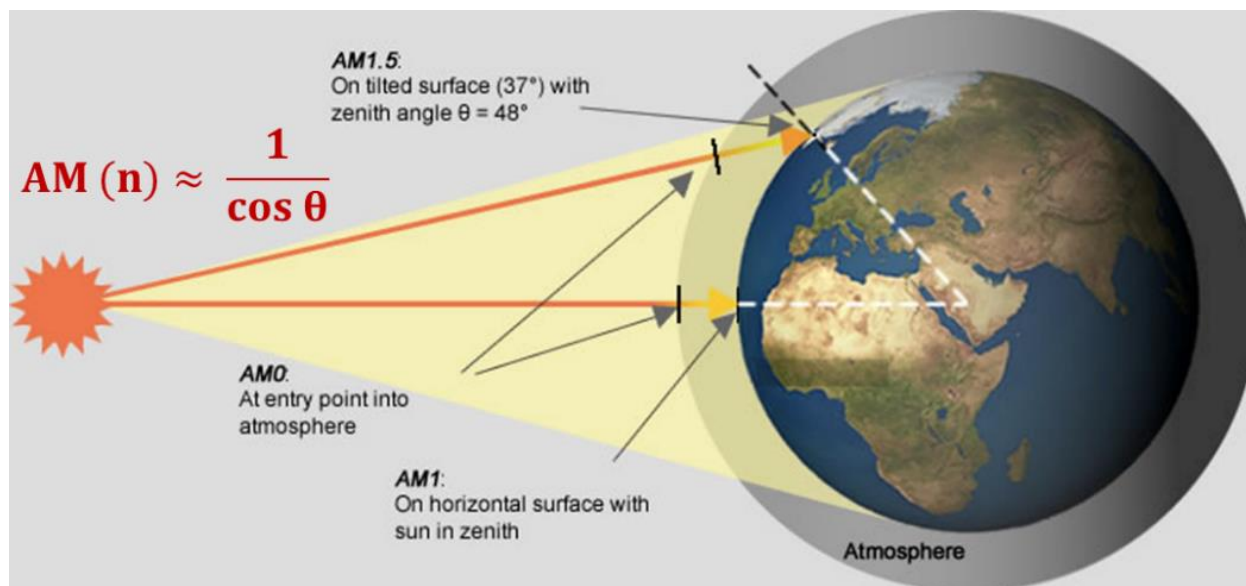


Figure 2-1 Air mass (AM) definition and the equation corresponding to zenith angle. (from Green Rhino Energy, <http://www.greenrhinoenergy.com/solar/radiation/spectra.php>)

(2) Photocurrent density-voltage curve (J - V curve)

Photovoltaic parameters and incident photon-to-current conversion efficiency (IPCE) spectra of DSSCs for the cells with different CEs were recorded by a potentiostat/galvanostat (PGSTAT 30, Autolab Eco-Chemie, Utrecht, the Netherlands). The cell conversion efficiency (η) of a DSSC was obtained under a light illumination of 100 mW cm^{-2} (calibrated with a standard Si cell, PECSI01, Peccell Technologies, Inc., Kanagawa, Japan), using a class A quality solar simulator (XES-301S, AM1.5G, San-Ei Electric Co. Ltd., Osaka, Japan). Accordingly, the power conversion efficiency (PCE, η) of a DSSC is calculated by its values of short-circuit photo-current density (J_{SC}), open-circuit photo-voltage (V_{OC}), fill factor (FF), and the power of incident light (P_{in}), as shown in

Equation 2-1. Here, the FF value (between 0 and 1) is defined as a ratio of the practical maximum power output (P_{max}) to an ideal maximum power output ($J_{SC} \times V_{OC}$) of a cell per unit area, as shown in **Equation 2-2**. Also, **Figure 2-2** illustrate the above-mentioned equations.

$$\eta (\%) = \frac{P_{max}}{P_{in}} \times 100\% = \frac{J_{sc}(\text{mA cm}^{-2}) \times V_{oc}(\text{V}) \times FF}{P_{in}(\text{mW cm}^{-2})} \times 100\% \quad (2-1)$$

$$FF = \frac{P_{max}}{J_{sc} \times V_{oc}} \quad (2-2)$$

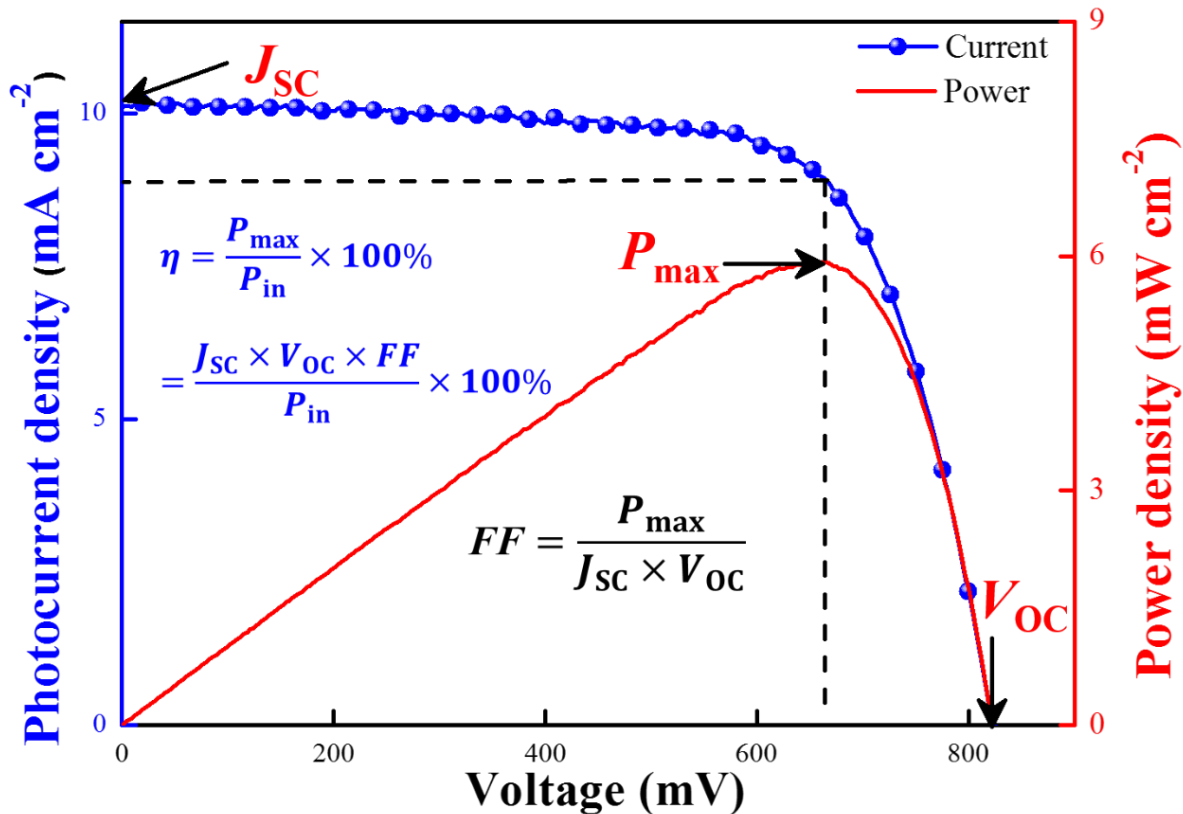


Figure 2-2 Illustrate the parameters of the J - V curves.

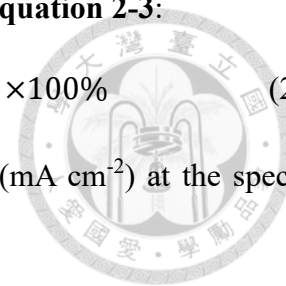
(2) Monochromatic incident photon-to-current conversion efficiency (IPCE)

The IPCE curves of the DSSCs were obtained in the wavelength range of 400 to 800 nm by another class A quality solar simulator (PEC-L11, AM1.5G, Peccell Technologies, Inc., Kanagawa, Japan), equipped with a monochromator (model 74100, Oriel Instrument, California, USA). The incident radiation flux (ϕ) was recorded by an optical detector (model 818-SL, Newport, California, USA) and a power meter (model 1916-R, Newport, California, USA). The IPCE of a dye-sensitized solar cell is defined as the ratio of the electrons produced in the external circuit at a given wavelength

to the incident photons under a short-circuit condition; it is expressed as **Equation 2-3**:

$$\text{IPCE (\%)} = \frac{\text{number of electrons}}{\text{number of incident photons}} \times 100\% = \frac{1240 \times J_{\text{SC}}}{\lambda \times \phi} \times 100\% \quad (2-3)$$

where λ is the wavelength, J_{SC} is the short-circuit photocurrent density (mA cm^{-2}) at the specific wavelength, and ϕ is the incident radiation flux (mW cm^{-2}).



2-4-3 Electrochemical properties for DSSCs

(1) Cyclic voltammetry (CV)

CV analysis was obtained from the same potentiostat/galvanostat mentioned above using a three-electrode electrochemical system, consisted of an electrocatalytic film (1 cm^2), a Pt foil, and a Ag/Ag^+ that were used as the working, counter, and reference electrodes, respectively. The electrolyte for the CV analysis contained 1.0 mM I_2 , 10.0 mM LiI , and 0.1 M LiClO_4 in ACN. CV analysis was applied to investigate the redox kinetics of iodide/triiodide (I^-/I_3^-) at the surface of an electro-catalytic film. Via scanning from -0.6 to 0.4 V (vs. Ag/Ag^+) at a scan rate of 100 mV s^{-1} , one pair of the redox peaks can be observed. The anodic and cathodic peaks can be represented by **Equation 2-4** and **2-5**, respectively,



As a CE in a DSSC, an electrocatalytic film is specifically designed to facilitate the reduction of I_3^- at the CEs/electrolyte interface. The overdose I_3^- causes the severe charge recombination at the photoanode/electrolyte interface, thereby losing the energy of a cell. Therefore, we focus on investigating the cathodic peak current density (J_{pc}) and the peak separation (ΔE_{p}) of a CV curve; the larger J_{pc} and the smaller ΔE_{p} reflect the better overall electrocatalytic ability of a film for I_3^- reduction.

(2) Rotating disk electrode (RDE)

RDE analysis were recorded by a potentiostat (model 900B, CHI Instruments) equipped with a modulated speed rotator (MSR, PINE Instrument Company, Grove, Pennsylvania, USA) in an ACN

solution containing 0.1 M LiClO₄ and 1.0 mM TBAI₃. An electrocatalytic film was coated on a glassy carbon electrode (GCE, Part #AFE7R9GCGC, PINE Instrument Company) as the working electrode; another electrode with Pt as the disk material (Pt-RDE, working area: 0.196 cm², Part #AFE2M050PT, PINE Instrument Company) was also used as the working electrode for estimating the parameters related to Pt electrode. A Pt wire and an Ag/Ag⁺ electrode were used as the counter and reference electrodes, respectively. RDE analysis was applied to determine two important indexes, *i.e.*, the intrinsic heterogeneous rate constant (k^0) and the effective electrocatalytic surface area (A_e); both parameters influence the overall electrocatalytic ability of a film. At the formal potential (E^0) of the I⁻/I₃⁻, various values of reciprocal current (i^{-1}) can be obtained from the linear sweep voltammetry (LSV) curves for a specific electrode at various rotating speeds (50, 100, 200, 400, 600, 800, and 1000 rpm), using a scan rate of 2 mV s⁻¹. According to a simplified Koutecký–Levich equation (**Equation 2-6**), a plot of reciprocal current (i^{-1}) vs. reciprocal of rotating rate root ($\omega^{-0.5}$) for an electrocatalytic film was used to calculate the values of k^0 and A_e by its intercept and the slope, respectively.⁶²

$$\frac{1}{i} = \frac{1}{nFA_e k^0 C} + \frac{1}{0.62nFA_e D^{2/3} \nu^{-1/6} \omega^{1/2} C} \quad (2-6)$$

where i is the disk current obtained at the formal potential (E^0) of I⁻/I₃⁻, n is the number of electrons transferred for I₃⁻ reduction, F is the Faraday constant, C is the bulk concentration of I₃⁻ (1.0 mM), D is the diffusion coefficient of I₃⁻ (3.62×10⁻⁶ cm² s⁻¹), ν is the kinematic viscosity of the electrolyte, and ω is the angular velocity converted from the rotating speed.

(3) Tafel polarization plot (Tafel)

Tafel analysis was performed by the same potentiostat/galvanostat mentioned above, with a FRA2 module, by using a symmetric cell consisting of the same films on both anode and cathode; the electrolyte consisted of 0.1 M LiI, 0.6 M DMPII, 0.05 M I₂, and 0.5 M tBP in MPN/ACN (volume ratio of 1/1). For an electrocatalytic film, a linear sweep voltammetry (LSV) curve is measured at a low scan rate of 50 mV s⁻¹; and the pertinent Tafel polarization plot is shown as a logarithmic current

density–voltage ($\text{Log } J-V$) curve. Tafel analysis aims to explore the practical electrocatalytic ability of a film for I_3^- reduction in an electrolyte for the DSSCs (with high I^-/I_3^- concentration). From the Tafel plot, the exchange current density (J_0) of an electrocatalytic film can be obtained by extrapolating the anodic and cathodic curves in the Tafel zone and reading the cross point at 0 V. The higher value of J_0 indicates the better electrocatalytic ability of the film. In addition, the J_0 value of a film can be further used to calculate the charge transfer resistance ($R_{\text{ct-Tafel}}$) corresponding to the electrocatalytic film/electrolyte interface, as shown in **Equation 2-7**. The smaller $R_{\text{ct-Tafel}}$ value refers to a larger amount of electrons transferring through the electrocatalytic film/electrolyte interface, and thereby implies a faster electron transfer capability of the film.⁶³

$$J_0 = \frac{RT}{nFR_{\text{ct-Tafel}}} \quad (2-7)$$

where R is the ideal gas constant, T is the absolute temperature, F is Faraday constant, n is the number of electrons transferred for I_3^- reduction.

(3) Electrochemical impedance spectroscopy (EIS)

EIS analysis was performed by the above-mentioned potentiostat/galvanostat equipped FRA2 module and was measured between 10 mHz to 65 kHz with an AC amplitude of ± 10 mV using a symmetric cell of an electrocatalytic film. The EIS analysis aims to precisely investigate the interfacial resistances, namely series resistance (R_s) and charge transfer resistance ($R_{\text{ct-EIS}}$). According to the equivalent circuit shown in **Figure 2-3**, the R_s value equals to onset point of the semicircle on left-hand side in the high frequency region ($10^6 \sim 10^5$ Hz); the lower R_s reflects the better ohmic contact between the substrate and an electrocatalytic film. The $R_{\text{ct-EIS}}$ is obtained from the radius of the semicircle in the middle frequency region ($10^5 \sim 10^1$ Hz); the lower $R_{\text{ct-EIS}}$ refers to the larger amount of charges pass through the electrocatalytic film/electrolyte interface.

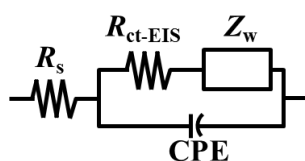


Figure 2-3 The equivalent circuit of a symmetric cell of an electrocatalytic film.



2-4-4 Electrochemical properties for SCs

The electrochemical measurements, including cyclic voltammetry (CV) and galvanostatic charge-discharge (GCD) were performed with a CHI 440 electrochemical workstation (CH Instruments, Inc., Austin, TX, USA). Electrochemical impedance spectroscopy (EIS) analysis was carried out using a potentiostat/galvanostat (PGSTAT 30, Autolab Eco-Chemie, Utrecht, the Netherlands). All electrochemical measurements were conducted on a standard three-electrode system in 6.0 M KOH aqueous solution, using Ni foam substrates modified with as-prepared materials, a Pt foil (1 cm × 4 cm) and reversible hydrogen electrode (RHE) as the working electrode, counter electrode and reference electrode, respectively. The potentials *vs.* RHE were converted to the mercury/mercury oxide electrode (Hg/HgO) using **Equation 2-8**,

$$E_{\text{RHE}} = E_{\text{Hg/HgO}} + 0.059\text{pH} + E_{\text{Hg/HgO}}^{\circ} \quad (2-8)$$

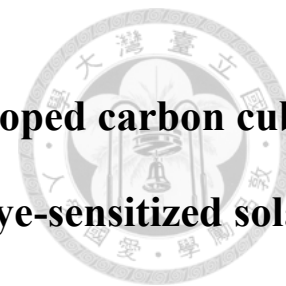
where $E_{\text{Hg/HgO}}$ is the converted potential *vs.* Hg/HgO, $E_{\text{Hg/HgO}}^{\circ} = 0.098$ V at 25 °C, and E_{RHE} is the experimentally measured potential against RHE reference. CV curves were obtained in the scan range from -0.07 to 0.63 V under various scan rates, and GCD curves were carried out in the potential window of 0.08 to 0.48 V under different current densities. EIS was performed in the same platform with the frequency range from 10 kHz to 0.1 Hz. Specific capacitance values were calculated from GCD results using **Equation 2-9**:

$$C_g = \frac{I \times \Delta t}{m \times \Delta V} \quad (2-9)$$

where C_g is the gravimetric capacitance (F g^{-1}), I is the current (A), Δt is the discharge time (s), m is the mass of the active electrode materials (g), and ΔV is the potential window (V).

Chapter 3

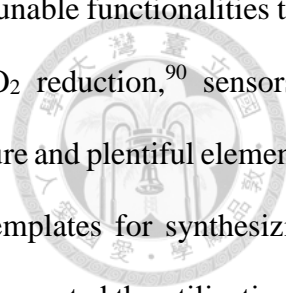
A zeolitic imidazolate framework-derived ZnSe/N-doped carbon cube hybrid electrocatalyst as the counter electrode for dye-sensitized solar cells



3-1 Introduction and motivation

Sunlight is considered to be promising green energy to replace traditional petroleum fuels since it was the most abundant energy resource on the earth.⁶⁴ Till now, innumerable scientists and engineers have been exploring various kinds of solar cells, such as silicon solar cells,⁶⁵ organic solar cells,⁶⁶ quantum dot solar cells,^{67, 68} dye-sensitized solar cells (DSSCs),^{64, 69, 70} perovskite solar cells,⁷¹ and so on, that can convert solar energy into electricity. Among these photovoltaic cells, DSSCs with the possible advantages of low manufacturing cost and simple fabrication process have attracted extensive attention since the pioneered work reported by M. Grätzel group.⁶⁹ The same group has recently reported a DSSC that achieves a very high photovoltaic conversion efficiency of 28.9% under ambient light conditions.⁷² Typical DSSCs are composed of three independent components, namely, dye-sensitized nanocrystalline TiO₂ film as the photoanode, an electrocatalytic material as the counter electrode (CE), and an electrolyte consisting of a redox couple. Among them, the CE works for regenerating the I⁻ ion to keep the function of DSSCs. In other words, the development of an efficient CE with highly electrocatalytic activities plays a crucial role in DSSCs.^{73, 74} Pt, with its outstanding electrocatalytic ability and high conductivity, has been widely used as a CE in DSSCs for realizing the high photovoltaic conversion efficiency.^{75, 76} So far, several alternatives, including carbonaceous materials,⁷⁷⁻⁷⁹ conducting polymers,^{35, 80} and transition metal-containing materials^{81, 82}, have been proposed to replace Pt since the high-cost issue of Pt still limited the development of DSSCs in industrials.

Recently, metal-organic frameworks (MOFs), which consist of metallic clusters as the nodes and organic ligands as the linkers, have received rather broad attention as a novel class of materials



possessing ultrahigh specific surface area, unique structural topology, and tunable functionalities that are useful for gas absorption,⁸³⁻⁸⁵ gas separation,^{86, 87} catalyst,^{88, 89} CO₂ reduction,⁹⁰ sensors,⁹¹ supercapacitors,^{92,93} and so on. Moreover, highly ordered framework structure and plentiful elemental composition of MOFs can be used as unique precursors or sacrificial templates for synthesizing various nanomaterials with novel characteristics. For example, Dai's group reported the utilization of MOFs as a template for synthesizing N, P, and S ternary-doped metal-free porous carbon materials, which were used as electrocatalysts for ORR.⁹⁴ Zeolitic imidazolate frameworks (ZIFs), which composed of tetrahedrally-coordinate transition metal ions (Co, Cu, Zn, *etc*) connected by imidazolate linkers, represent a class of MOFs that are topologically isomorphic with zeolites since the angle (~145°) of the metal connected by imidazolate linkers is similar to zeolites. Electrical conductivity and electrocatalytic ability of ZIF-derived materials can be improved by calcination process.⁹⁵⁻⁹⁷ The rich nitrogen-containing imidazolate ligands of ZIFs provide both carbon and nitrogen sources, thus making ZIFs an excellent candidate for synthesizing N-doped porous carbons through direct carbonization. In addition, compared to other N-doped carbons,⁹⁸⁻¹⁰⁰ carbonaceous materials derived from ZIFs can retain the advantages of porous structures of ZIFs. Moreover, tunnel structure is crucial to the diffusion of electrolyte and its high specific surface area is beneficial to the catalytic reactions. ZIF derived materials have received tremendous attention in many aspects, such as gas absorption,¹⁰¹ oxygen reduction,¹⁰² and supercapacitors.¹⁰³⁻¹⁰⁶ Taking supercapacitors as an example, Salunkhe *et al.* used nanoporous carbon derived from ZIF-8 as the core for growing polyaniline nanorod, and the composites achieved high capacitance performance for supercapacitors¹⁰³. Kim *et al.* prepared hybrid ZIF carbon from two ZIFs, having two different metal ions. The hybrid product possesses the advantages of both ZIF-8 (Zn²⁺) and ZIF-67 (Co²⁺), thus offering attractive properties for application in supercapacitors.¹⁰⁵

Nevertheless, only a few literatures mentioned about their application in the field of DSSCs.¹⁰⁷⁻¹⁰⁹ Sun *et al.* synthesized ZIF-8 derived carbon materials as a counter electrode (CE) of DSSCs owing to their large specific surface area and high electrocatalytic abilities towards the reduction of I₃⁻ ions; the DSSC with ZIF-8 derived carbon materials CE exhibits a photovoltaic conversion efficiency (η)

of 7.32%, which is comparable to that of the Pt CE (7.53%).¹⁰⁷ Moreover, metallic compound decorated ZIF-derived materials can be synthesized spontaneously by calcination process since the metallic nodes in the frameworks also serve as the metallic precursor. For instance, Jing *et al.* used ZIF-67 as a self-template in a facile pyrolysis synthesis of metal nanoparticles embodied in an N-doped porous graphitic carbon with surface-oxidized CoO. The DSSC performance of the cell with ZIF-67-850 (pyrolyzed at 850 °C) CE shows an η of 7.92%, which is close to that of the Pt CE (8.18%).¹⁰⁸ Cui *et al.* also used ZIF-67 derived CoS₂ embedded carbon nanocages as a CE of DSSCs; the DSSC consisting of CoS₂ embedded carbon nanocages achieves an η of 8.20%, which exceeds that of the Pt-based DSSC (7.88%).¹⁰⁹

Recently, transition metal compounds, such as carbides, nitrides, oxides, sulfides, phosphides, selenides, and tellurides, have gotten lots of attention due to their attractive advantages, e.g., low-cost, excellent electrochemical activity, good conductivity, and good stability.^{81, 110, 111} According to our previous results, we found that among many transition metal compounds, transition metal selenides give the best electrocatalytic ability to their counter electrodes and thus provide the highest performance to the DSSCs.¹¹² Lee *et al.* also reported that the DSSC with a MoSe₂ CE shows an η of 9.00%, which is higher than that of the cell with a MoS₂ CE (8.69%).¹¹³ Zhu *et al.* proposed a ZnSe-graphene (ZnSe-rGO) nanocomposites as the CE by using a facile hydrothermal method;¹¹⁴ the DSSC with ZnSe-rGO CE shows an η of 6.61%, which is comparable to that of the Pt CE (6.23%). Evoking by our previous experience, ZIF-7 derived ZnSe/N-doped carbon cube (ZIF-ZnSe-NC) hybrid electrocatalyst is proposed for the first time in this work as the CE in DSSCs. As shown in **Figure 3-1**, the home-made ZIF-7 powder is first fabricated by an eco-friendly method using ethanol as the solvent. After that, carbonization and selenization under different temperatures for synthesizing ZIF-7 derived N-doped carbon cube (ZIF-NC) and ZIF-7 derived ZnSe/N-doped carbon cube (ZIF-ZnSe-NC) were proceeded step by step. In ZIF-ZnSe-NC hybrid electrocatalyst, N-doped carbon cube is beneficial to the electrocatalytic performance and the electrical conductivity. Meanwhile, embedded ZnSe in carbon matrix also serves as the additional active sites for facilitating I₃⁻ reduction. After optimizing the weight percentage of ZIF-ZnSe-NC film (~11 wt%), the DSSCs with ZIF-ZnSe-NC-

11 wt% CE exhibits the best η of $8.69 \pm 0.13\%$, which is higher than that of the cell with a Pt CE ($8.26 \pm 0.02\%$), showing a high potential to replace the expensive Pt. The results of cyclic voltammetry, Koutecký-Levich plot, electrochemical impedance spectroscopy, and Tafel polarization plots provide substantial evidence to explain the higher η value of the cell with ZIF-ZnSe-NC CE, which is attributed to the outstanding electrocatalytic ability for reducing the I_3^- , thus minimizing the charge-transfer resistance at the CE/electrolyte interface. **Table 3-1** summarizes the performance of the reported DSSCs using various ZIF-derived CEs and ZnSe CEs, as compared to that obtained in this work.

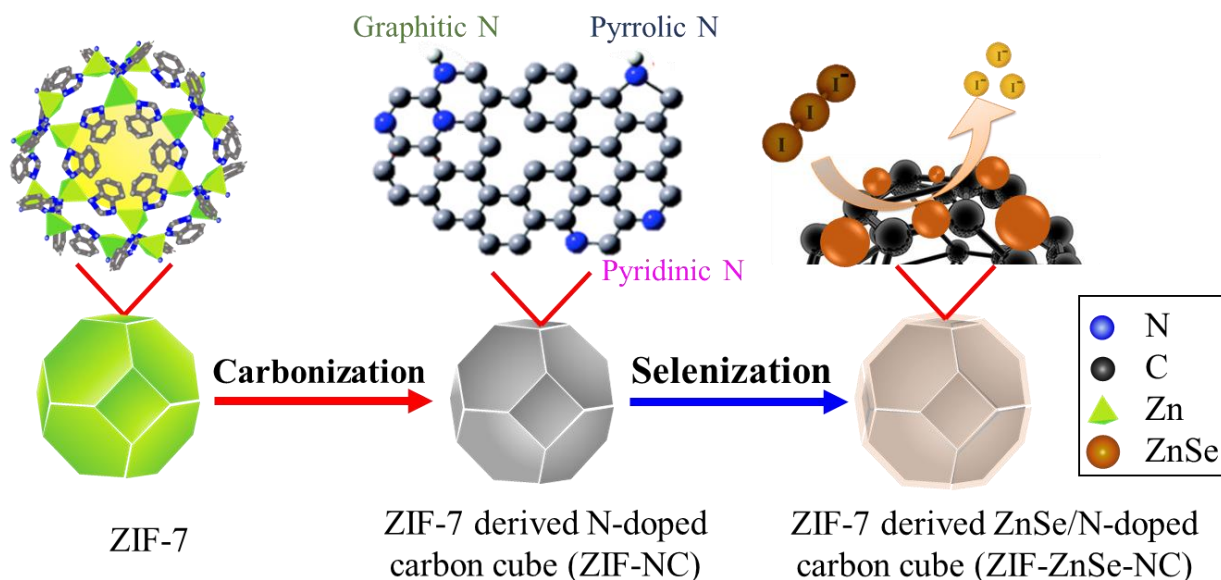


Figure 3-1 The sketch of the process from ZIF-7 to ZIF-derived materials.

Table 3-1 The performance of the reported DSSCs using various ZIF-derived CEs and ZnSe CEs, as compared to that obtained in this work. ^a ZIF-derived counter electrodes. ^b ZnSe counter electrodes (not derived from ZIFs).

Counter electrode	Metal	η (%)	η_{Pt} (%)	V_{oc} (V)	J_{sc} (mA cm ⁻²)	FF	Ref.
ZIF-8 derived carbons ^a	Zn	7.32	7.53	0.77	13.56	0.68	107
ZIF-67 derived carbons ^a	Co	7.92	8.18	0.80	13.29	0.74	108
ZIF-67 derived CoS ₂ ^a embedded carbon nanocages ^a	Co	8.20	7.88	0.73	16.90	0.66	109
ZnSe/rGO ^b		6.61	6.23	0.78	15.00	0.57	114
ZIF-67 derived CoS ^a	Co	8.10	8.00	0.78	14.70	0.71	115
ZnSe-10 ^b		8.13	8.59	0.77	15.72	0.68	116
Cu ₂ ZnSnSe ₄ ^b		8.22	7.56	N.A.	N.A.	N.A.	117
ZIF-7 derived ZnSe-NC ^a	Zn	8.69	8.26	0.77	16.40	0.69	This work

3-2 Results and discussions

3-2-1 Characterization of the as-synthesized ZIF-7

ZIF-7 is composed of zinc cluster connected by benzimidazolate (bIM) ligand in sodalite (SOD) topology structure, as illustrated in **Figure 3-2a**. **Figure 3-2b** shows the SEM image of as-synthesized ZIF-7, which are uniform micrometer-sized spherical crystals composed of smaller irregular particles. The as-synthesized ZIF-7 particles do not possess well-defined crystal faces compared with those prepared in DMF,¹¹⁸ which presumably is caused by rapid deprotonation of organic ligands in ethanol/ammonium hydroxide solution and resulted in anisotropic crystal growth.⁸ **Figure 3-2c** shows the XRD pattern of as-synthesized ZIF-7; the peaks are highly consistent with the reported XRD pattern of simulated ZIF-7.¹¹⁹ The N₂ adsorption-desorption isotherm of ZIF-7 is shown in **Figure 3-2d**. As expected, the Brunauer-Emmett-Teller (BET) surface area of ZIF-7 is only 5.14 m² g⁻¹. This phenomenon has been observed previously,^{8, 120} suggesting that the pore sizes of ZIF-7 are so small that N₂ could not enter the window of ZIF-7 and they are only absorbed on the external surface.

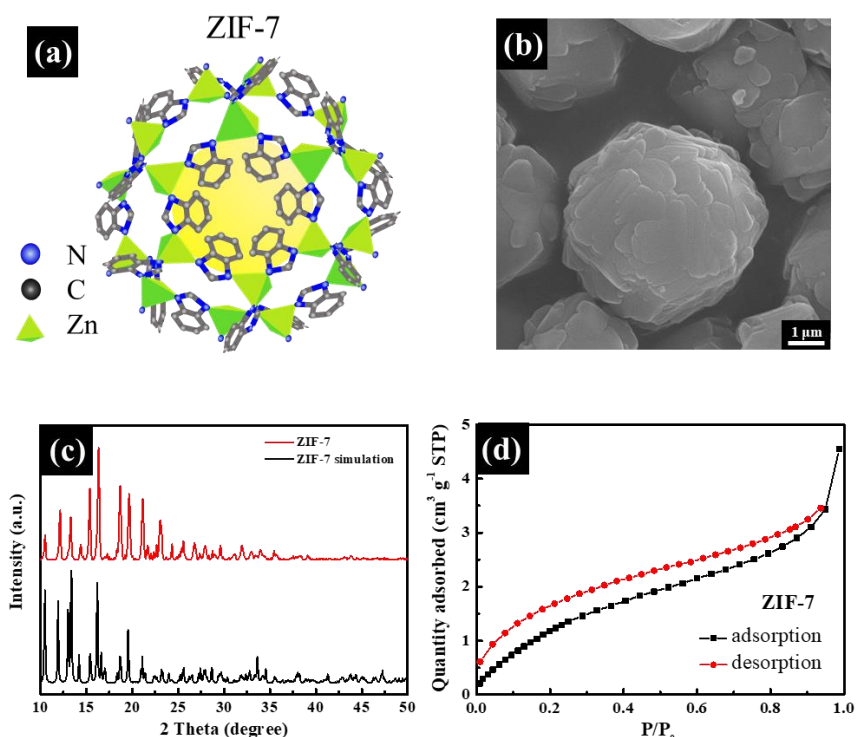


Figure 3-2 (a) Schematic illustration, (b) FE-SEM image, (c) XRD pattern, and (d) N₂ adsorption-desorption isotherms of as-synthesized ZIF-7.

3-2-2 Characterization of carbonized ZIF-7 under various calcination temperatures

To understand the carbonization effect of ZIF-7, ZIF-7 with various calcination temperatures was studied at the beginning. **Figure 3-3a** gives the TGA curve of the ZIF-7 sample. The mass loss during the temperature range of 200-400 °C is attributed to the evaporation of solvents remaining in the pores of ZIF-7. After that, there is a weight-loss step corresponds to the decomposition of the framework at ~ 650 °C. The colors of the powder under different calcination temperatures (600, 700, 800, 900, 1000 °C) are shown in the inset of **Figure 3-3a**. The color of the ZIF-NC powder carbonized under 600 °C is khaki, which is different from the colors of ZIF-NC powder processed at other temperatures, suggesting that it is not sufficiently being carbonized. Raman spectra were performed to investigate the degree of graphitization of the ZIF-NC further. As shown in **Figure 3-3b**, two peaks detected at 1346 cm⁻¹ and 1585 cm⁻¹ were related to D and G bands of the carbon, respectively. The D band is due to out of plane vibrations attributed to the presence of structural defects, while the G band is a result of in-plane vibrations of sp² bonded carbon atoms. The intensity ratio of the D band to G band (I_D/I_G) illustrates relates to the amount of structurally ordered graphite crystallites in the carbonaceous materials. No noticeable peak of ZIF-NC-600 °C can be obtained, once again confirmed that it had not adequately carbonized yet. The I_D/I_G ratio of ZIF-NC gradually decreased from 1.099 to 1.024 with the calcination temperatures increased from 700 to 1000 °C, which indicates that some carbonaceous disorders were converted into ordered graphite crystallites while elevating the temperature. Higher temperatures will enhance the degree of graphitization but reduce oxygen-containing functional groups on the surface of as-prepared carbonaceous materials, thus accordingly influencing the electrocatalytic performance.^{107, 121}

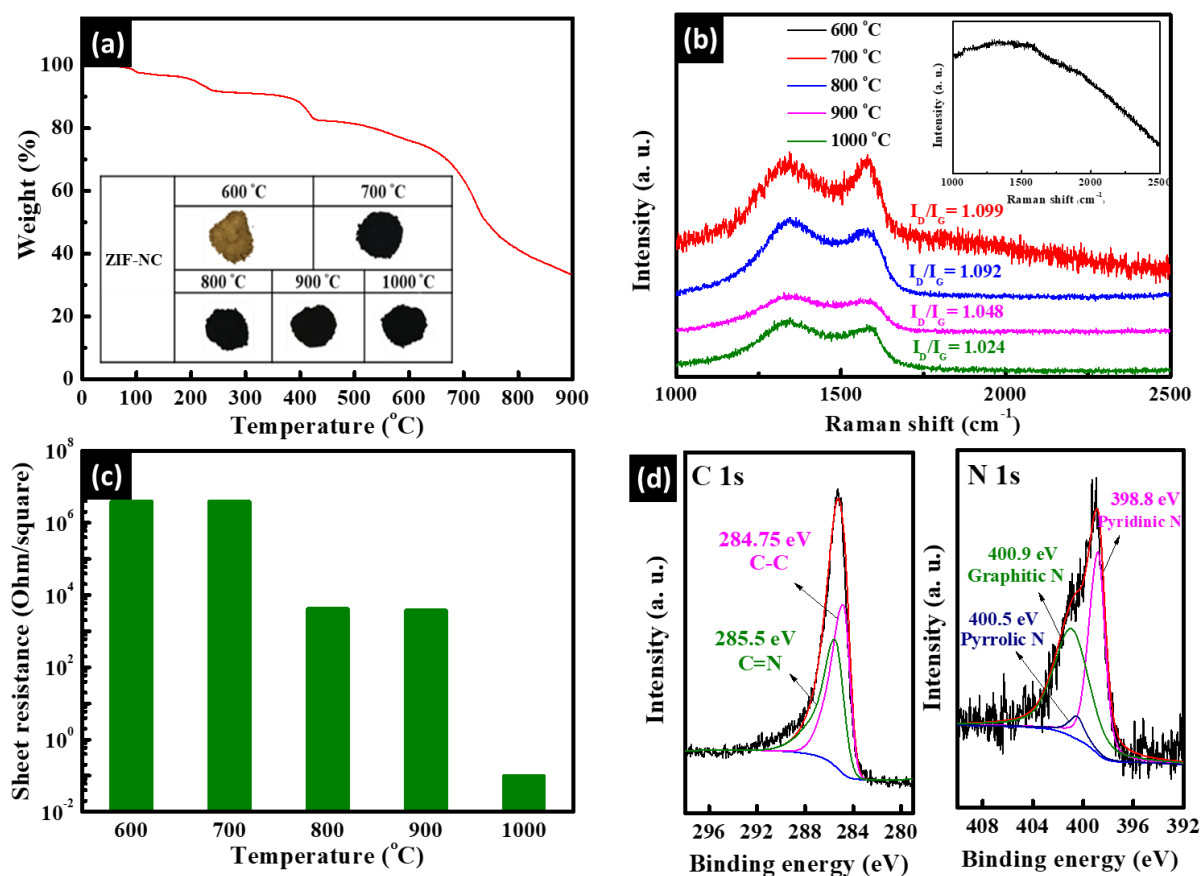


Figure 3-3 (a) TGA plot of ZIF-7 at a temperature rate of $10\text{ }^{\circ}\text{C min}^{-1}$ in an N_2 atmosphere; the pictures of ZIF-NC powder with different carbonization temperatures (600~1000 $^{\circ}\text{C}$) are shown in the inset; (b) Raman spectra and (c) four-point probe analysis of the ZIF-NC with different carbonization temperatures (600~1000 $^{\circ}\text{C}$); (d) C 1s and N 1s XPS spectra of ZIF-NC-900 $^{\circ}\text{C}$.

The sheet resistances (R_{sh}), relating to the electrical conductivities, of different ZIF-NC films (with an average thickness of 20 μm) were measured by a four-point probe method, as shown in **Figure 3-3c**. The data are listed in **Table 3-2**. The R_{sh} values decrease with the increasing temperature, showing that a higher calcination temperature would enhance the electrical conductivity of the ZIF-NC. On the other hand, to confirm the characteristic of N-doped carbon in ZIF-NC, XPS spectra of ZIF-NC-900 $^{\circ}\text{C}$ for their C 1s orbitals and N 1s orbitals are shown in **Figure 3-3d**. The C 1s spectrum can be divided into two peaks. The peak at 284.75 eV is assigned to C-C, while the peak at 285.5 eV is attributed to C=N. The N 1s spectrum can also be divided into three peaks. The peak at 398.8 eV is related to pyridinic nitrogen, referring to sp^2 -nitrogen bonded to two carbon atoms. The peak at

400.9 eV is assigned to graphitic nitrogen. There is a lower peak at 400.5 eV, which is attributed to pyrrolic nitrogen. Inferred from these results, the ZIF-NC-900 °C was comprised of pyridinic nitrogen (45.0%) and graphitic nitrogen (49.6%). These two types of nitrogen would form active sites for promoting the triiodide reduction reaction and could reduce the redox potential.¹²² Moreover, the BET surface area of ZIF-NC-900 °C is 65.89 m² g⁻¹ (**Figure 3-4a**), which is higher than that of ZIF-7 since the pore sizes of carbonized ZIF-7 are larger for N₂ penetrating into the structure.⁹² The XRD pattern of ZIF-NC-900 °C (**Figure 3-4b**) also displays two broad peaks at around 22 and 43°, suggesting the amorphous structure of the carbon.

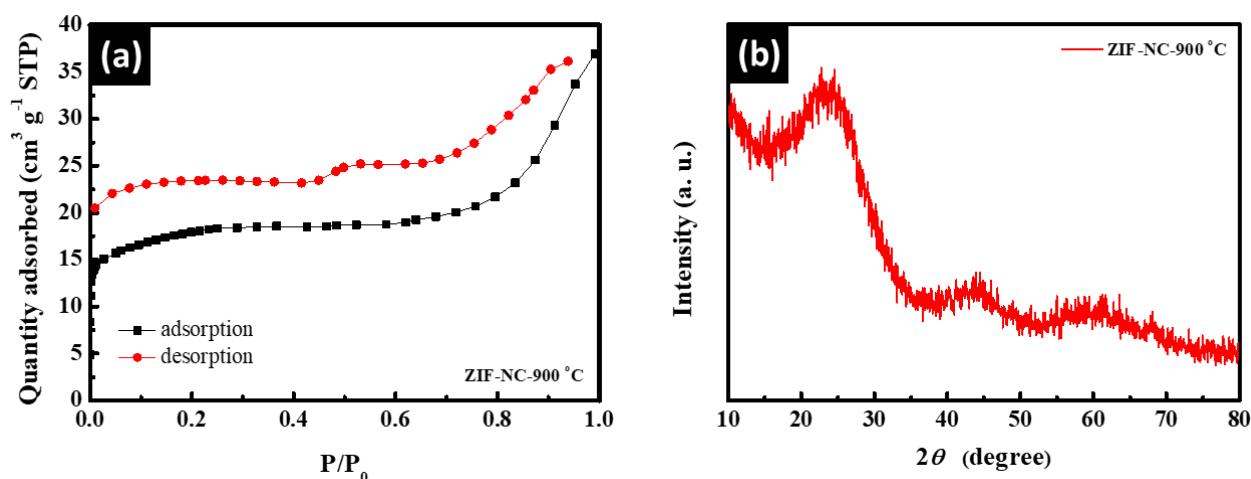


Figure 3-4 (a) N₂ adsorption-desorption isotherms and (b) XRD pattern of ZIF-NC-900 °C powder.

Figure 3-5a shows photocurrent density-voltage (*J-V*) curves of the DSSCs with the CEs of ZIF-NC treated at various carbonization temperatures (600~1000 °C). The pertinent photovoltaic parameters with standard deviations are listed in **Table 3-2**. After optimizing the carbonization temperature of ZIF-NC, the cell with ZIF-NC-900 °C composite film exhibits the best photovoltaic conversion efficiency (η) of $6.02 \pm 0.03\%$ with an open-circuit voltage (V_{OC}) of 0.74 ± 0.00 V, a short-circuit current density (J_{SC}) of 12.27 ± 0.29 mA cm⁻², and a fill factor (FF) of 0.66 ± 0.01 (**Table 3-2**). Although ZIF-NC-1000 °C with higher graphitization shows the lowest values of I_D/I_G and R_{sh} ,

the DSSC performance of the cell using ZIF-NC-1000 °C is harmed by the collapse of the ZIF-NC polyhedral. As clearly shown in **Figure 3-5b**, the morphology of the as-prepared carbonaceous material is consistent with the original structure of ZIF-7 when the calcination temperature is lower than 1000 °C. However, the morphology structure of the ZIF-NC is crumble and could not be preserved to its original ZIF-7 once the temperature is raised to 1000 °C, thus significantly influences the DSSC performance. With the higher calcination temperature, the electrical conductivity of the materials would increase (**Table 3-2**) as the morphology of ZIF-7-NC may collapse (**Figure 3-5b**). According to the above results, carbonization temperature of 900 °C was selected as the best condition for carbonizing the ZIF-7.

Table 3-2 The photovoltaic parameters of the DSSCs with ZIF-NC CEs prepared under different carbonization temperatures, measured at 100 mW cm⁻². Average values and standard deviations were obtained from three independent cells. ^a Measured without PEDOT:PSS.

Samples	η (%)	V_{oc} (V)	J_{sc} (mA cm ⁻²)	FF	R_{sh}^a (Ohm/square)
ZIF-NC-600 °C	4.40 ± 0.05	0.74 ± 0.00	12.04 ± 0.66	0.50 ± 0.03	3.81 × 10 ⁶
ZIF-NC-700 °C	4.78 ± 0.21	0.75 ± 0.00	12.27 ± 0.82	0.52 ± 0.03	3.78 × 10 ⁶
ZIF-NC-800 °C	5.30 ± 0.27	0.74 ± 0.00	12.70 ± 0.10	0.57 ± 0.03	4.06 × 10 ³
ZIF-NC-900 °C	6.02 ± 0.03	0.74 ± 0.00	12.27 ± 0.29	0.66 ± 0.01	3.63 × 10 ³
ZIF-NC1000 °C	3.79 ± 0.05	0.68 ± 0.00	12.70 ± 0.26	0.44 ± 0.01	9.64 × 10 ⁻²

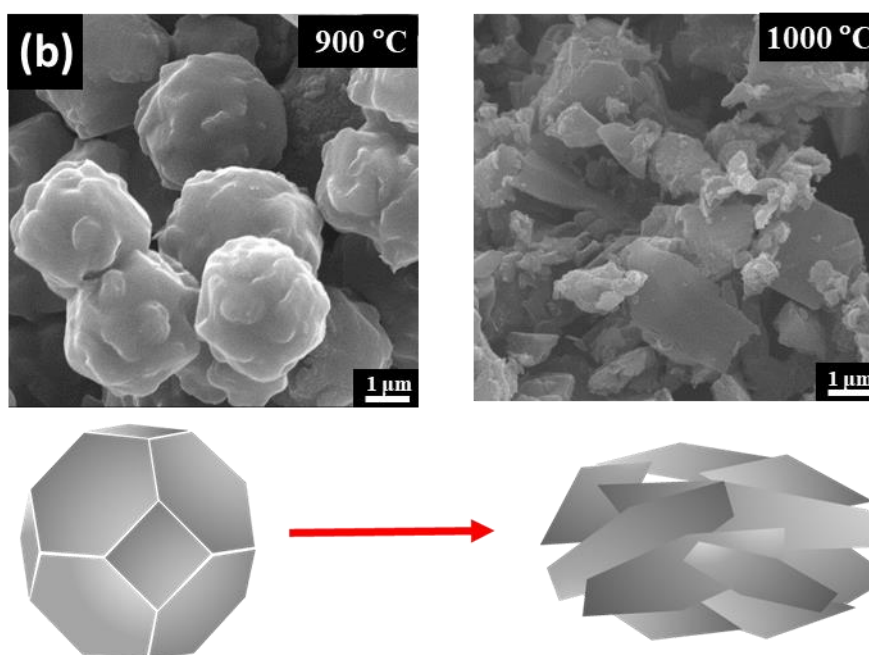
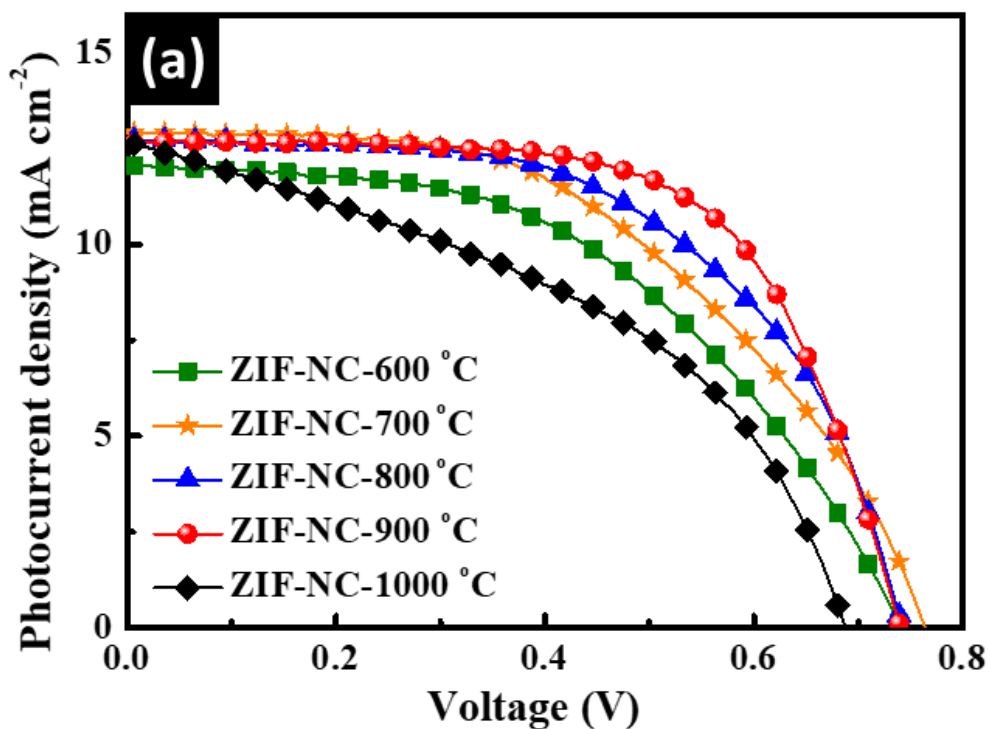


Figure 3-5 (a) Photocurrent density-voltage curves of the DSSCs with the CE of different carbonization temperatures (600~1000 °C) of ZIF-NC films, (b) FE-SEM images of ZIF-NC-900 °C and ZIF-NC-1000 °C; the schematic illustration of collapsed ZIF-NC via annealing process at 1000 °C is also presented.

3-2-3 Characterization of the selenized ZIF-NC under various calcination temperatures

To further improve the electrocatalytic activities of ZIF-NC by increasing the additional active sites, the carbonized ZIF-7 with optimized calcination temperature, namely ZIF-NC-900 °C, was further selenized under different temperatures (300~600 °C). In the XPS survey scan of ZIF-NC before and after selenization at 450 °C (**Figure 3-6a**), it is apparent that the peak of ZIF-ZnSe-NC at 178.7 eV can be assigned to the Auger electron of selenium, where the peak of ZIF-ZnSe-NC at around 54 eV, referring to the Se-Zn chemical bonds of crystalline ZnSe. As shown in the Se 3d spectrum of ZIF-ZnSe-NC (**Figure 3-6a**), there are two split peaks at 54.1 and 54.7 eV for Se 3d_{3/2} and Se 3d_{5/2} respectively, confirming the existence of a Se-Zn bond attributed to the ZnSe formation. **Figure 3-6b** presents the XRD patterns of different selenization temperatures of ZIF-ZnSe-NC, and there are three peaks at 27.3°, 45.3°, and 53.6°, belonging to the cubic phase of ZnSe (JCPDS, card NO. 1-690). The XRD pattern demonstrates that ZIF-ZnSe-NC was successfully synthesized from ZIF-7-NC under various selenization temperatures. For further identifying the percentage of ZnSe in various conditions of the as-prepared samples, the EDS analysis of ZIF-ZnSe-NC under different selenization temperatures was examined, as presented in **Figure 3-6c**. The EDS result shows that the weight percentage of selenium could reach the highest value at 450 °C, implying that ZIF-ZnSe-NC-450 °C has much more electrocatalytic active sites of ZnSe to facilitate the reduction of the I₃⁻. However, the weight percentage of selenium decreases as the selenization temperature is increased from 450 °C to 600 °C, suggesting that the selenium pellets may sublime too fast to form crystalline ZnSe in the structure of the ZIF-derived material. **Figure 3-6d** shows *J-V* curves of the DSSCs with the CEs of ZIF-ZnSe-NC prepared under different selenization temperatures. The pertinent photovoltaic parameters with standard deviations are also listed in **Table 3-3**. After optimizing the selenization temperatures of ZIF-NC, the cell with ZIF-ZnSe-NC-450 °C composite film exhibits the best η of $7.11 \pm 0.04\%$ with a V_{OC} of 0.76 ± 0.00 V, a J_{SC} of 13.60 ± 0.19 mA cm⁻², and a *FF* of 0.69 ± 0.01 , corresponding to the presence of the highest amount of ZnSe (22.55 wt%). With the increase of the selenization temperature from 450 °C up to 600 °C, the DSSC performance decreased due to the less weight percentage of ZnSe in ZIF-ZnSe-NC for forming the electrocatalytic active sites.

Overall, selenization temperature of 450 °C was selected as the best condition for selenizing the ZIF-NC.

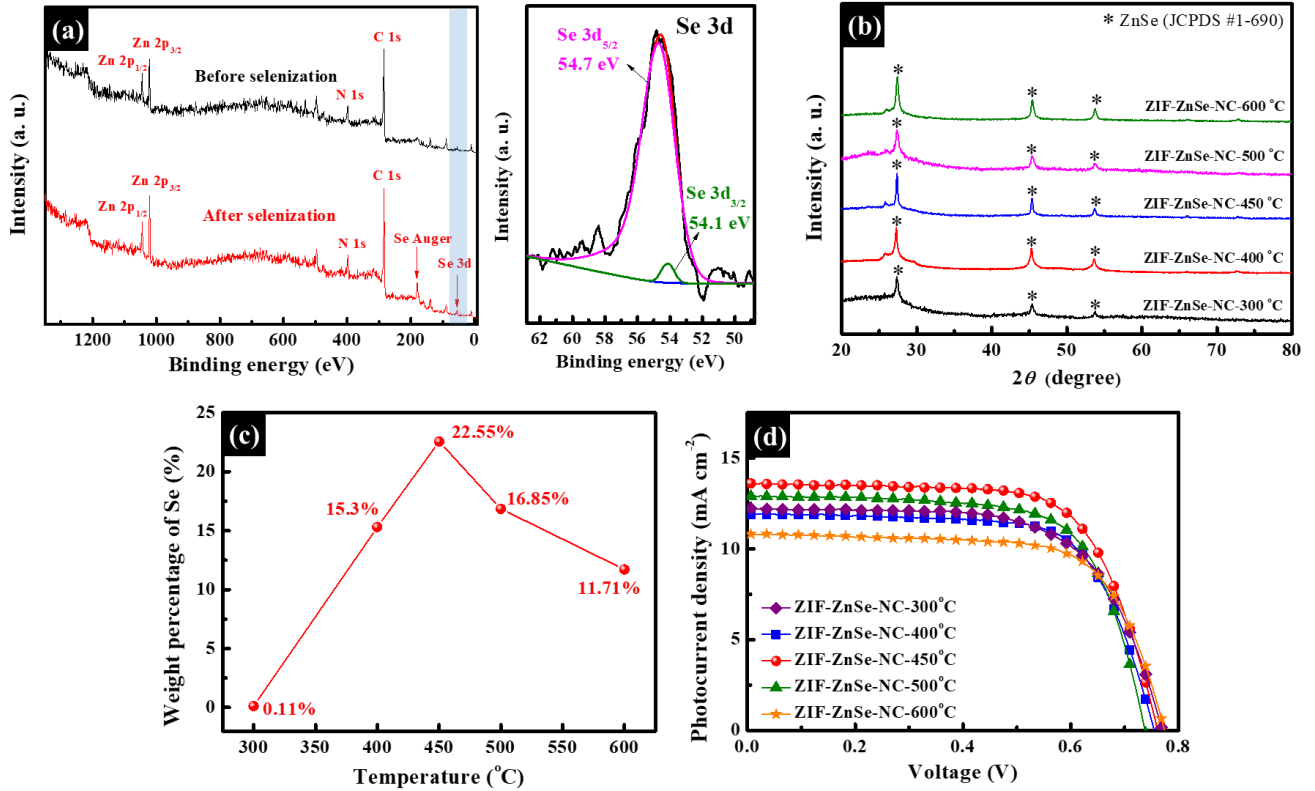


Figure 3-6 (a) XPS survey scan of ZIF-NC before and after selenization at 450 °C, and XPS of ZIF-NC after selenization for Se 3d spectra; (b) XRD patterns and (c) EDS analysis on the weight percentage of ZIF-ZnSe-NC with different selenization temperatures (300~600 °C); (d) *J-V* curves of the DSSCs with the CEs of ZIF-ZnSe-NC under different selenization temperatures (300~600 °C).

Table 3-3 The photovoltaic parameters of the DSSCs with ZIF-ZnSe-NC CEs prepared under different selenization temperatures, measured at 100 mW cm⁻². Average values and standard deviations were obtained from three independent cells.

Samples	η (%)	V_{oc} (V)	J_{sc} (mA cm ⁻²)	FF
ZIF-ZnSe-NC-300 °C	6.19 ± 0.05	0.77 ± 0.00	12.19 ± 0.30	0.66 ± 0.01
ZIF-ZnSe-NC-400 °C	6.21 ± 0.08	0.75 ± 0.00	11.93 ± 0.14	0.69 ± 0.00
ZIF-ZnSe-NC-450 °C	7.11 ± 0.04	0.76 ± 0.00	13.60 ± 0.19	0.69 ± 0.01
ZIF-ZnSe-NC-500 °C	6.51 ± 0.06	0.73 ± 0.00	12.66 ± 0.22	0.69 ± 0.01
ZIF-ZnSe-NC-600 °C	5.80 ± 0.07	0.77 ± 0.00	10.83 ± 0.20	0.69 ± 0.01

3-2-4 Electrochemical analyses of ZIF-7 and ZIF-derived materials

For making the main purpose of each process clearly, **Figure 3-1** shows the schematic process of ZIF-ZnSe-NC. First of all, the precursor of ZIF-7 was subject to carbonization to form ZIF-7 derived N-doped carbon cube (ZIF-NC); carbonization could enhance the electrical conductivity while the graphitic N and pyridinic N would form electroactive sites for promoting the I₃⁻ reduction reaction. Secondly, ZIF-NC was subject to selenization to form ZIF-7 derived ZnSe modified N-doped carbon cube (ZIF-ZnSe-NC); selenization could improve the electrocatalytic ability of the materials as both N-doped carbon materials and ZnSe could facilitate the reduction of I₃⁻. **Figure 3-7a** shows *J-V* curves of the DSSCs with the CEs of ZIF-7, ZIF-NC, and ZIF-ZnSe-NC. The pertinent photovoltaic parameters with standard deviations are listed in **Table 3-4**, in which the cell with ZIF-ZnSe-NC composite film exhibits the best DSSC performance among the CEs due to its enhanced electrocatalytic ability. To better understand the intrinsic parameters of each electrocatalyst sample, rotating disk electrode (RDE) analysis was applied to determine the two important indexes, namely, the intrinsic heterogeneous rate constant (k^0) and the effective electrocatalytic surface area (A_e). These properties largely influence the overall electrocatalytic activity of an electrode. At the formal potential

(E^0) of the I^-/I_3^- , various values of reciprocal current (i^{-1}) can be obtained from the linear sweep voltammetry (LSV) curves for a specific electrode at various rotating speeds (50, 100, 200, 400, 600, 800, and 1000 rpm). Thus, plots of reciprocal current (i^{-1}) vs. reciprocal of square root of rotating speed ($\omega^{-0.5}$) were obtained for ZIF-7, ZIF-NC, and ZIF-ZnSe-NC composite electrodes, as shown in **Figure 3-7b**. The intercept and slope of a fitting line in **Figure 3-7b** are respectively used to find k^0 and A_e values, by the following simplified Koutecký-Levich (K-L) **Equation 3-1**,⁶²

$$\frac{1}{i} = \frac{1}{nFA_e k^0 C} + \frac{1}{0.62nFA_e D^{2/3} \nu^{-1/6} \omega^{1/2} C} \quad (3-1)$$

where i is the disk current obtained at the formal potential (E^0) of I^-/I_3^- , n is the number of electrons transferred for I_3^- reduction, F is the Faraday constant, C is the bulk concentration of I_3^- (1.0 mM), D is the diffusion coefficient of I_3^- ($3.62 \times 10^{-6} \text{ cm}^2 \text{ s}^{-1}$), ν is the kinematic viscosity of ACN, and ω is the angular velocity converted from the rotating speed. Comparing to the pristine ZIF-7 ($k^0 = 9.4 \times 10^{-4} \text{ cm s}^{-1}$), the value of k^0 increases gradually while ZIF-7 was carbonized ($k^0 = 1.30 \times 10^{-3} \text{ cm s}^{-1}$) and further selenized ($k^0 = 3.42 \times 10^{-3} \text{ cm s}^{-1}$), indicating that both carbonization and selenization processes can enhance the electrocatalytic ability of ZIF-7 derived materials. On the other hand, the value of A_e for ZIF-7 ($A_e = 0.41 \text{ cm}^2$) slightly decreases under carbonization ($A_e = 0.36 \text{ cm}^2$) but increases dramatically upon further selenization ($A_e = 0.81 \text{ cm}^2$), suggesting that the polyhedra structure of ZIF-7 may shrink after annealing due to the decomposition of organic linkers at high carbonization temperature, while additional electroactive site of ZnSe was created *via* selenization, thus for increasing the A_e for catalyzing the I_3^- reduction. As summarized in **Table 3-4**, the ZIF-ZnSe-NC film shows the high k^0 value of $3.42 \times 10^{-3} \text{ cm s}^{-1}$ and a high A_e value of 0.805 cm^2 ; this reveals that the ZIF-ZnSe-NC film possesses excellent intrinsic electrocatalytic activity and high sufficient surface area for facilitating the reduction of I_3^- .

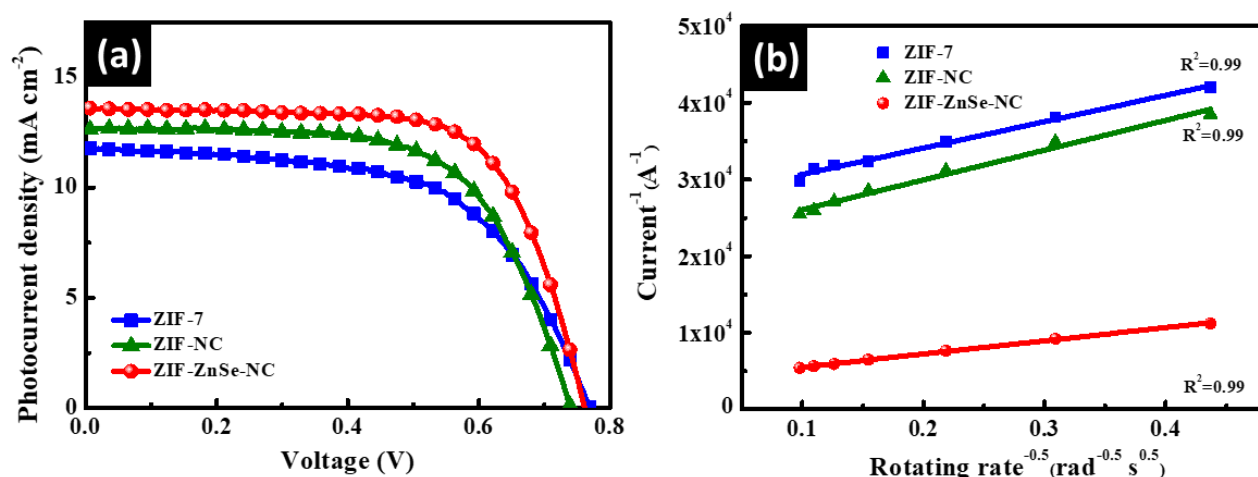


Figure 3-7 (a) J - V curves of the DSSCs with the CEs of ZIF-7, ZIF-NC, and ZIF-ZnSe-NC; (b) K-L plots for ZIF-7, ZIF-NC, and ZIF-ZnSe-NC composite electrodes.

Table 3-4 The photovoltaic parameters of the DSSCs with various CEs of ZIF-7, ZIF-NC, and ZIF-ZnSe-NC, measured at 100 mW cm^{-2} . Average values and standard deviations were obtained from three independent cells.

Samples	η (%)	V_{oc} (V)	J_{sc} (mA cm^{-2})	FF	k^0 (cm s^{-1})	A_e (cm^2)
ZIF-7	5.27 ± 0.08	0.77 ± 0.00	11.81 ± 0.36	0.58 ± 0.01	9.40×10^{-4}	0.41
ZIF-NC	6.02 ± 0.03	0.74 ± 0.00	12.27 ± 0.29	0.66 ± 0.01	1.30×10^{-3}	0.36
ZIF-ZnSe-NC	7.11 ± 0.04	0.76 ± 0.00	13.60 ± 0.19	0.69 ± 0.01	3.42×10^{-3}	0.81

3-2-5 Optimization of the ZIF-ZnSe-NC weight percentage for highly efficient counter electrode

To optimize the weight percentage of ZIF-ZnSe-NC for preparing the highly efficient CE in DSSCs, ZIF-ZnSe-NC films with various weight percentages in the PEDOT:PSS matrix were studied in the following. In this work, PEDOT:PSS not only served as the linker to enhance the connection of each ZIF-ZnSe-NC, but also acted as the binder to enhance the adhesion between the corresponding film and the conductive substrate¹²³ and among the ZIF-ZnSe-NC particles. In **Figure 3-8a**, FE-SEM images of the ZIF-ZnSe-NC films with different weight percentages of ZIF-ZnSe-NC (5~13 wt%) reveal that PEDOT:PSS is uniformly covered on ZIF-ZnSe-NC particles, suggesting that it is beneficial for the charge transfer. In all of the composite films, it was found that the ZIF-ZnSe-NC particles were well connected with each other by PEDOT:PSS conductive polymer. The SEM images of the ZIF-ZnSe-NC films (5~9 wt%) show that lower weight percentage of ZIF-ZnSe-NC films having abundant PEDOT:PSS covered on the surface of ZIF-ZnSe-NC particles; this suggests that the active site on the ZIF-ZnSe-NC particles may be blocked. For the case with high loading of ZIF-ZnSe-NC particles (13 wt%), PEDOT:PSS may not only provide sufficient connection among ZIF-ZnSe-NC particles. In addition, it may suffer from the poor adhesion between the composite film and the substrate. To compare the performance of ZIF-ZnSe-NC films with various weight percentages, **Figure 3-8b** shows $J-V$ curves of the DSSCs with the corresponding CE films. The corresponding photovoltaic parameters with standard deviation data are summarized in **Table 3-5**. After optimizing the weight percentage concentration of ZIF-ZnSe-NC, the cell with ZIF-ZnSe-NC-11 wt% composite film exhibits an attractive photovoltaic conversion efficiency of $8.69\pm 0.13\%$, as shown in **Figure 3-8c**. Although the DSSC with a CE of ZIF-ZnSe-NC-13 wt% composite film, having a relatively higher amount of electrocatalytic active site and showing higher J_{SC} value of $16.78\pm 0.09 \text{ mA cm}^{-2}$, lower V_{OC} ($0.75\pm 0.00 \text{ V}$) and lower FF (0.63 ± 0.01), its cell efficiency ($7.91\pm 0.05\%$) is limited by the insufficient coverage of PEDOT:PSS¹¹⁶. It's concluded that a CE film of ZIF-ZnSe-NC-11 wt% gives the best performance, and simultaneously provides both proper charge transfer route and good electrocatalytic ability. The EDS spectrum indicates the existence of C, N, Zn, Se, and S in the ZIF-ZnSe-NC-11 wt% film (**Figure 3-9a**). Besides, the EDS elemental mapping images of ZIF-ZnSe-NC-

11 wt% film (**Figure 3-9b**) show homogeneous distribution of C, N, Zn, and Se in the ZIF-ZnSe-NC particles. The element S, which is derived from PEDOT:PSS, is well-dispersed in the ZIF-ZnSe-NC-11 wt% film.

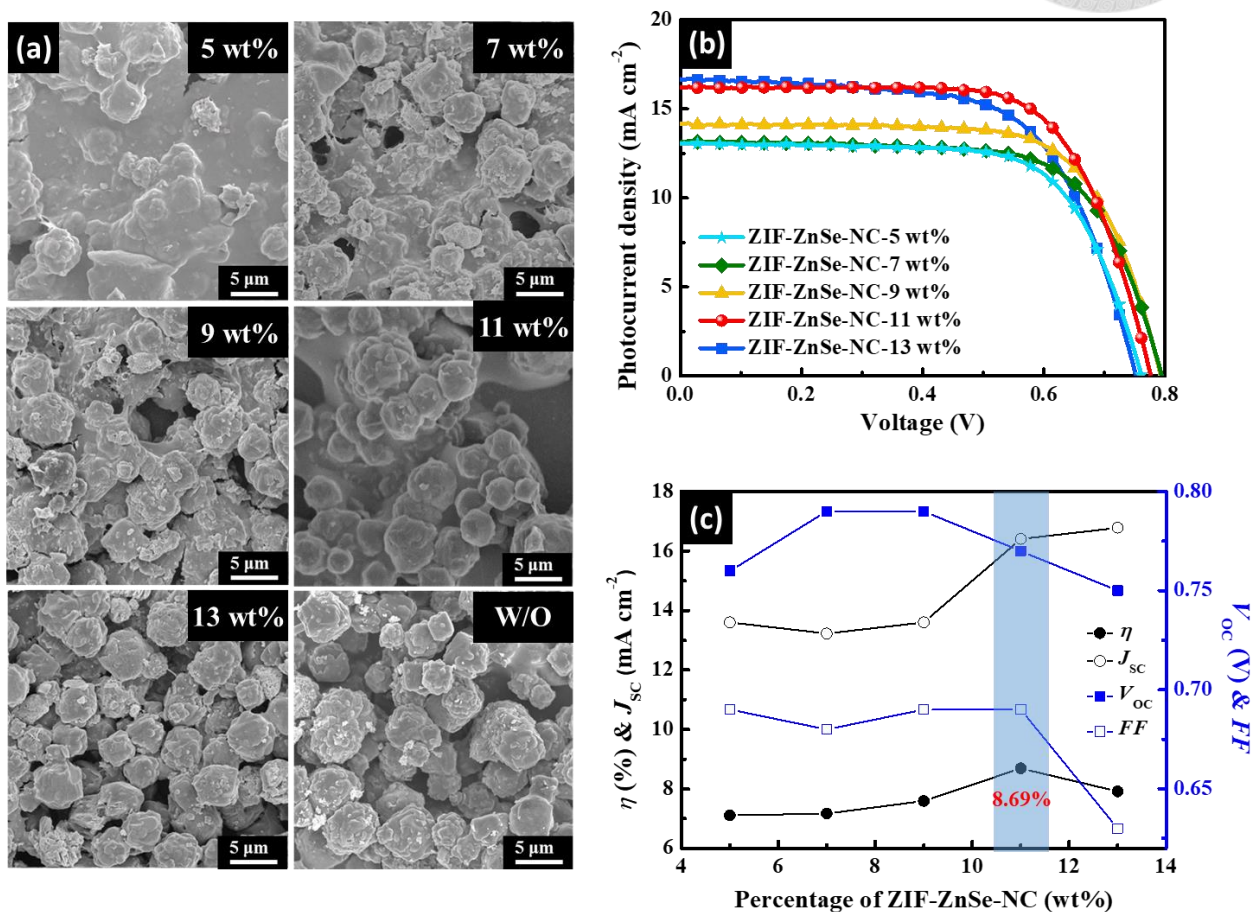


Figure 3-8 (a) FE-SEM images of the ZIF-ZnSe-NC films with different weight percentages of ZIF-ZnSe-NC (5~13 wt%) and pristine ZIF-ZnSe-NC film (W/O: without PEDOT:PSS); (b) *J*-*V* curves and (c) Photovoltaic parameters of the DSSCs with the CEs of ZIF-ZnSe-NC films with different weight percentages (5~13 wt%).

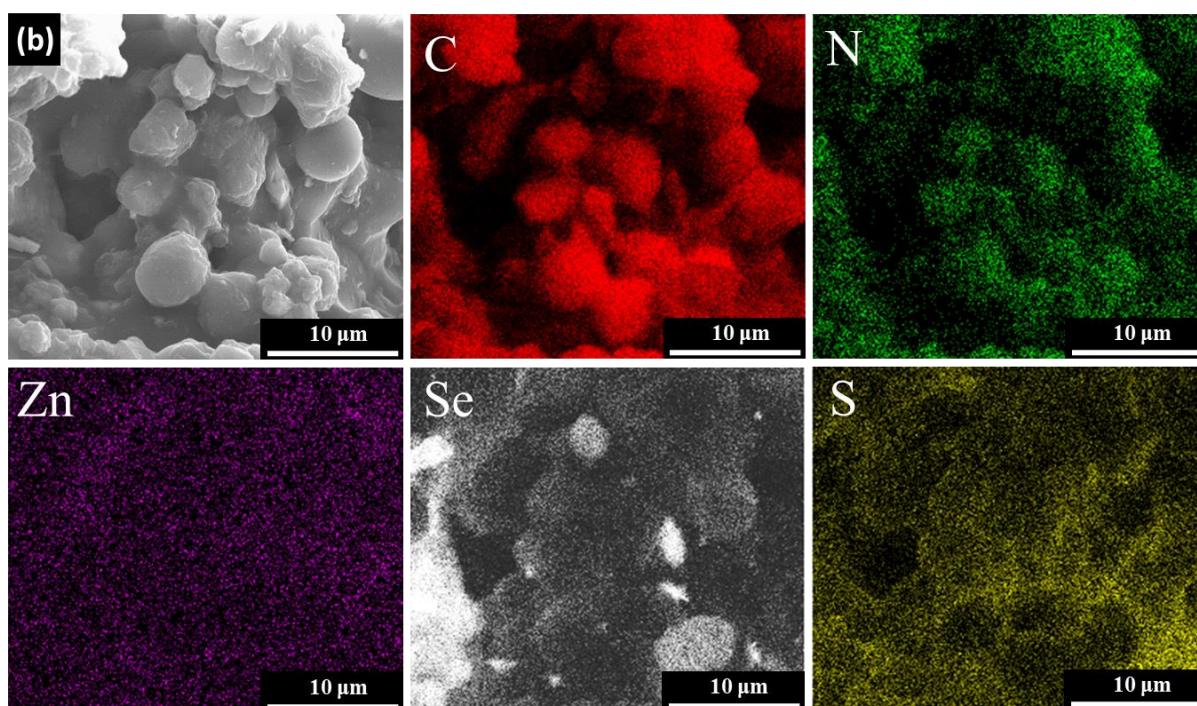
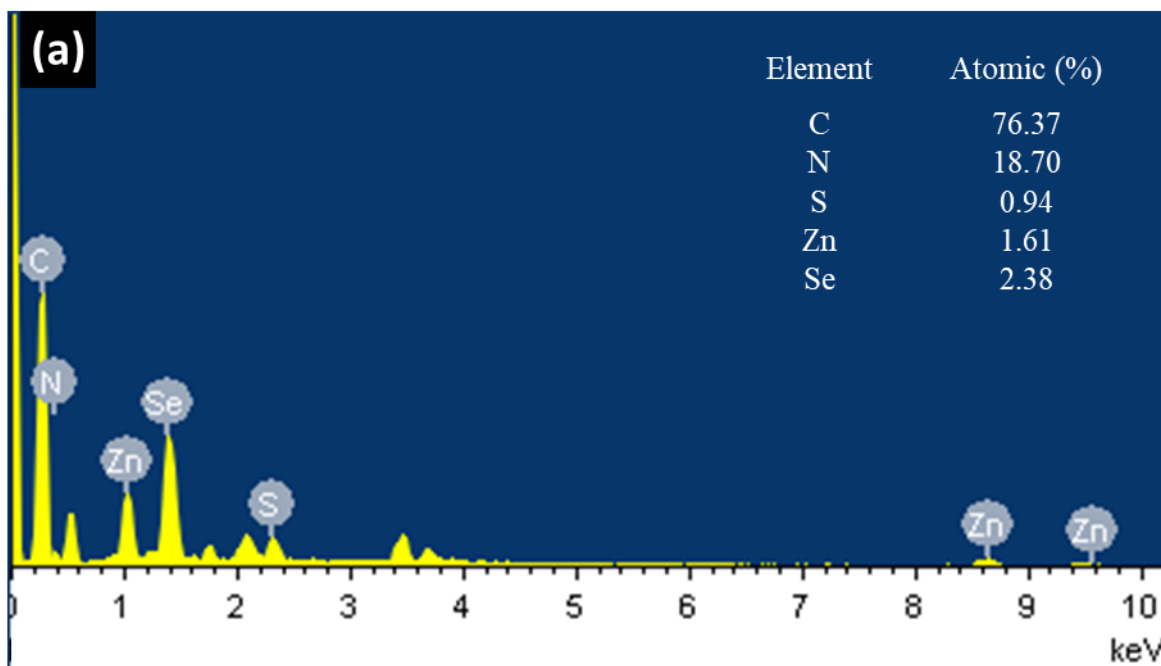


Figure 3-9 (a) EDS spectrum, and (b) the corresponding EDS elemental mapping images of ZIF-ZnSe-NC-11 wt% film.

Table 3-5 The photovoltaic parameters of the DSSCs with ZIF-ZnSe-NC CEs under different slurry concentrations (5~13 wt%), measured at 100 mW cm⁻². Average values and standard deviations were obtained from three independent cells.

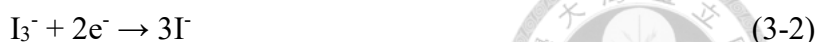
Samples	η (%)	V_{oc} (V)	J_{sc} (mA cm ⁻²)	FF
ZIF-ZnSe-NC-5 wt%	7.11 ± 0.04	0.76 ± 0.00	13.60 ± 0.19	0.69 ± 0.01
ZIF-ZnSe-NC-7 wt%	7.17 ± 0.07	0.79 ± 0.00	13.22 ± 0.25	0.68 ± 0.01
ZIF-ZnSe-NC-9 wt%	7.59 ± 0.17	0.79 ± 0.00	13.60 ± 0.45	0.69 ± 0.00
ZIF-ZnSe-NC-11 wt%	8.69 ± 0.13	0.77 ± 0.00	16.40 ± 0.45	0.69 ± 0.01
ZIF-ZnSe-NC-13 wt%	7.91 ± 0.05	0.75 ± 0.00	16.78 ± 0.09	0.63 ± 0.01

3-2-6 Comparison of DSSC with CE of commercial Pt and optimized ZIF-ZnSe-NC

Figure 3-10a shows the J - V curves of the DSSCs with the CEs of ZIF-ZnSe-NC-11 wt% and Pt; the inset spectra is the incident photon-to-current conversion efficiency (IPCE), which is defined as the ratio of the electrons produced by the external circuit to the incident photons at the wavelength of 400~800 nm under a short-circuit condition. The corresponding photovoltaic parameters with standard deviation data are summarized in **Table 3-6**. The cell with ZIF-ZnSe-NC-11 wt% composite CE film exhibits the best η of 8.69 ± 0.13%, which is higher than that of the cell with a Pt CE (8.26±0.02%). The theoretical short-circuit current density ($J_{SC-IPCE}$) values of the cell calculated based on the IPCE with ZIF-ZnSe-NC-11 wt% (13.34 mA cm⁻²) is higher than that of the cell with a Pt CE (12.40 mA cm⁻²). This is because the pristine ZIF-ZnSe-NC particle provides a larger electrocatalytic surface area for its composite film for I₃⁻ reduction, and thereby, enables a higher electrocatalytic activity for its CE.

Cyclic voltammetry (CV) was applied to explore the redox kinetics of I/I₃⁻ at the surfaces of different electrocatalytic films, and the electrocatalytic film of a CE facilitates the reduction of I₃⁻ at

its surface with the electrolyte, as shown in **Equation 3-2**⁸²



The CV curves of ZIF-ZnSe-NC-11 wt% and Pt CEs are shown in **Figure 3-10b**. The net peak current density from the cathodic current peak to the background curve is defined as the cathodic peak current density (J_{pc}). The J_{pc} value of ZIF-ZnSe-NC-11 wt% ($J_{pc} = 0.91 \text{ mA cm}^{-2}$) is higher than that of Pt ($J_{pc} = 0.85 \text{ mA cm}^{-2}$), once again confirmed its overall electrocatalytic ability for I_3^- reduction. As shown in the K-L plot (**Figure 3-10c**), the Pt film shows a higher k^0 value ($5.57 \times 10^{-3} \text{ cm s}^{-1}$) and a lower A_e value (0.11 cm^2) (**Table 3-7**); this reveals that the flat Pt film possesses an excellent intrinsic electrocatalytic activity with a limited active surface area. The ZIF-ZnSe-NC-11 wt% film offers a much larger value of A_e (0.81 cm^2) despite its slightly lower value of k^0 ($3.42 \times 10^{-3} \text{ cm s}^{-1}$); Overall, the ZIF-ZnSe-NC-11 wt% CE film still possesses good intrinsic electrocatalytic activity and high surface area for facilitating the reduction of I_3^- .

To investigate the charge transfer properties at the CE/electrolyte interface, Tafel polarization curves and electrochemical impedance spectra (EIS) analyses were conducted in the same electrolyte using symmetric cells composed of the same film on both anode and cathode, individually consisted of ZIF-ZnSe-NC-11 wt% and Pt films. **Figure 3-10d** represented the EIS spectra of such symmetric cells with ZIF-ZnSe-NC-11 wt% and Pt. Based on the equivalent circuit shown in the inset of **Figure 3-10d**, the series resistance (R_s) and charge transfer resistance (R_{ct}) were obtained; these were evaluated from the onset point and the radius of the first semicircle, respectively. A lower R_s reflects a better ohmic contact between the substrate and the electrocatalytic film; a smaller R_{ct} value refers to a more substantial amount of electrons transferring through the CE/electrolyte interface, and thereby indicating a faster electron transfer capability of the film. As summarized in **Table 3-7**, the R_s values and the R_{ct} values show a tendency of ZIF-ZnSe-NC-11 wt% < Pt. The Tafel polarization curves of ZIF-ZnSe-NC-11 wt% and Pt are shown in the inset of **Figure 3-10d**. The value of the exchange current density (J_0) of a film is read from the intercept (at $V = 0$) of the extrapolating lines of both anodic and cathodic curves in the Tafel zone ($120 \text{ mV} < |V| < 400 \text{ mV}$).⁶³ A higher value of J_0 represents a better electrocatalytic ability of a film; the values of J_0 show a tendency of ZIF-ZnSe-

NC-11 wt% > Pt, which is in good agreement with the trend of J_{pc} . The electrocatalytic ability of an electrode is validated not only by CV and RDE analyses, but also by Tafel and EIS analyses. After the above analyses, we conclude that ZIF-ZnSe-NC-11 wt% exhibits the best electrocatalytic ability for I_3^- reduction, thus offering a high potential for replacing the expensive Pt in a DSSC.

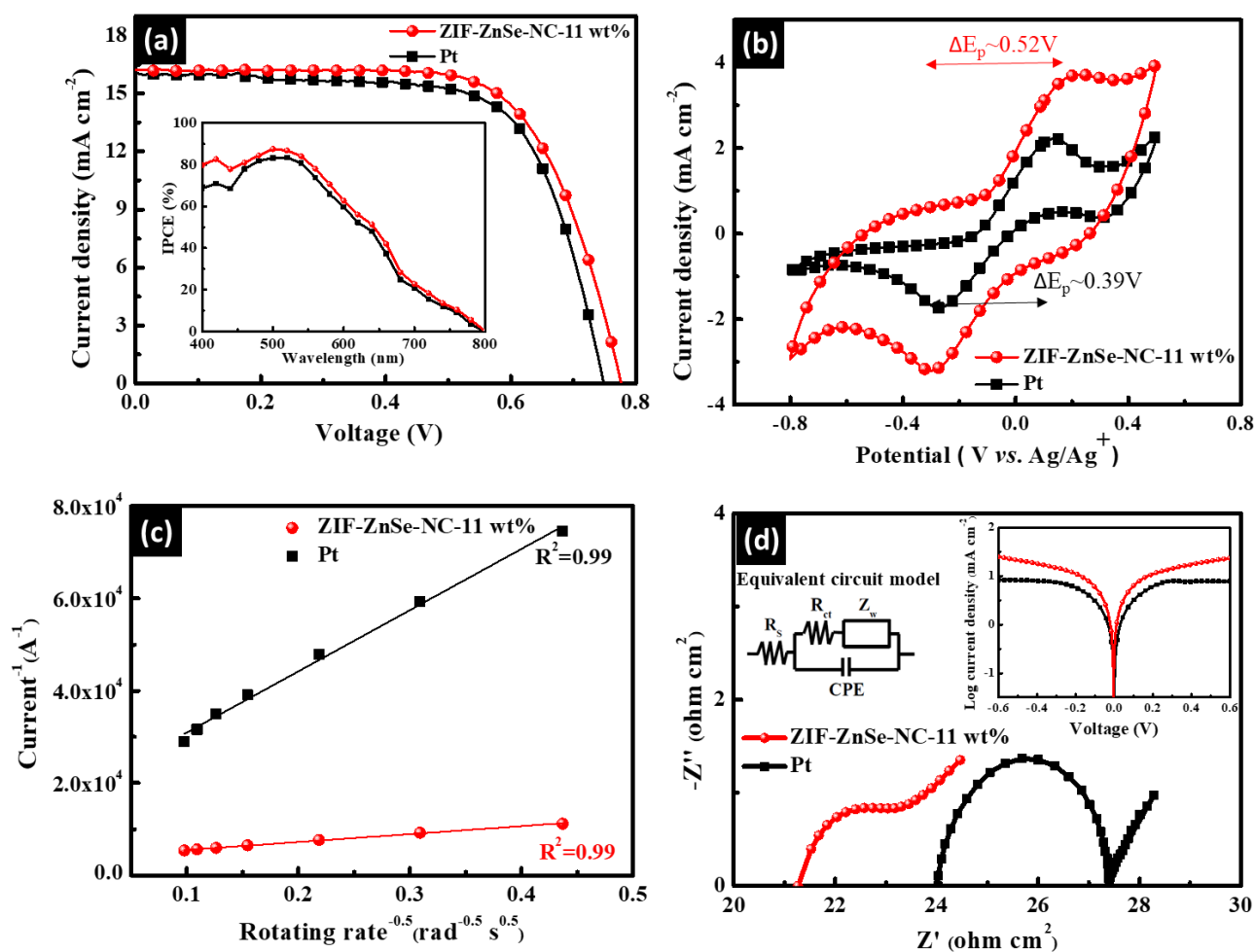


Figure 3-10 (a) J - V curves of the DSSCs with the CEs of ZIF-ZnSe-NC-11 wt% and Pt (inset: IPCE curves of the corresponding devices); (b) CV curves, (c) K-L plots, and (d) EIS spectra (inset: Tafel polarization plots) of the electrodes with ZIF-ZnSe-NC-11 wt% and Pt.

Table 3-6 The photovoltaic parameters of the DSSCs with CEs of ZIF-ZnSe-NC-11 wt% and Pt, measured at 100 mW cm⁻². Average values and standard deviations were obtained from three independent cells.

Samples	η (%)	V_{oc} (V)	J_{sc} (mA cm ⁻²)	FF	$J_{SC-IPCE}$ (mA cm ⁻²)
ZIF-ZnSe-NC-11 wt%	8.69 ± 0.13	0.77 ± 0.00	16.40 ± 0.45	0.69 ± 0.01	13.34
Pt	8.26 ± 0.02	0.75 ± 0.00	16.05 ± 0.03	0.69 ± 0.00	12.40

Table 3-7 The electrochemical parameters *via* CV and RDE; charge transfer parameters *via* EIS and Tafel for the electrocatalytic films of ZIF-ZnSe-NC-11 wt% and Pt.

Samples	J_{pc} (mA cm ⁻²)	k^0 (cm s ⁻¹)	A_e (cm ²)	R_s (Ω cm ²)	R_{ct} (Ω cm ²)	J_0 (mA cm ⁻²)
ZIF-ZnSe-NC-11 wt%	0.91	3.42×10 ⁻³	0.81	21.27	1.26	3.63
Pt	0.85	5.57×10 ⁻³	0.11	24.03	1.71	3.28

Furthermore, it was also worth to mention that DSSC still exhibited good conversion efficiency in the dim light condition.⁷² The J - V curves of the DSSCs based on the CEs of ZIF-ZnSe-NC-11 wt% and Pt were obtained at various light intensities in the range of 10-100 mW cm⁻², as shown in **Figure 3-11**. The corresponding photovoltaic parameters with standard deviation data are summarized in **Table 3-8**. The DSSCs with CEs of ZIF-ZnSe-NC-11 wt% were illuminated at the dim light condition of 50 mW cm⁻², the efficiency ($\eta = 8.02 \pm 0.01\%$) did not decay too much and almost maintain 92% of the efficiency under 1 sun condition of 100 mW cm⁻² ($\eta = 8.69 \pm 0.13\%$). Even in the case of 10 mW cm⁻² illumination, a reasonable efficiency of $7.99 \pm 0.01\%$ was still obtained for the DSSCs with

CEs of ZIF-ZnSe-NC-11 wt%. In contrast, the η of the DSSCs with CEs of Pt went from 8.26 ± 0.02 , 7.87 ± 0.05 , to $7.41 \pm 0.02\%$ under illuminations at 100, 50, and 10 mW cm^{-2} , respectively.

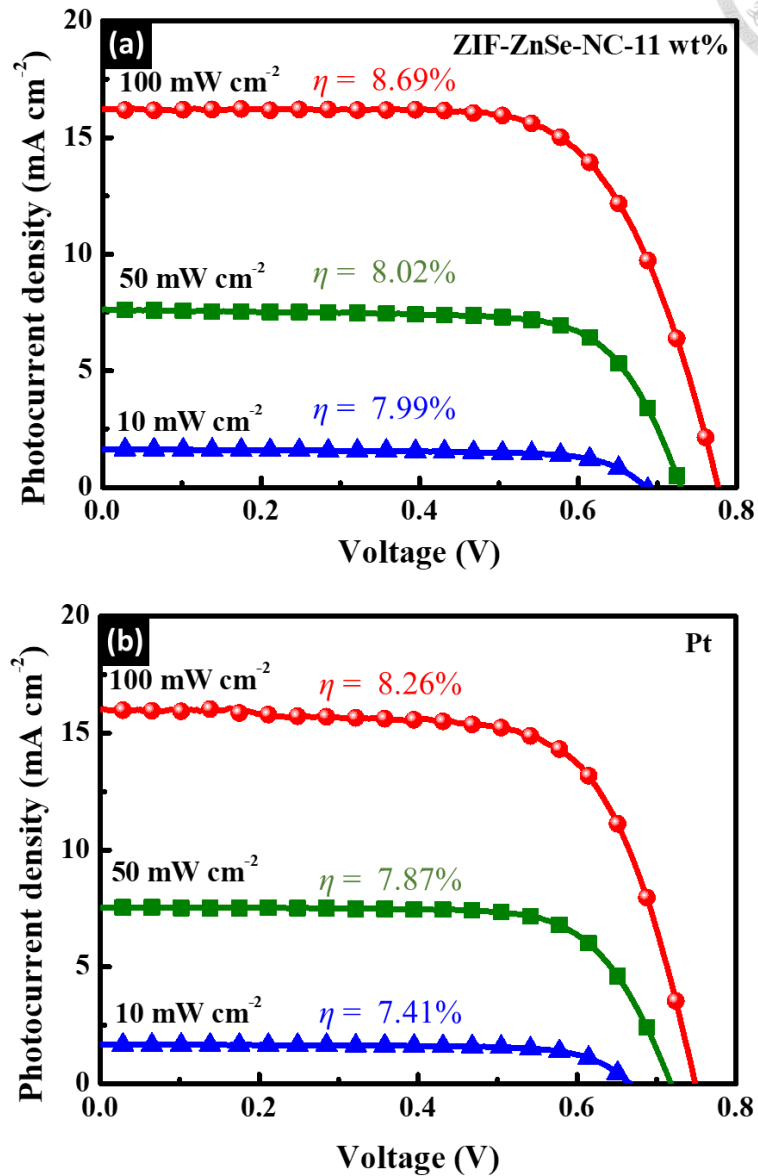


Figure 3-11 *J-V* curves of the DSSCs with the CEs of (a) ZIF-ZnSe-NC-11 wt% and (b) Pt under different incident light intensities (10~100 mW cm^{-2}).

Table 3-8 The photovoltaic parameters of the DSSCs with the CEs of ZIF-ZnSe-NC-11 wt% and Pt, measured under 10-100 mW cm⁻². Average values and standard deviations were obtained from three independent cells.

Light intensity (mW cm ⁻²)	ZIF-ZnSe-NC-11 wt%			
	η (%)	V _{OC} (V)	J _{SC} (mA cm ⁻²)	FF
100 (1 sun)	8.69 ± 0.13	0.77 ± 0.00	16.40 ± 0.45	0.69 ± 0.01
50 (0.5 sun)	8.02 ± 0.01	0.73 ± 0.00	7.60 ± 0.05	0.72 ± 0.00
10 (0.1 sun)	7.99 ± 0.01	0.68 ± 0.00	1.63 ± 0.01	0.72 ± 0.00
Light intensity (mW cm ⁻²)	Pt			
	η (%)	V _{OC} (V)	J _{SC} (mA cm ⁻²)	FF
100 (1 sun)	8.26 ± 0.02	0.75 ± 0.00	16.05 ± 0.03	0.69 ± 0.00
50 (0.5 sun)	7.87 ± 0.05	0.72 ± 0.00	7.56 ± 0.03	0.73 ± 0.00
10 (0.1 sun)	7.41 ± 0.02	0.66 ± 0.00	1.67 ± 0.00	0.73 ± 0.00

3-3 Conclusions

In this work, zinc selenide decorated N-doped carbonaceous hybrid material (ZIF-ZnSe-NC) derived from zeolitic imidazolate framework (ZIF-7) was successfully synthesized and firstly introduced as the electrocatalyst for the CE in DSSCs. ZIF-7 powder was subject to carbonization to form ZIF-7 derived N-doped carbon cube (ZIF-NC), followed by further selenization to transform into ZIF-7 derived ZnSe/N-doped carbon cube (ZIF-ZnSe-NC). Raman, four-point probe analyses, and SEM images showed that with the higher carbonization temperature, the electrical conductivity of the materials would increase, while the morphology of ZIF-NC may collapse. XRD and XPS analyses revealed that the annealed ZIF-ZnSe-NC composite material is composed of crystalline ZnSe and N-doped amorphous carbon. The better electrocatalytic ability of ZIF-ZnSe-NC-11 wt% film, as compared to that of Pt, is validated by CV, RDE, Tafel and EIS analyses. The DSSCs with ZIF-ZnSe-NC-11 wt% CEs rendered a photovoltaic conversion efficiency (η) of $8.69 \pm 0.13\%$, which is higher than that of the cells with Pt CEs ($8.26 \pm 0.02\%$). A reasonable cell efficiency of $7.99 \pm 0.01\%$ was still attained for the DSSCs with CEs of ZIF-ZnSe-NC-11 wt% under dim light intensities of 10 mW cm^{-2} . Thus, it could be concluded that the ZIF-ZnSe-NC is a promising material to replace the expensive Pt in DSSCs, especially for the indoor application. In fact, the key concept of this work is to propose a new strategy for the application of ZIFs as precursors in the field of photovoltaic devices. Based on the results obtained from this work, more attractive materials can be synthesized through different chemical modifications (including nitridation, sulfuration, *etc.*) using a variety of MOF-derived precursors. Therefore, more eco-friendly materials for the use in DSSCs with high photovoltaic performance can be expected in the future.

Chapter 4

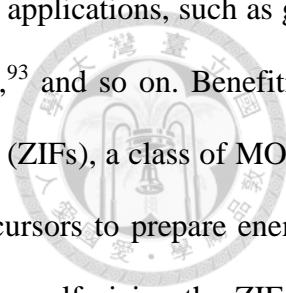
Designing a carbon nanotube interconnected ZIF-derived cobalt sulfide hybrid nanocage for supercapacitors



4-1 Introduction and motivation

Nowadays, as the energy consumption and the depletion of fossil fuel accelerating, the environment urgently calls for a new energy system to meet the current demands.^{40, 44, 124} Among several kinds of energy storage devices, electrochemical supercapacitors (SCs) have received the remarkable attention due to their worth mentioning properties of high power density, rapid charge-discharge rates and long cycle life.^{125, 126} Depending on their charge storage mechanism, SCs can be classified into two categories: electric double-layer capacitors (EDLCs) and pseudocapacitors. EDLCs, of which the capacitance arise from the charge separation at its electrode/electrolyte interface using mainly carbon materials, show the advantages of promising electric conductivity and high cycling stability.¹²⁷ However, the low specific capacitance of EDLCs limits their applicability for integrating into high-capacitance required electronic devices. On the other hand, pseudocapacitors offer a superior specific capacitance due to the fast and reversible faradaic redox reactions between the electrolyte and the redox-active electrode materials, such as transition metal oxides,^{51, 52} metal hydroxides,⁵³ and conducting polymers.⁵⁴ Recently, transition metal sulfides, *i.e.* cobalt sulfide, molybdenum disulfide, nickel sulfide and so on, have received widespread attention as appealing electrode materials for SCs in view of their outstanding electrochemical properties.⁵⁵⁻⁵⁹ Among the reported materials of metal sulfides, cobalt sulfide has emerged as a promising electrode material for SCs due to its higher mechanical, thermal stability and richer redox reactions with various crystalline phases compared with its cobalt oxide or hydroxide counterparts.^{57, 60} Nevertheless, just like most pseudocapacitive materials which badly suffered from poor rate capability, mechanical instability, and low electric conductivity, the progress of CoS-based pseudocapacitors is also limited by these drawbacks for practical applications.

Recently, metal-organic frameworks (MOFs), which consist of metallic clusters as the nodes



and organic ligands as the linkers, have been widely explored for versatile applications, such as gas absorption,^{83, 84} gas separation,^{86, 87} sensors,⁹¹ catalysis,⁸⁹ supercapacitors,⁹³ and so on. Benefiting from highly porous and robust structures, zeolitic imidazolate frameworks (ZIFs), a class of MOFs, have recently been proposed to be appealing sacrificial templates or precursors to prepare energy materials. For instance, Jiang *et al.* synthesized hollow CoS nanocages by sulfurizing the ZIF-67 template with thioacetamide, which exhibited a high specific capacitance of 1475 F g⁻¹ at a current density of 1 A g⁻¹ when used as an electrode material for SCs.¹²⁸ Han *et al.* used a ZIF-67-derived porous cobalt sulfide nanosheet array as an electrode material of SCs for achieving a specific capacitance of 1098 F g⁻¹ at a current density of 0.5 A g⁻¹.⁵⁶ Yilmaz *et al.* prepared a NiCo-LDH/Co₉S₈ hybrid from a ZIF-67 template as the SCs electrode, showing excellent electrochemical performance and stability (1653 F g⁻¹ at 4 A g⁻¹; 95.4% after 3000 cycles).¹²⁹ For further enhancing the pseudocapacitive performance of SCs electrodes, electrode materials interconnected with carbon nanotubes (CNTs) have been proposed,^{130, 131} so as to include merits of excellent electric conductivity, electrochemical stability, and good mechanical strength. CNTs provides highly conductive pathways for electron transfer between the electrode material and the current collector to improve the overall electric conductivity. Furthermore, CNTs can not only play a role to induce more porosity for facilitating ion diffusion, but also to inhibit the aggregation of the composites.¹³ For example, P. Wu *et al.* prepared NiCo₂O₄@CNT electrode for SCs, achieving a specific capacitance of 1590 F g⁻¹ at 0.5 A g⁻¹.¹³² Z. Tang *et al.* reported a nano-architected Ni(OH)₂/CNT electrode with a high specific capacitance of 3300 F g⁻¹ at 2.5 mA cm⁻² prepared by a simple two-step fabrication method.¹³³ X. Wang *et al.* synthesized CNT/ternary oxide composite materials electrode for utilizing in SCs, showing a specific capacitance of 1642 F g⁻¹ at 0.5 A g⁻¹.¹³⁴

As inspired from previous reports, herein, a hybrid structure of CNT interconnected ZIF-67 derived cobalt sulfide (CNT/CoS) nanocage for proposed in the first time as the electrode material of SCs. As shown in **Figure 4-1**, the precursors of ZIF-67 were synthesized with functional CNT to form the carbon nanotubes/ZIF-67 polyhedra nanocomposites (CNT/ZIF-67). The particle size of ZIF-67 can be easily controlled by adjusting the mass ratio of CNT to ZIF precursor under crystalline

process. After further sulfurization by the reflux method, the hybrid structure of CNT/CoS nanocage with high electrical conductivity and high electrochemical performance were successfully synthesized, maintaining the polyhedral structure of ZIF-67 derived CoS with interconnected CNT chains as the conductive channels. The advantage of hybrid CNT/CoS nanocage is to overcome the low electrical conductivity of amorphous ZIF-67 derived CoS by providing the conductive chains of CNT, which serves as fast electron conducting channels. Meanwhile, electrolyte can also easily diffuse into the hollow structure of CoS nanocage to increase the charge transportation. After optimizing the particle size of CoS nanocage, the electrode with the CNT/CoS 1:2 hybrid nanocage exhibits an excellent specific capacitance of 2173.1 F g^{-1} at a current density of 5 A g^{-1} (pristine CoS: 986 F g^{-1}), and the capacitance retention is 91% over 1000 cycles, demonstrating a great potential for not only in energy applications but also in electrocatalytic reactions.

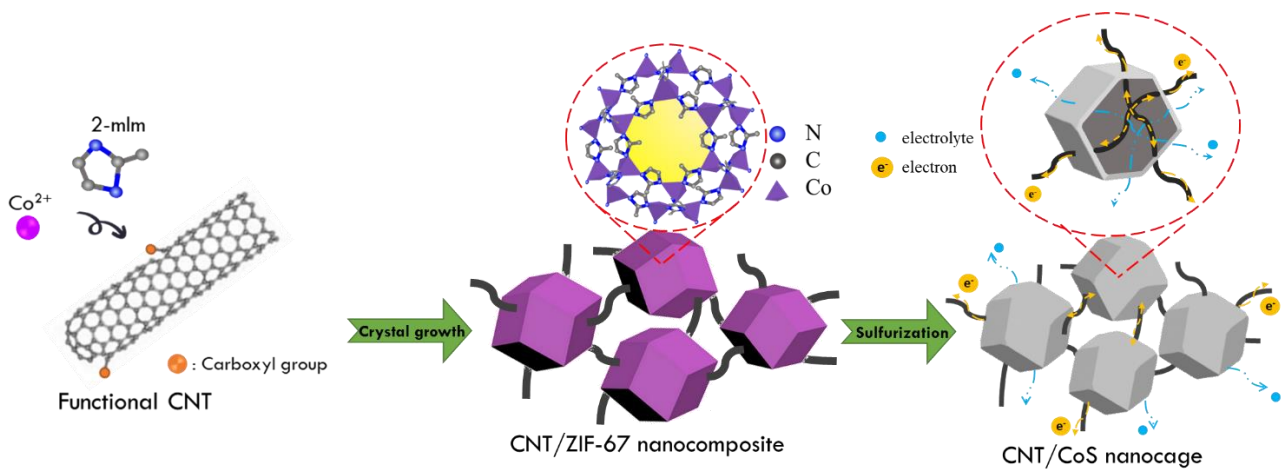


Figure 4-1 Schematic illustration of the synthesis of CNT/CoS nanocages.

4-2 Results and discussions

4-2-1 Characterization of the as-synthesized ZIF-67

ZIF-67 is composed of a cobalt cluster connected by a 2-methylimidazole (2-mlm) ligand in a sodalite (SOD) topology, as illustrated in **Figure 4-2a**. **Figure 4-2b** shows the SEM image of as-synthesized ZIF-67, revealing that the well-dispersed ZIF-67 crystals have a typical rhombic dodecahedral morphology and an average particle size around 500 nm. To further characterize the crystalline structure of as-synthesized ZIF-67, **Figure 4-2c** illustrates the XRD pattern of the as-synthesized ZIF-67; the characteristic diffraction peaks are highly consistent with the simulated XRD pattern of ZIF-67 crystal reported in the literature.⁶¹ Another index to confirm the microporous structure of as-synthesized ZIF-67 is surface area. The N₂ adsorption-desorption isotherm of ZIF-67 is shown in **Figure 4-2d**, showing the type I isotherm with sharply increased adsorption at low relative pressure, which is typical of microporous materials. The BET surface area of ZIF-67 is 1845.8 m² g⁻¹, which is superior to the values reported in the literatures.^{61, 135} Moreover, the pore size distribution was further evaluated by using the density functional theory (DFT) method. As shown in the inset of **Figure 2d**, the pore size distribution plot of ZIF-67 shows the peaks *ca.* 1.0 nm and 1.3 nm, revealing the presence of micropores.

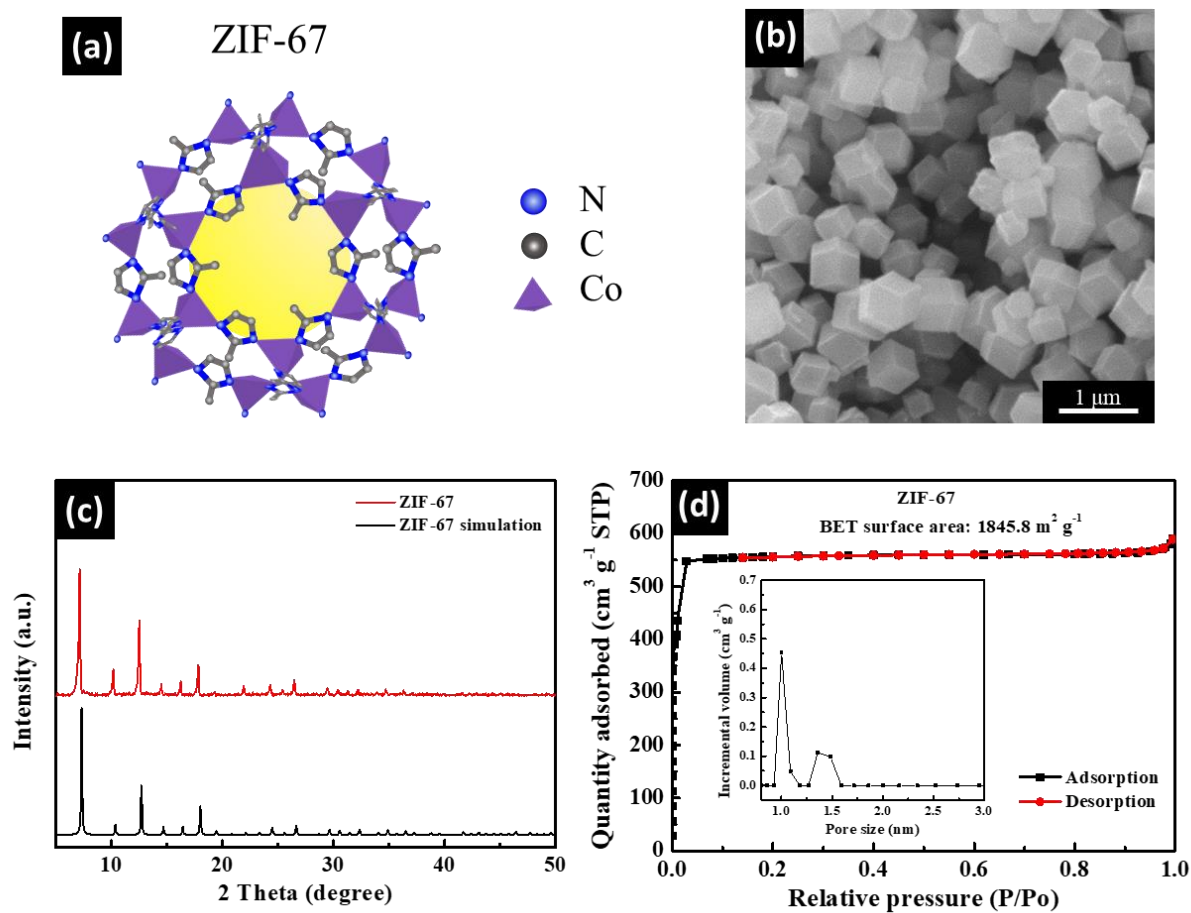


Figure 4-2 (a) Schematic illustration, (b) FE-SEM image, (c) XRD pattern, and (d) N_2 adsorption-desorption isotherms (inset: pore size distribution) of as-synthesized ZIF-67.

4-2-2 Characterization of CNT/ZIF-67 nanocomposites

Figure 4-3a shows the SEM images of functionalized CNT and as-synthesized CNT/ZIF-67 nanocomposites with various CNT/ZIF-67 mass ratios. The SEM images of functionalized CNT shows a dense network of CNTs with an average diameter around 20 nm. For the case of CNT/ZIF-67 nanocomposites with various mass ratios, CNT/ZIF-67 composites consist of uniform CNT-inserted polyhedral with average sizes of 180, 250, and 400 nm by varying the mass ratio of CNT/ZIF-67 of 1:1, 1:2, and 1:8, respectively. Possible formation mechanism of ZIF-67 growth on functional CNT surface with various mass ratio was schematically illustrated in **Figure 4-3b**. In the first step, the negatively carboxyl groups on functional CNT acted as nucleation sites so that metal ions could be attracted to the CNT, which may facilitate the formation of ZIF-67 by heterogeneous nucleation. At lower mass ratio of CNT/ZIF-67, most of the CNTs are embedded by ZIF-67 crystals and few of them can be found in SEM images, and the particle size of the corresponding nanocomposite is similar to that of the pristine ZIF-67. As the mass ratio of CNTs to ZIF-67 increases, the more nucleation sites on the surface of CNTs are available for the growth of ZIF-67, which would result in smaller particle size of ZIF-67 crystals.^{13, 101} The trend of ZIF-67 formation on the CNT surface with various mass ratios can be well elucidated by SEM images, as shown in **Figure 4-3a**. To understand the crystalline structure of CNT/ZIF-67 nanocomposites with various mass ratios, **Figure 4-3c** shows the XRD patterns of the CNT/ZIF nanocomposites. With the introduction of CNTs into ZIF-67, the obtained CNT/ZIF-67 nanocomposites exhibit similar diffraction peaks with ZIF-67. Another interesting trend of XRD pattern for CNT/ZIF-67 nanocomposites showed the intensities of the peaks ($2\theta = 7.5^\circ$) increase as the mass ratio of CNT to ZIF-67 decreases, once again confirming the highly crystallization to form larger particle sizes for the case of CNT/ZIF-67 1:8. Moreover, no obvious peaks of CNT can be observed; it may be ascribed to the low content of CNT in CNT/ZIF-67 nanocomposites.

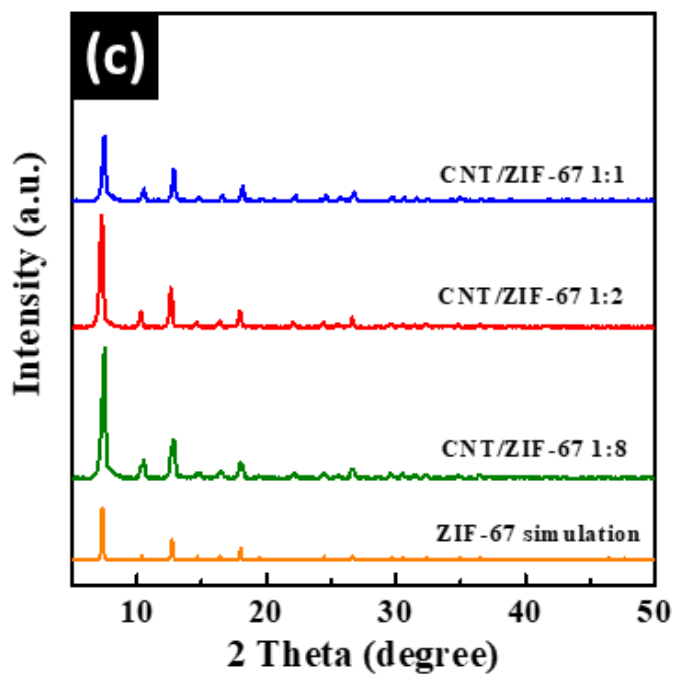
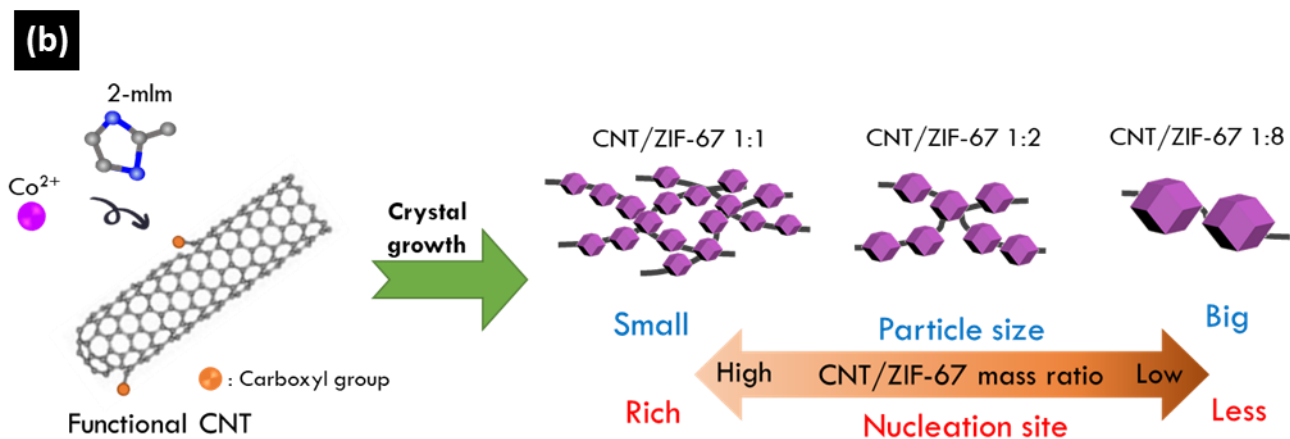
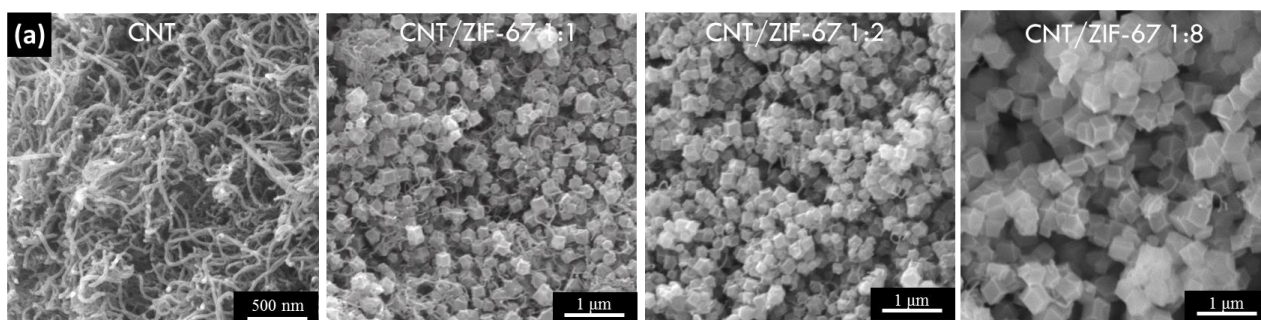


Figure 4-3 (a) FE-SEM image of CNT and CNT/ZIF-67 nanocomposites with different mass ratios of CNT to ZIF-67, (b) growth schematic and (c) XRD patterns of ZIF-67 crystal size with different ratio of CNT to ZIF-67.

4-2-3 Characterization of CoS nanocage and hybrid CNT/CoS nanocages

In the previous section, the particle sizes of ZIF-67 were successfully tailored by controlling the mass ratio of CNT to ZIF-67. Based on this result, the hybrid CNT/CoS nanocage with desirable particles size can be synthesized after simple sulfurization and then further applied for SCs. **Figure 4-4a** shows the SEM images of as-synthesized CoS nanocage and hybrid CNT/CoS nanocages with various sizes of ZIF-67 as templates, namely CNT/CoS 1:1, CNT/CoS 1:2, and CNT/CoS 1:8 which followed from precursors of CNT/ZIF-67. After sulfurization, it is obvious to see that pristine ZIF-67 particles would become CoS nanocages with hollow structure and obtuse edges, as shown in **Figure 4-5**. On the other hand, the sizes of CoS for the cases of CNT/CoS 1:2 and CNT/CoS 1:8 nanocages would shrink but still maintain the polyhedral structure after sulfurization. The synergistic interaction between interconnected CNT and CoS nanocage shall be helpful to enhance the electrochemical performance of SCs. However, it is not obvious to see the CoS particles in CNT/CoS 1:1, suggesting that the precursors of CNT/ZIF-67 1:1 with the smallest particle size of ZIF-67 would collapse after sulfurization (**Figure 4-6**). **Figure 4-7** presents the XRD patterns of as-synthesized CoS nanocage and hybrid CNT/CoS nanocages with various CNT/ZIF-67 as precursors. After sulfurization, the characteristic peaks of ZIF-67 disappeared, suggesting that the ZIF-67 based precursors may successfully transform into the cobalt sulfide. Notably, there is no obvious diffraction peaks assigned for the cobalt sulfide phase, demonstrating the amorphous nature of the as-synthesized CNT/CoS samples. This is similar to what has been reported in a previous literature that amorphous cobalt sulfide was obtained in ethylene glycol solvent.¹³⁶ Furthermore, for the case of CNT/CoS 1:1, the obvious diffraction peak of CNT for (002) plane at $\sim 26^\circ$ is observed due to its higher proportion of CNTs; while the intensity of the (002) diffraction peak of CNT in CNT/CoS 1:8 is rather low, suggesting that the surfaces of CNTs are highly covered by the amorphous cobalt sulfide.

To further confirm the chemical composition of as-synthesized cobalt sulfide, the XPS spectra of Co 2*p* orbitals and S 2*p* orbitals of CNT/CoS 1:2 are shown in **Figure 4-4b**. The Co 2*p* spectrum shows two strong peaks at 798.4 (2*p*_{1/2}) and 781.9 eV (2*p*_{3/2}) accompanied by two shake-up satellite peaks (786.3 and 802.9 eV), demonstrating the presence of both Co²⁺ and Co³⁺.^{56, 137} For XPS

spectrum of S 2p, the peak at 161.9 eV is assigned to cobalt sulfide.^{138, 139} The additional satellite peak at 169.2 eV is related to the S⁴⁺ species in sulfate groups.⁵⁶ For revealing more difference between the CoS nanocage and the hybrid CNT/CoS nanocage, the N₂ adsorption-desorption isotherms of CoS nanocage and hybrid CNT/CoS 1:2 nanocage were examined, as shown in **Figure 4-4c**. Both of the structures show the IV-type isotherms with hysteresis loop (**Figure 4-4c**), which is representative of the mesoporous materials. The result reveals the hysteresis loop of hybrid CNT/CoS 1:2 nanocage is larger than that of pristine CoS nanocage, indicating more mesopores in the structure of hybrid CNT/CoS 1:2 nanocage. Also, hybrid CNT/CoS 1:2 nanocage exhibits higher surface area (156.1 m² g⁻¹) than that of the pristine CoS nanocage (53.5 m² g⁻¹), suggesting that the hybrid CNT/CoS nanocage would offer more electrochemical surface area for utilizing in SCs.

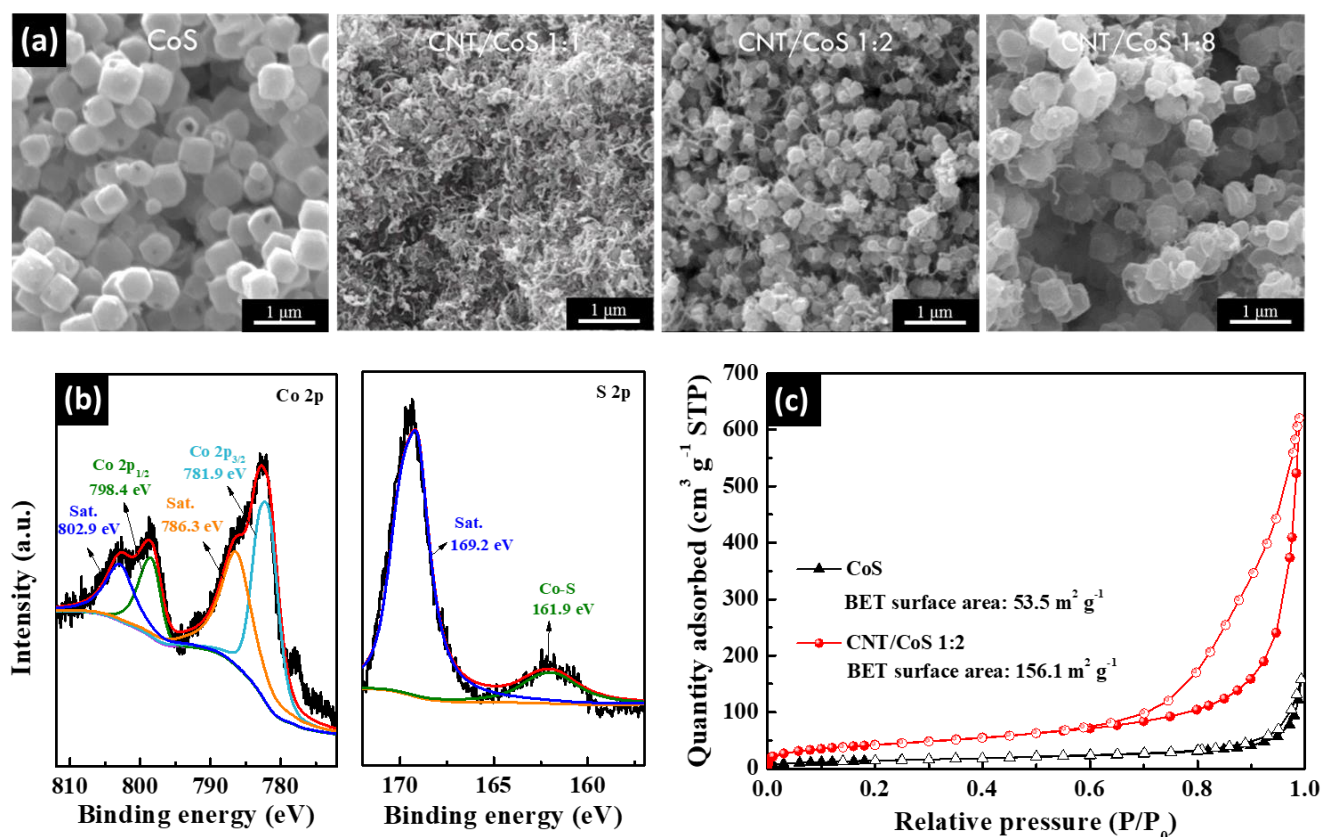


Figure 4-4 (a) FE-SEM image of CoS nanocage and hybrid CNT/CoS nanocages with various sizes of ZIF-67 as templates, (b) XPS spectra of Co 2p and S 2p for CNT/CoS 1:2 nanocages, and (c) N₂ adsorption-desorption isotherms of CoS nanocage and CNT/CoS 1:2 nanocages.

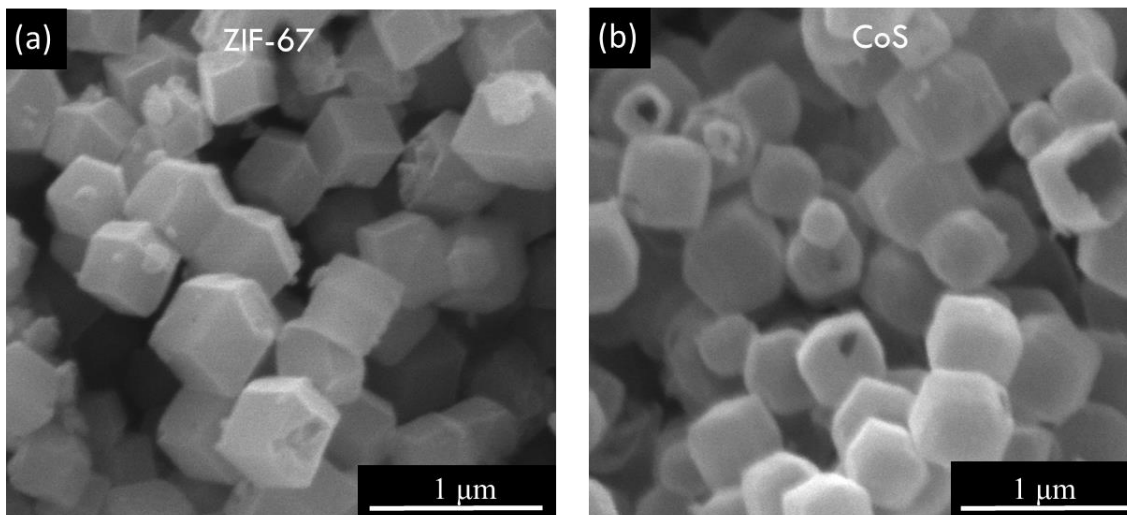


Figure 4-5 FE-SEM images of (a) ZIF-67 nanoparticles, and (b) CoS nanocages.

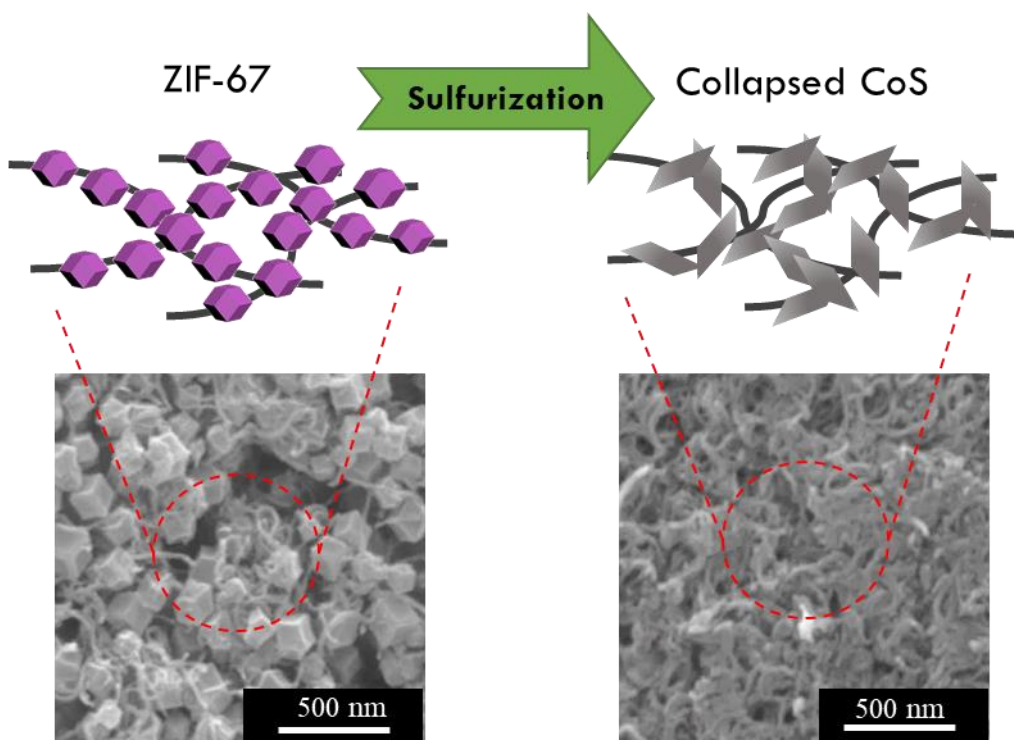


Figure 4-6 The schematic illustration of the collapsed CoS *via* sulfurization.

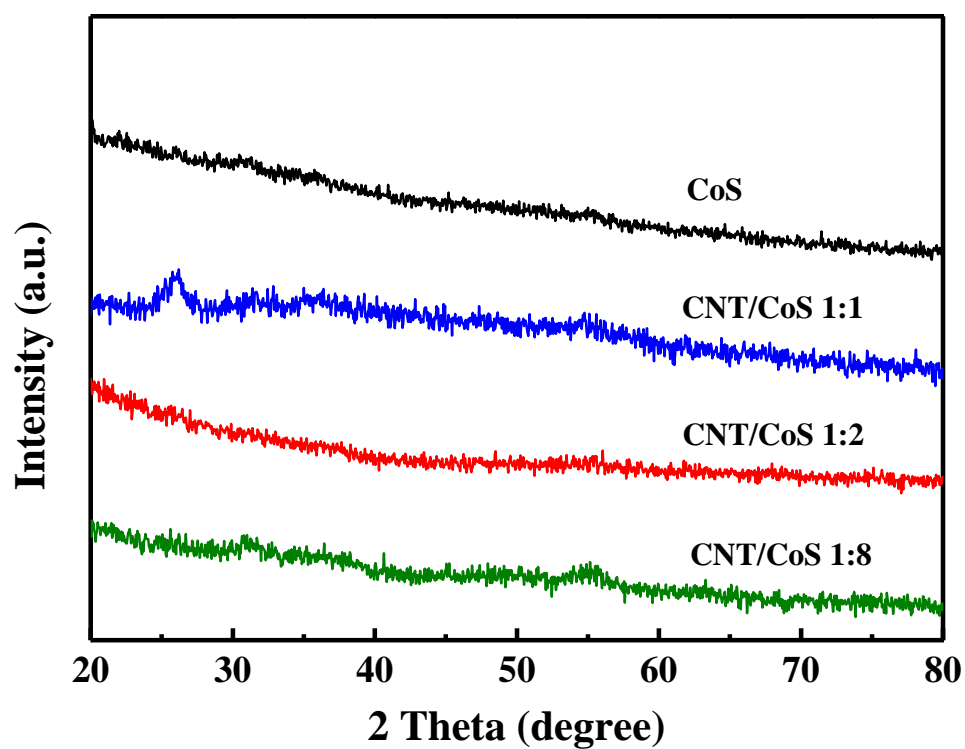
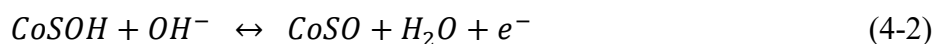


Figure 4-7 XRD patterns of CoS cage and hybrid CNT/CoS nanocages with various sizes of ZIF-67 as templates.

4-2-4 Electrochemical performance of CoS nanocage and hybrid CNT/CoS nanocages

In order to investigate the electrochemical performances of the as-synthesized CoS nanocage and hybrid CNT/CoS nanocage as the electrode materials in SCs, the cyclic voltammetry (CV) and the galvanostatic charge-discharge (GCD) were conducted with a three-electrode system in 6.0 M KOH. The electrochemical behaviors of CoS, CNT/CoS 1:1, CNT/CoS 1:2, and CNT/CoS 1:8 nanocage modified electrodes were investigated by CV curves in the potential range from -0.07 to 0.63 V (vs. Hg/HgO) at a scan rate of 100 mV s⁻¹, as shown in **Figure 4-8a**. The mechanism of the electrochemical redox reaction of cobalt sulfide in alkaline solution can be outlined as **Equations 4-1** and **4-2**,^{128, 140, 141}



It can be seen that all of the hybrid CNT/CoS nanocage based electrodes exhibit a larger integrated CV area than that of pristine CoS nanocage one, suggesting an enhancement in its specific capacitance attributed from the addition of CNT. Incorporating with faster charge transfer of CNT into amorphous CoS nanocage can enhance the overall conductivity of the composite.^{142, 143} Among different hybrid CNT/CoS nanocage electrodes, CNT/CoS 1:2 electrode shows the highest integrated CV area, implying more electrochemical surface area to provide active sites for the surface redox reaction. To further examine the electrochemical performance in detail, the galvanostatic charge-discharge (GCD) test is performed.¹⁴⁴ The calculation of the specific capacitance is according to **Equation 4-3**:

$$C_g = \frac{I \times \Delta t}{m \times \Delta V} \quad (4-3)$$

where C_g is the gravimetric capacitance (F g⁻¹), I is the current (A), Δt is the discharge time (s), m is the mass of the active electrode materials (g), and ΔV is the potential window (V). As shown in **Figure 4-8b**, the specific capacitance values for CoS, CNT/CoS 1:1, CNT/CoS 1:2, CNT/CoS 1:8 nanocage electrodes in the potential range of 0.08-0.48 V (vs. Hg/HgO) at a current density of 5 A g⁻¹ are 986.0, 657.3, 2173.1, 1587.1 F g⁻¹, respectively. This results demonstrate the better capacitance

behavior of the CNT/CoS 1:2 electrode, which is in good agreement with the results of the CVs. The reason for the superior capacitance of the CNT/CoS 1:2 nanocage can be promoted to the adequate addition of the CNTs for its high conductivity that could facilitate the rapid electron transfer, leading to better performance of the SC. Furthermore, according to the result of BET analysis (**Figure 4-8c**), the CNT/CoS 1:2 nanocage can provides surface area with more mesoporous structure for surface redox reaction and electrolyte penetration than that of pristine CoS nanocage. Notably, the capacitance value of the CNT/CoS 1:1 nanocage is lower than that of the CoS nanocage, which may correspond to the CoS with collapsed structure as revealed from SEM image (**Figure 4-6**); the precursors of ZIF-67 are less, and the particle sizes are small in the CNT/ZIF-67 1:1 nanocomposite, so the particles would barely remain after sulfurization, somehow influencing the electrochemical property. Moreover, this phenomenon may also implied that by further increasing the mass ratio of CNTs to CoS, the charge storage mechanism shall transfer from pseudocapacitance domain to EDLC domain, lowering its capacitance value.

Figure 4-8c shows the CV curves of the CNT/CoS 1:2 nanocage at various scan rates from 25 to 200 mV s⁻¹. The GCD curves of the CNT/CoS 1:2 nanocage electrode at different current densities from 5 to 20 A g⁻¹ are also presented in **Figure 4-8d**. The CV curves of other tested materials (**Figure 4-9**) are all of lower capacitance when compared with the CNT/CoS 1:2. From the discharge times, the specific capacitances of the CNT/CoS 1:2 nanocage electrode were calculated to be 2173.1, 1957.2, 1556.4 and 1410.1 F g⁻¹ at 5, 10, 15 and 20 A g⁻¹, respectively. The GCD curves of other tested materials were also performed (**Figure 4-10**). The specific capacitance values for CoS, CNT/CoS 1:1, CNT/CoS 1:2, CNT/CoS 1:8 nanocage electrodes at a current density of 5 A g⁻¹ are displayed in **Figure 4-8e**. It is worth to mention that the specific capacitance of the CNT/CoS 1:8 is lower than that of the CNT/CoS 1:2, suggesting that it not only diminished the electrical conductivity with low mass ratio of CNT to CoS but also reduced the surface area with bigger size of CoS, thus influencing the electrochemical performance. To compare the rate capability of the as-synthesized CoS nanocage and the hybrid CNT/CoS nanocages, the specific capacitances of them at different current densities are shown in **Figure 4-8f**. It demonstrates that the specific capacitance values

increase as the current densities decrease. At low current density, electrolyte ions can penetrate into the inner structure of the nanocages, making use of the active materials, which brings about high capacitance. Conversely, the capacitance decreases at high current density due to the inadequate involvement of the active materials in redox reaction.^{33, 34} It is obvious to see that the specific capacitances of the CNT/CoS 1:2 nanocage electrode are higher than those of other electrodes in all current densities. The CNT/CoS 1:2 nanocage electrode still maintains 65% of its initial capacitance as the current density is up to 20 A g⁻¹, indicating its good rate capability.

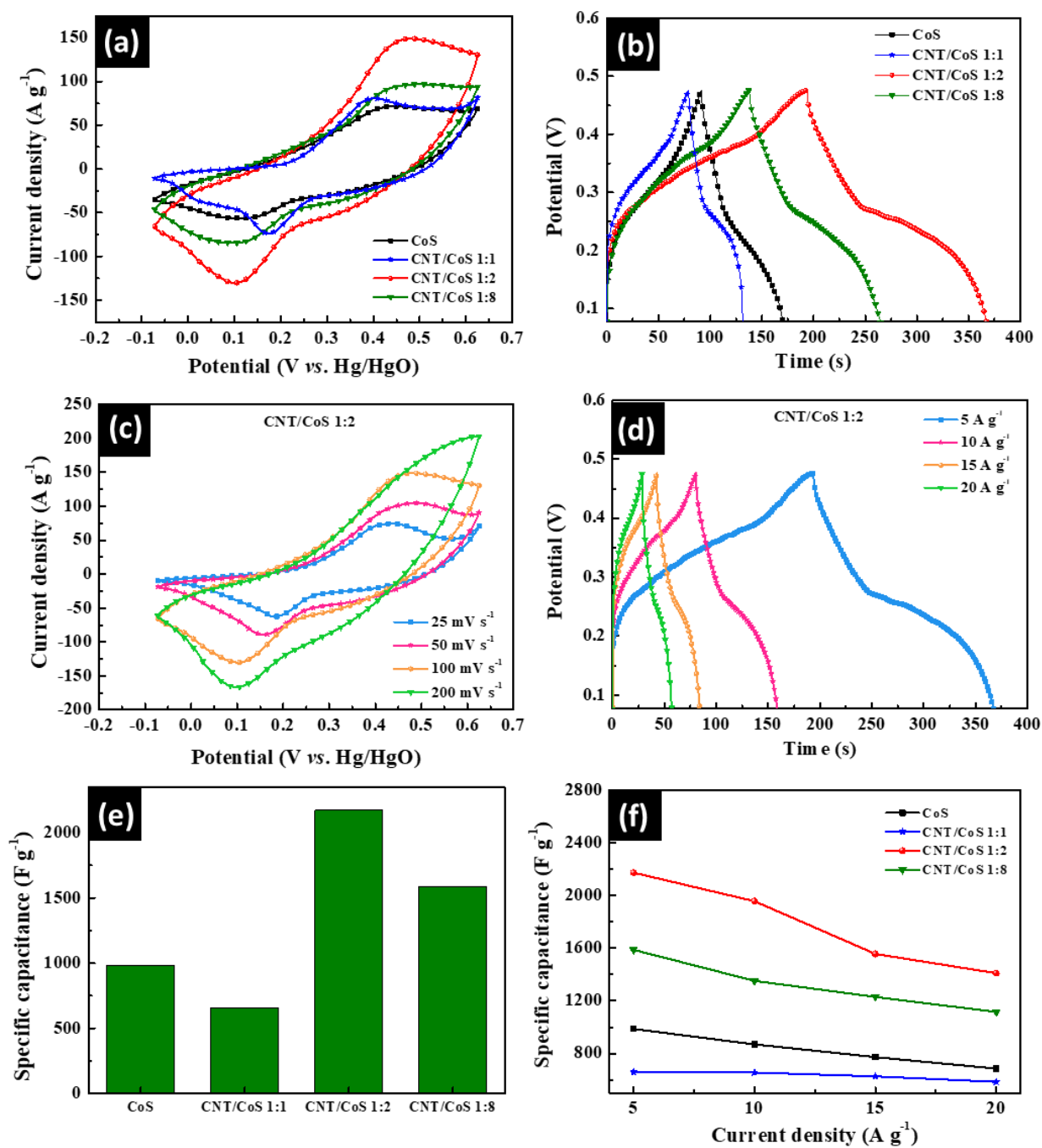


Figure 4-8 (a) Cyclic voltammograms (CVs) at a scan rate of 100 mV s⁻¹, (b) galvanostatic charge-discharge (GCD) curves at a current density of 5 A g⁻¹ of CoS, CNT/CoS 1:1, CNT/CoS 1:2, and CNT/CoS 1:8 nanocage electrodes, (c) CVs of CNT/CoS 1:2 electrodes at different scanning rates, (d) GCD curves of CNT/CoS 1:2 nanocage electrodes at different current densities, (e) comparison of the specific capacitance performance of CoS, CNT/CoS 1:1, CNT/CoS 1:2, and CNT/CoS 1:8 nanocage electrodes at a current density of 5 A g⁻¹, and (f) comparison of the specific capacitance values at various current densities of the nanocages.

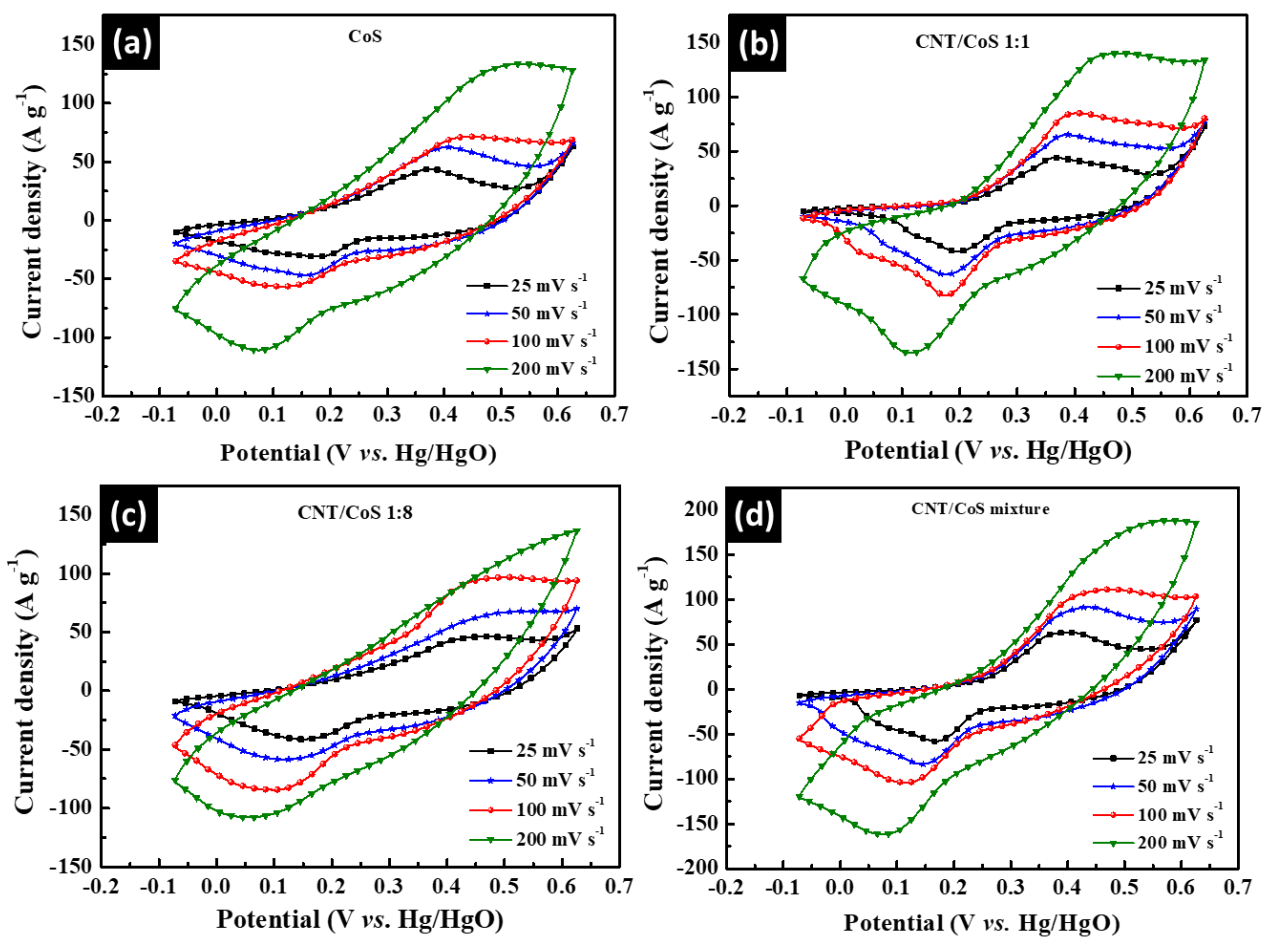


Figure 4-9 CVs of (a) CoS nanocage, (b) CNT/CoS 1:1 nanocage, (c) CNT/CoS 1:8 nanocage, and (d) CNT/CoS mixture electrodes at different scan rates.

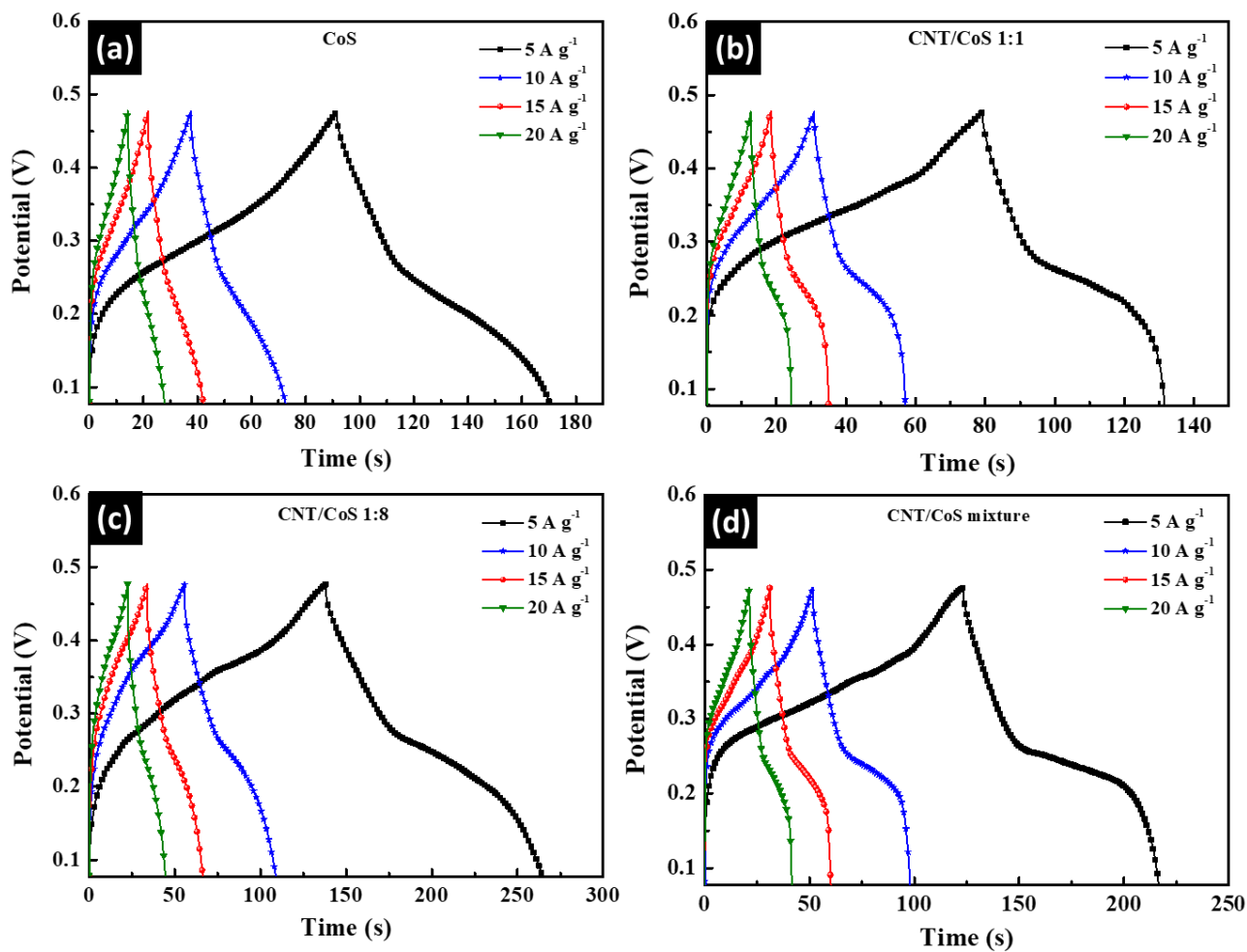


Figure 4-10 GCD curves of (a) CoS nanocage, (b) CNT/CoS 1:1 nanocage, (c) CNT/CoS 1:8 nanocage, and (d) CNT/CoS mixture electrodes at different current densities.

4-2-5 Electrochemical analyses of CoS nanocage and hybrid CNT/CoS nanocages

To further investigate the electrochemical behaviors of the electrodes, electrochemical impedance spectroscopy (EIS) was utilized to examine the charge transfer resistance of the as-synthesized nanocages. **Figure 4-11a** shows the Nyquist plots of CoS nanocage and hybrid CNT/CoS nanocages in the frequency range from 100 kHz to 0.1 Hz. The inset of **Figure 4-11a** shows the electrical equivalent circuit employed for EIS fitting. The equivalent circuit consists of the series resistance of the overall system (R_s), the charge transfer resistance (R_{ct}), the finite-length Warburg diffusion element (W_o), and the double-layer capacitance (C_{DL}). In particular, R_{ct} can be measured from the region of the semicircle in the Nyquist plot. The R_{ct} value determines the charge transport kinetics at the electrode/electrolyte interface; a lower R_{ct} value would lead to an enhanced electrochemical performance of the electrode materials. **Figure 4-11b** shows that the R_{ct} value of the CNT/CoS 1:2 is 0.079 Ω , which was much lower than that of the CoS (0.262 Ω), CNT/CoS 1:1 (0.451 Ω) and CNT/CoS 1:8 (0.197 Ω), indicating the faster electron transfer and ion transport. The results also reveals that collapsed CoS may obstruct the electron transfer since the R_{ct} value of the CNT/CoS 1:1 is much higher than other samples. Moreover, the excellent capacitor characteristics of the electrode was verified by its linear part observed at low frequencies. Therefore, the EIS results further confirm that the CNT/CoS 1:2 is an excellent material for the electrode of SCs.

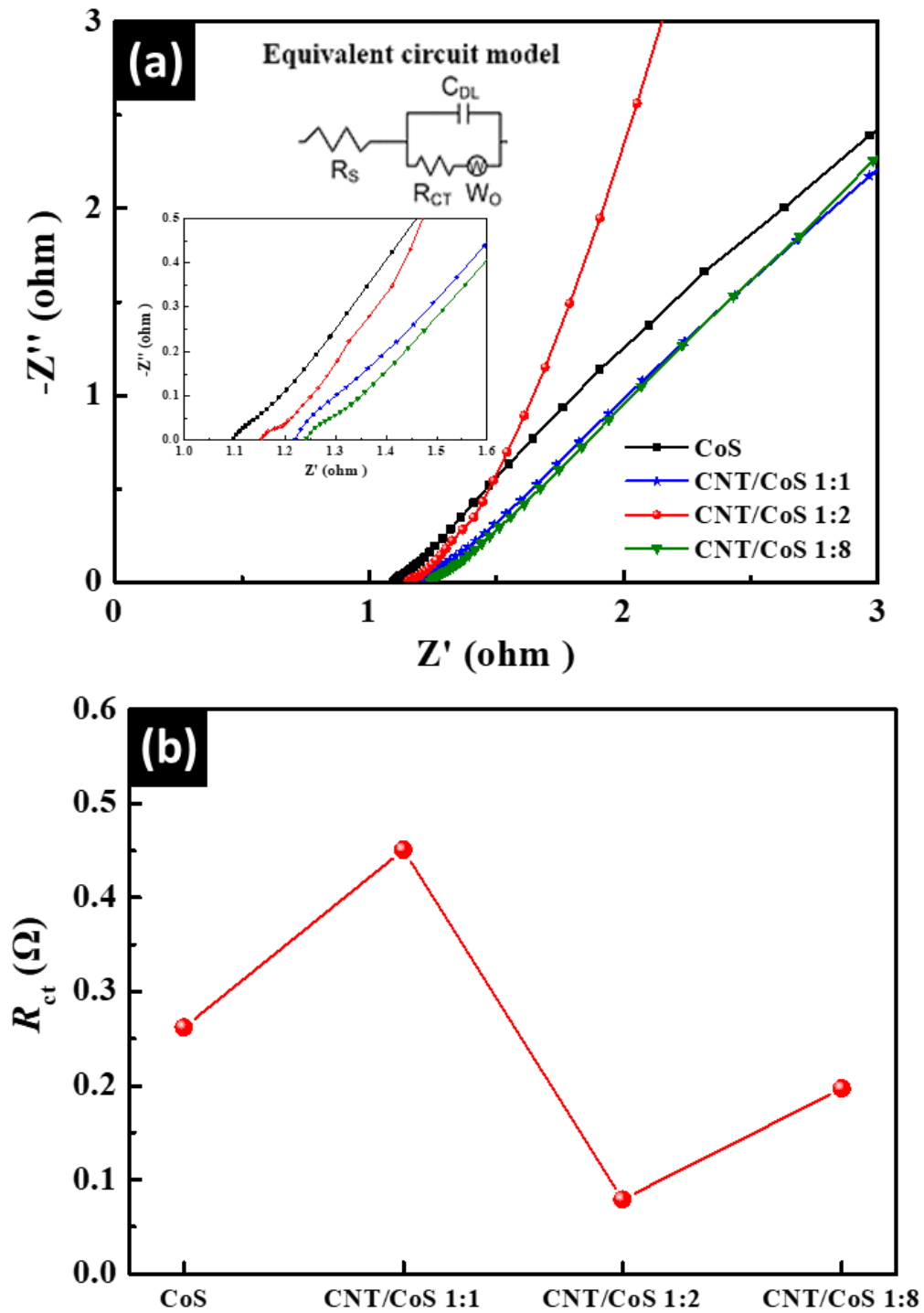


Figure 4-11 (a) Nyquist plots (magnified plot in high frequency range and electrical equivalent circuit was also included as the inset), and (b) R_{ct} values (obtained from Figure 4-11a) of CoS, CNT/CoS 1:1, CNT/CoS 1:2 and CNT/CoS 1:8 nanocages with the frequency range from 100 kHz to 0.1 Hz.

4-2-6 Comparison of hybrid CNT/CoS nanocage and physical mixture of CNT/CoS

To highlight the importance of the CNTs inserted homogeneously in CoS nanocages, the hybrid CNT/CoS 1:2 nanocage was compared with the physical mixture in the mass ratio of 1 to 2 of CNTs and CoS nanocage. In the following comparisons, the hybrid CNT/CoS 1:2 nanocage was abbreviated as CNT/CoS nanocage, and the physical mixture was denoted as CNT/CoS mixture. In **Figure 4-12a**, compared to the CNT/CoS nanocage, the SEM image of the CNT/CoS mixture reveal that CoS nanocages were not inserted by CNTs uniformly. CNTs and CoS nanocages became agglomerate separately; this phenomenon may strongly impacts on the electrochemical performance. As shown in **Figure 4-12b**, the specific capacitance values for the CNT/CoS nanocage and the CNT/CoS mixture at a current density of 5 A g⁻¹ are 2173.1 and 1164.7 F g⁻¹ respectively. The reason for the superior capacitance of the CNT/CoS nanocage can be attributed to the distributed CoS nanocages homogeneously interconnected by CNTs, providing high electrical conductivity and both contributions of EDLC and pseudocapacitance. **Figure 4-12c** also shows the Nyquist plots of the CNT/CoS nanocage and the CNT/CoS mixture; the R_{ct} value of the CNT/CoS nanocage (0.079 Ω) is lower than that of physical mixture one (0.241 Ω), once again confirming the faster electron transfer and ion transport. Cycling stability is also a very vital factor for the practical applications of SCs. To further investigate the cycling performance of the CNT/CoS nanocage, GCD curves of the CNT/CoS nanocage and CNT/CoS mixture were measured in 6.0 M KOH at a current density of 5 A g⁻¹ for 1,000 cycles. According to **Figure 4-12d**, the specific capacitance of the CNT/CoS nanocage remained 91% of its initial value after 1000 cycles, demonstrating a good cycling stability. As a comparison, the CNT/CoS mixture only shows 82.1% maintained after 1000 cycles. The excellent electrochemical properties of the CNT/CoS nanocage can be ascribed to the introduction of CNT into amorphous CoS nanocage, which may not only enhances the electrical conductivity and promotes the charge transfer, but also prevents the agglomeration of the nanocages and increases the active sites for the charge storage. Moreover, the existence of CNTs can induce more porosity of the nanocages, thus facilitating the ion diffusion. Furthermore, the Ragone plot was used to evaluate the performance of the supercapacitors. The energy density (E , Wh kg⁻¹) and power density (P , W kg⁻¹) can be

calculated using **Equation 4-4** and **4-5**:¹⁴²

$$E = \left(\frac{1}{2} C_g \Delta V^2\right) / 3.6 \quad (4-4)$$

$$P = (3600 \times E) / \Delta t \quad (4-5)$$

where C_g is the gravimetric capacitance ($F\ g^{-1}$), ΔV is the potential window (V), and Δt is the discharge time (s). As shown in **Figure 4-12e**, at a current density of $5\ A\ g^{-1}$, the energy density of the optimized CNT/CoS nanocage reached $48.29\ Wh\ kg^{-1}$ at a power density of $1000.0\ W\ kg^{-1}$, and remained at $31.34\ Wh\ kg^{-1}$ at the power density of $4000.3\ W\ kg^{-1}$ when the current density was up to $20\ A\ g^{-1}$, which was much higher than the performance of the CoS nanocage ($21.91\ Wh\ kg^{-1}$, $1000.0\ W\ kg^{-1}$, $5\ A\ g^{-1}$) and the CNT/CoS mixture ($25.88\ Wh\ kg^{-1}$, $1000.0\ W\ kg^{-1}$, $5\ A\ g^{-1}$). A comparison of the electrochemical performance of the optimized CNT/CoS nanocage with MOF-derived cobalt sulfide and carbon/cobalt sulfide materials in SCs is listed in **Table 4-1**. These results indicate that hybrid CNT/CoS nanocage is a promising supercapacitor electrode material for applying in high-rate applications.

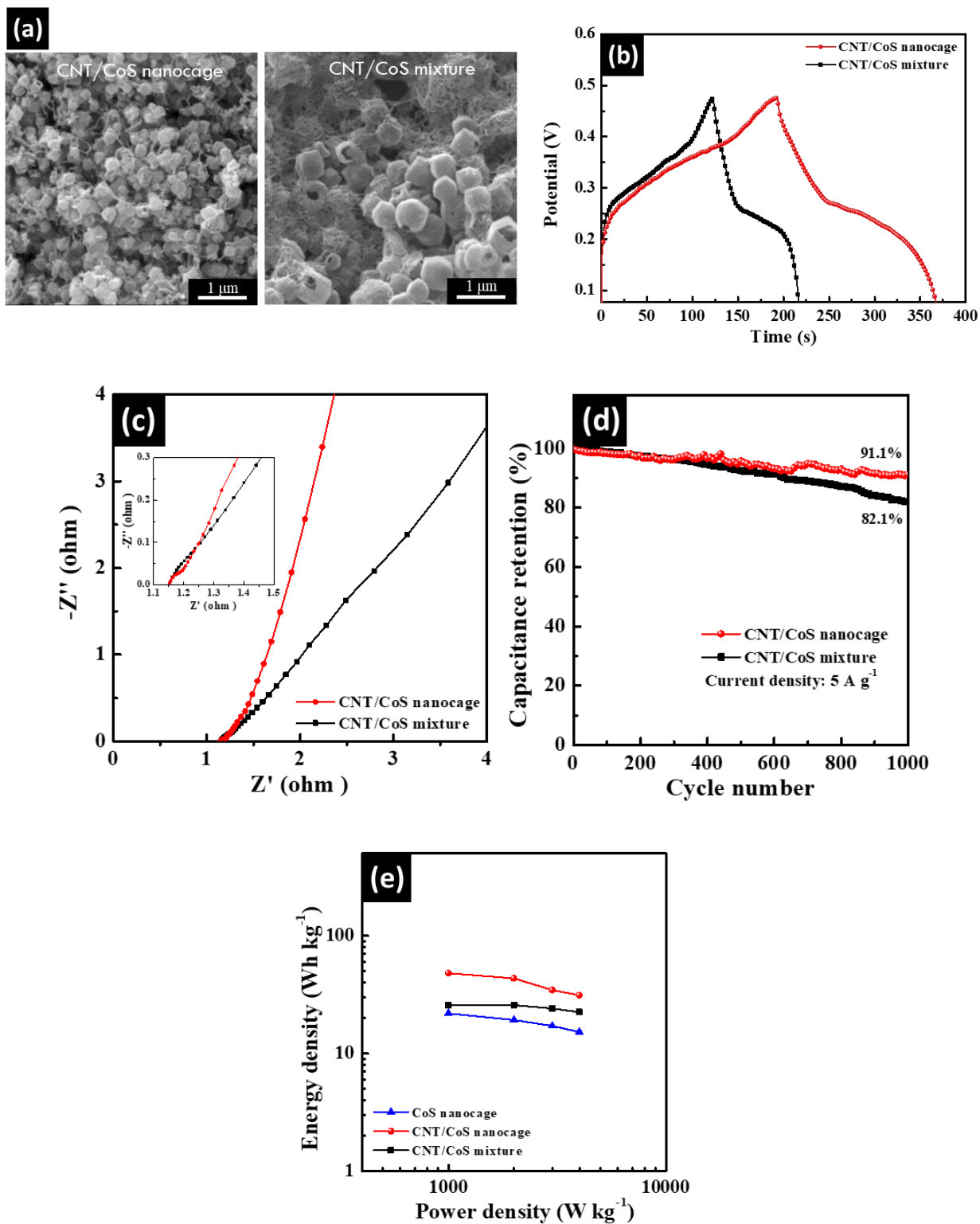


Figure 4-12 (a) FE-SEM image, (b) GCD curves at a current density of 5 A g^{-1} , (c) Nyquist plots, (d) cycling performance at a current density of 5 A g^{-1} of CNT/CoS nanocage and CNT/CoS mixture nanocages, and (e) Ragone plot of CoS nanocage, CNT/CoS nanocage and CNT/CoS mixture under various current densities.

Table 4-1 A list of ^a MOF-derived cobalt sulfide and ^b carbon/cobalt sulfide materials in the application of supercapacitors, compared to that obtained in this work. ^c Co₉S₈ embedded in carbon co-doped with N and S. ^d Co₉S₈@S, N-doped carbon cuboid. ^e CoS-nanoparticle-assembled nanoboxes surrounded by outer CoS-nanosheet-constructed shells. ^f Co_xS@porous carbon/RGO. ^g conductive polymer/rGO/Co₉S₈.

Materials	Electrolyte	Capacitance gravimetric F g ⁻¹ (Condition, vs. Hg/HgO)	Capacitance retention	Ref.
Co ₉ S ₈ -nanosheet array ^a	1.0 M KOH	1098.8 (0.15 – 0.55 V, 0.5 A g ⁻¹)	1000 (87.4%)	56
CoS nanocages ^a	1.0 M KOH	1475 (-0.15 – 0.35 V, 1 A g ⁻¹)	3000 (70.3%)	128
Co ₉ S ₈ /NS-C ^{a, b, c}	6.0 M KOH	734.09 (0 – 0.5 V, 1 A g ⁻¹)	140000 (99.8%)	138
Co ₉ S ₈ @SNCC ^{a, b, d}	6 M KOH	429 (-1.1 – -0.6V, 1 A g ⁻¹)	2000 (98%)	139
Zn-Co-S ^a	6.0 M KOH	1266 (0.15 – 0.65 V, 1 A g ⁻¹)	10000 (91%)	145
CoS-NP/CoS-NS ^{a, e}	2.0 M KOH	980 (0.15 – 0.70 V, 1 A g ⁻¹)	10000 (89%)	146
CoS-N-doped carbon ^{a, b}	2.0 M KOH	360.1 (0.1 – 0.7 V, 1.5 A g ⁻¹)	2000 (90%)	147
Co _x S@PC/RGO ^{a, b, f}	1.0 M KOH	455 (0.15 – 0.65 V, 2 A g ⁻¹)	4000 (99.7%)	148
CoS _x /FMWCNTs ^b	2.0 M KOH	334 (-0.15 – 0.60 V, 0.4 A g ⁻¹)	1000 (95%)	149
CNT/CoS ^b	1.0 M KOH	1332.8 (0.15 – 0.65 V, 217.4 A g ⁻¹)	1500 (91%)	150
CoS/CNT ^b	6.0 M KOH	804 (0.15– 0.65 V, 0.5 A g ⁻¹)	1000 (93.4%)	151
rGO ₁₀₀ -CNT ₅₀ -Co ₃ S ₄ ^b	6.0 M KOH	977 (0.15 – 0.65 V, 1 A g ⁻¹)	3000 (90%)	142

RGO/CoS ^b	6.0 M KOH	1130 (0.15 – 0.65 V, 0.5 A g ⁻¹)	1000 (92.1%)	152
cP/rGO/Co ₉ S ₈ ^{b, g}	2.0 M KOH	788.9 (0.1 – 0.55 V, 1 A g ⁻¹)	10000 (over 100%)	153
CoS@rGO ^b	2.0 M KOH	849 (0 – 0.55 V, 5 mA cm ⁻²)	3000 (90.5%)	154
Co ₃ S ₄ /rGO ^b	2.0 M KOH	675.9 (0 – 0.5 V, 0.5 A g ⁻¹)	1000 (over 100%)	155
CoS/rGO ^b	6.0 M KOH	550 (0.15– 0.55 V, 1A g ⁻¹)	5000 (95%)	156
Co ₃ S ₄ -rGO ^b	2.0 M KOH	2314 (-0.15 – 0.75 V, 2 mV/s)	1000 (92.6%)	157
Co ₉ S ₈ /reduced graphene ^b	6.0 M KOH	728 (0.15 – 1.15 V, 2 A g ⁻¹)	1000 (97%)	158
Co ₉ S ₈ /RGO ^b	6.0 M KOH	616 (0 – 0.8 V, 4.4 A g ⁻¹)	1000 (98%)	159
PANI-rGO-CoS ^b	1.0 M H ₂ SO ₄	431 (0.15 – 0.95 V, 0.5A g ⁻¹)	1000 (90.1%)	160
CoS/graphene ^b	2.0 M KOH	3386 (0.05– 0.55 V, 1 A g ⁻¹)	2500 (31.1%)	161
CoS/graphene ^b	6.0 M KOH	564 (0.1 – 0.55 V, 1 A g ⁻¹)	2000 (94.8%)	162
CoS/graphene ^b	6.0 M KOH	2423.3 (-0.7 – 0.1 V, 5 mV/s)	-	163
Co ₉ S ₈ /3D graphene ^b	1.0 M KOH	2317 (0.1 – 0.55 V, 1 A g ⁻¹)	6000 (90%)	164
3D graphene/CoS _x ^b	1.0 M KOH	443 (0 – 0.6 V, 1 A g ⁻¹)	5000 (86%)	165
Co ₃ S ₄ -N-doped graphene ^b	6.0 M KOH	2245 (0.05– 0.3 V, 3 A g ⁻¹)	-	166

g-C₃N₄/CoS^b

3.0 M KOH

668
(0.15 – 0.55 V, 2 A g⁻¹)

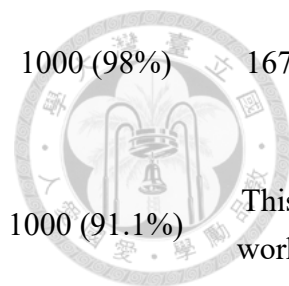
1000 (98%) 167

Hybrid CNT/CoS
nanocage^{a, b}

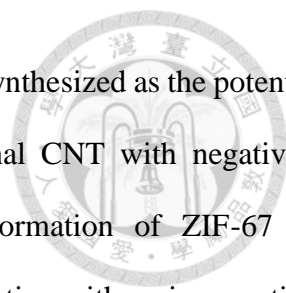
6.0 M KOH

2173.1
(0.08 – 0.48 V, 5 A g⁻¹)

1000 (91.1%) This
work



4-3 Conclusions



In summary, a hybrid structure of CNT/CoS nanocage is successfully synthesized as the potential electrode material of SCs. In the ZIF-67 growth reaction, the functional CNT with negatively carboxyl groups can serve as nucleation sites for facilitating the formation of ZIF-67 by heterogeneous nucleation, thus to control the size of ZIF-67. After sulfurization with various particle size of ZIF-67 as template, the hybrid CNT/CoS nanocages composited with the polyhedral structure of ZIF-67 derived CoS with interconnected CNT chains were discussed. Due to the optimized ratio of CNT to CoS and suitable size of CoS nanocage, electrochemical studies showed the CNT/CoS 1:2 nanocage exhibits an outstanding specific capacitance of 2173.1 F g⁻¹ at a current density of 5 A g⁻¹ (pristine CoS: 986 F g⁻¹), and the capacitance retention is 91% over 1000 cycles, demonstrating a great potential in energy applications. Moreover, the energy density of the optimized CNT/CoS nanocage reached 48.29 Wh kg⁻¹ (pristine CoS: 21.91 Wh kg⁻¹) at a power density of 1000.0 W kg⁻¹, and remained at 31.34 Wh kg⁻¹ when the current density was up to 20 A g⁻¹. Based on the experience of this work, the controllable synthesis strategy of ZIF based crystals and their derivatives can be extended to synthesize other metal oxide or metal sulfide incorporated porous graphitic carbon composites with controllable sizes and morphology for a variety of energy storage applications.

Chapter 5

Conclusions and suggestions



5-1 General conclusions

Nowadays, due to ever-increasing concerns related to nonrenewable energy depletion and environmental pollution, there is a urgent need for the development of high-performance energy storage and conversion technologies. Extensive researches have demonstrated that ZIFs can function as ideal templates for the facile preparation of various nanostructures. ZIFs, as a novel class of porous crystalline materials, exhibit a wide range of applications, especially in the field of energy storage and conversion including supercapacitors and DSSCs. The advantages of ZIFs, including high porosity, adjustable pore size, excellent mechanical stability, controllable structure and exceptional chemical and thermal stabilities make great contributions to their electrochemical performance. However, the performance of MOFs in most of these applications are not yet satisfactory.^{168, 169}

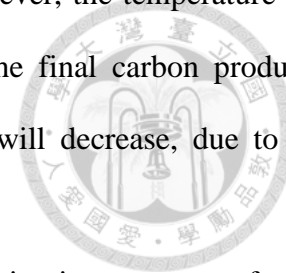
5-2 Suggestions

In this section, we would like to discuss some issues that could be helpful to the people who would like to follow the research in this thesis. For instance, despite much progress on the development of various ZIFs-derived nanostructures, more precise control of the chemical compositions and fine nanostructures still remains challenging due to a limited understanding of pyrolysis or carbonization processes. Another common issue for ZIFs is their limited electronic conductivity due to the existence of organic linkers. With further research, high conductivity ZIFs are expected to be developed and used in electrochemical devices.

5-2-1 Suggestions for Chapter 3

First, for MOF-derived carbons, nitrogen can be easily doped into the carbons through the one-step pyrolysis of MOFs at high temperature, which would be beneficial for improving electrical

conductivity and electrochemical activity of MOF-derived carbons. However, the temperature and organic linkers significantly affect the amount of doped nitrogen in the final carbon products. Generally, by increasing temperatures, the amount of doped nitrogen will decrease, due to the instability of nitrogen at high temperature.



To achieve a high nitrogen doping level, organic linkers that are rich in nitrogen are preferred. Therefore, other types of imidazolate linkers can be chosen to synthesize the MOF-derived carbons in the future research. Also, heteroatom atoms, such as N, S and P, can be doped into the composites to further enhance the performance of MOF-derived porous carbon.

Besides, the key concept of this work is to propose a new strategy for the application of ZIFs as precursors in the field of photovoltaic devices. Based on the results obtained from this work, more attractive materials can be synthesized through different chemical modifications (including nitridation, sulfuration, *etc.*) using a variety of MOF-derived precursors. Therefore, more eco-friendly materials for the use in DSSCs with high photovoltaic performance can be expected in the future.

5-2-2 Suggestions for Chapter 4

MOFs and MOF-derived nanomaterials show great potential in the field of energy storage and conversion due to their unique properties. However, to meet the requirements for commercialization, further research is required.

The controllable synthesis strategy of ZIF crystals and their derivatives used in this work can be extended to synthesize other metal oxide or metal sulfide incorporated porous graphitic carbon composites with controllable sizes and morphology for a variety of energy storage applications.

The use of aqueous electrolyte will result in the restriction in operating voltage due to the water decomposition. It has been known that lowering the operating voltage will lead to a lower energy density which is disadvantageous to the practical applications. Moreover, the use of aqueous electrolyte will encounter extremely difficulty in packing a device because of the electrolyte leakage and corrosion. Therefore, the use of gel or solid electrolytes can be studied for future researches. Thus, many efforts are needed to fabricate devices under proper conditions based on this nanocomposite.

References

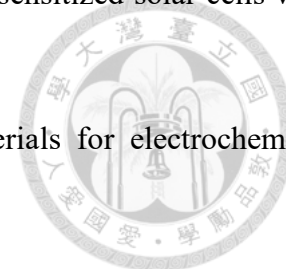


1. M. E. Davis, Ordered porous materials for emerging applications, *Nature*, 2002, **417**, 813-821.
2. O. M. Yaghi, G. Li and H. Li, Selective binding and removal of guests in a microporous metal–organic framework, *Nature*, 1995, **378**, 703-706.
3. C. Zhang, Y. Dai, J. R. Johnson, O. Karvan and W. J. Koros, High performance ZIF-8/6FDA-DAM mixed matrix membrane for propylene/propane separations, *Journal of Membrane Science*, 2012, **389**, 34-42.
4. B. Chen, Z. Yang, Y. Zhu and Y. Xia, Zeolitic imidazolate framework materials: recent progress in synthesis and applications, *Journal of Materials Chemistry A* 2014, **2**, 16811-16831.
5. A. Phan, C. J. Doonan, F. J. Uribe-Romo, C. B. Knobler, M. O’keeffe and O. M. Yaghi, Synthesis, structure, and carbon dioxide capture properties of zeolitic imidazolate frameworks, *Accounts of Chemical Research*, 2010, **43**, 58-67.
6. K. S. Park, Z. Ni, A. P. Côté, J. Y. Choi, R. Huang, F. J. Uribe-Romo, H. K. Chae, M. O’Keeffe and O. M. Yaghi, Exceptional chemical and thermal stability of zeolitic imidazolate frameworks, *Proceedings of the National Academy of Sciences*, 2006, **103**, 10186-10191.
7. X. C. Huang, Y. Y. Lin, J. P. Zhang and X. M. Chen, Ligand-directed strategy for zeolite-type metal–organic frameworks: zinc (II) imidazolates with unusual zeolitic topologies, *Angewandte Chemie*, 2006, **118**, 1587-1589.
8. M. He, J. Yao, L. Li, K. Wang, F. Chen and H. Wang, Synthesis of zeolitic imidazolate framework-7 in a water/ethanol mixture and its ethanol-induced reversible phase transition, *ChemPlusChem*, 2013, **78**, 1222-1225.
9. T. D. Bennett, P. J. Saines, D. A. Keen, J. C. Tan and A. K. Cheetham, Ball-milling-induced amorphization of zeolitic imidazolate frameworks (ZIFs) for the irreversible trapping of iodine, *Chemistry*, 2013, **19**, 7049-7055.
10. Y. V. Kaneti, S. Dutta, M. S. A. Hossain, M. J. A. Shiddiky, K. L. Tung, F. K. Shieh, C. K.

- Tsung, K. C. Wu and Y. Yamauchi, Strategies for improving the functionality of zeolitic imidazolate frameworks: tailoring nanoarchitectures for functional applications, *Advanced Materials*, 2017, **29**, 1700213-1700243.
11. F. K. Shieh, S. C. Wang, S. Y. Leo and K. C. Wu, Water-based synthesis of zeolitic imidazolate framework-90 (ZIF-90) with a controllable particle size, *Chemistry*, 2013, **19**, 11139-11142.
12. H. Jing, X. Song, S. Ren, Y. Shi, Y. An, Y. Yang, M. Feng, S. Ma and C. Hao, ZIF-67 derived nanostructures of Co/CoO and Co@N-doped graphitic carbon as counter electrode for highly efficient dye-sensitized solar cells, *Electrochimica Acta*, 2016, **213**, 252-259.
13. X. Li, C. Hao, B. Tang, Y. Wang, M. Liu, Y. Wang, Y. Zhu, C. Lu and Z. Tang, Supercapacitor electrode materials with hierarchically structured pores from carbonization of MWCNTs and ZIF-8 composites, *Nanoscale*, 2017, **9**, 2178-2187.
14. M. A. Nasalevich, M. van der Veen, F. Kapteijn and J. Gascon, Metal–organic frameworks as heterogeneous photocatalysts: advantages and challenges, *CrystEngComm*, 2014, **16**, 4919-4926.
15. A. Yella, H.-W. Lee, H. N. Tsao, C. Yi, A. K. Chandiran, M. K. Nazeeruddin, E. W.-G. Diao, C.-Y. Yeh, S. M. Zakeeruddin and M. Grätzel, Porphyrin-sensitized solar cells with cobalt (II/III)–based redox electrolyte exceed 12 percent efficiency, *Science*, 2011, **334**, 629-634.
16. S. Mathew, A. Yella, P. Gao, R. Humphry-Baker, B. F. Curchod, N. Ashari-Astani, I. Tavernelli, U. Rothlisberger, M. K. Nazeeruddin and M. Grätzel, Dye-sensitized solar cells with 13% efficiency achieved through the molecular engineering of porphyrin sensitizers, *Nature chemistry*, 2014, **6**, 242-247.
17. K. Kakiage, Y. Aoyama, T. Yano, K. Oya, J. i. Fujisawa and M. Hanaya, Highly-efficient dye-sensitized solar cells with collaborative sensitization by silyl-anchor and carboxy-anchor dyes, *Chemical Communications*, 2015, **51**, 15894-15897.
18. F. Huang, D. Chen, X. L. Zhang, R. A. Caruso and Y. B. Cheng, Dual-function scattering layer of submicrometer-sized mesoporous TiO₂ beads for high-efficiency dye-sensitized solar cells, *Advanced Functional Materials*, 2010, **20**, 1301-1305.

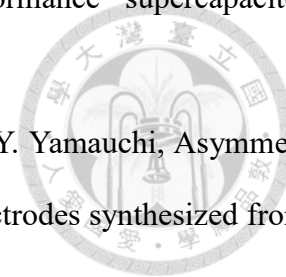
19. S. Ahmad, E. Guillén, L. Kavan, M. Grätzel and M. K. Nazeeruddin, Metal free sensitizer and catalyst for dye-sensitized solar cells, *Energy & Environmental Science*, 2013, **6**, 3439-3466.
20. C. P. Lee, R. Y.-Y. Lin, L. Y. Lin, C. T. Li, T. C. Chu, S. S. Sun, J. T. Lin and K. C. Ho, Recent progress in organic sensitizers for dye-sensitized solar cells, *RSC Advances*, 2015, **5**, 23810-23825.
21. C. T. Li, C. P. Lee, C. T. Lee, S. R. Li, S. S. Sun and K. C. Ho, Iodide-free ionic liquid with dual redox couples for dye-sensitized solar cells with high open-circuit voltage, *ChemSusChem*, 2015, **8**, 1244-1253.
22. A. Listorti, B. O'Regan and J. R. Durrant, Electron transfer dynamics in dye-sensitized solar cells, *Chemistry of Materials*, 2011, **23**, 3381-3399.
23. A. G. Anneke Hauch, Diffusion in the electrolyte and charge-transfer reaction at the platinum electrode in dye-sensitized solar cells, *Electrochimica Acta*, 2001, **46**, 3457-3466.
24. Y. Hou, D. Wang, X. H. Yang, W. Q. Fang, B. Zhang, H. F. Wang, G. Z. Lu, P. Hu, H. J. Zhao and H. G. Yang, Rational screening low-cost counter electrodes for dye-sensitized solar cells, *Nature Communications*, 2013, **4**, 1583-1590.
25. Q. Tai and X.-Z. Zhao, Pt-free transparent counter electrodes for cost-effective bifacial dye-sensitized solar cells, *Journal of Materials Chemistry A*, 2014, **2**, 13207-13218.
26. M. Wu, X. Lin, Y. Wang, L. Wang, W. Guo, D. Qi, X. Peng, A. Hagfeldt, M. Grätzel and T. Ma, Economical Pt-free catalysts for counter electrodes of dye-sensitized solar cells, *Journal of the American Chemical Society*, 2012, **134**, 3419-3428.
27. L. Wang, M. Wu, Y. Gao and T. Ma, Highly catalytic counter electrodes for organic redox couple of thiolate/disulfide in dye-sensitized solar cells, *Applied Physics Letters*, 2011, **98**, 221102-221104.
28. G. H. Espen Olsen, Sten Eric Lindquist, Dissolution of platinum in methoxy propionitrile containing LiI/I_2 , *Solar Energy Materials & Solar Cells*, 2000, **63**, 267-273.
29. E. Ramasamy, C. Jo, A. Anthonysamy, I. Jeong, J. K. Kim and J. Lee, Soft-template simple synthesis of ordered mesoporous titanium nitride-carbon nanocomposite for high performance

- dye-sensitized solar cell counter electrodes, *Chemistry of Materials*, 2012, **24**, 1575-1582.
30. S. A. Sapp, C. M. Elliott, C. Contado, S. Caramori and C. A. Bignozzi, Substituted polypyridine complexes of cobalt (II/III) as efficient electron-transfer mediators in dye-sensitized solar cells, *Journal of the American Chemical Society*, 2002, **124**, 11215-11222.
31. W. Maiaugree, N. Kongprakaiwoot, A. Tangtrakarn, S. Saekow, S. Pimanpang and V. Amornkitbamrung, Efficiency enhancement for dye-sensitized solar cells with a porous NiO/Pt counter electrode, *Applied Surface Science*, 2014, **289**, 72-76.
32. X. Chen, Q. Tang, B. He, L. Lin and L. Yu, Platinum-free binary Co-Ni alloy counter electrodes for efficient dye-sensitized solar cells, *Angewandte Chemie International Edition*, 2014, **53**, 10799-10803.
33. T. T. Duong, T. Q. Tuan, D. V. A. Dung, N. Van Quy, D. L. Vu, M. H. Nam, N. D. Chien, S. G. Yoon and A. T. Le, Application of polyaniline nanowires electrodeposited on the FTO glass substrate as a counter electrode for low-cost dye-sensitized solar cells, *Current Applied Physics*, 2014, **14**, 1607-1611.
34. J. Wu, Q. Li, L. Fan, Z. Lan, P. Li, J. Lin and S. Hao, High-performance polypyrrole nanoparticles counter electrode for dye-sensitized solar cells, *Journal of Power Sources*, 2008, **181**, 172-176.
35. Y. F. Lin, C. T. Li and K. C. Ho, A template-free synthesis of the hierarchical hydroxymethyl PEDOT tube-coral array and its application in dye-sensitized solar cells, *Journal of Materials Chemistry A*, 2016, **4**, 384-394.
36. K. M. Lee, P. Y. Chen, C. Y. Hsu, J. H. Huang, W. H. Ho, H. C. Chen and K. C. Ho, A high-performance counter electrode based on poly(3,4-alkylenedioxythiophene) for dye-sensitized solar cells, *Journal of Power Sources*, 2009, **188**, 313-318.
37. J. Chen, K. Li, Y. Luo, X. Guo, D. Li, M. Deng, S. Huang and Q. Meng, A flexible carbon counter electrode for dye-sensitized solar cells, *Carbon*, 2009, **47**, 2704-2708.
38. H. Fang, C. Yu, T. Ma and J. Qiu, Boron-doped graphene as a high-efficiency counter electrode for dye-sensitized solar cells, *Chemical Communications*, 2014, **50**, 3328-3330.




39. S. Yun, A. Hagfeldt and T. Ma, Pt-free counter electrode for dye-sensitized solar cells with high efficiency, *Advanced Materials*, 2014, **26**, 6210-6237.
40. G. Wang, L. Zhang and J. Zhang, A review of electrode materials for electrochemical supercapacitors, *Chemical Society Reviews*, 2012, **41**, 797-828.
41. J. M. Tarascon and M. Armand, Issues and challenges facing rechargeable lithium batteries, *Nature*, 2001, **414**, 359-367.
42. S. Zhang and N. Pan, Supercapacitors performance evaluation, *Advanced Energy Materials*, 2015, **5**, 1401401-1401419.
43. R. J. B. Martin Winter, What are batteries, fuel cells, and supercapacitors?, *Chemical Reviews*, 2004, **104**, 4245-4269.
44. Y. G. Patrice Simon, Materials for electrochemical capacitors, *Nature Materials*, 2008, **7**, 845-854.
45. H. v. Helmholtz, Ueber einige Gesetze der Vertheilung elektrischer Ströme in körperlichen Leitern mit Anwendung auf die thierisch-elektrischen Versuche, *Annalen der Physik*, 1853, **165**, 211-233.
46. M. Gouy, Sur la constitution de la charge électrique à la surface d'un électrolyte, *Journal of Theoretical and Applied Physics*, 1910, **9**, 457-468.
47. D. L. Chapman, LI. A contribution to the theory of electrocapillarity, *The London, Edinburgh, and Dublin philosophical magazine and journal of science*, 1913, **25**, 475-481.
48. O. Stern, Zur theorie der elektrolytischen doppelschicht, *Berichte der Bunsengesellschaft für physikalische Chemie*, 1924, **30**, 508-516.
49. D. C. Grahame, The electrical double layer and the theory of electrocapillarity, *Chemical Reviews*, 1947, **41**, 441-501.
50. L. Pilon, H. Wang and A. d'Entremont, Recent advances in continuum modeling of interfacial and transport phenomena in electric double layer capacitors, *Journal of the Electrochemical Society*, 2015, **162**, A5158-A5178.
51. Y. Z. Zhang, Y. Wang, Y. L. Xie, T. Cheng, W. Y. Lai, H. Pang and W. Huang, Porous hollow

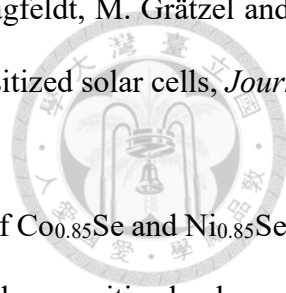
Co₃O₄ with rhombic dodecahedral structures for high-performance supercapacitors, *Nanoscale*, 2014, **6**, 14354-14359.

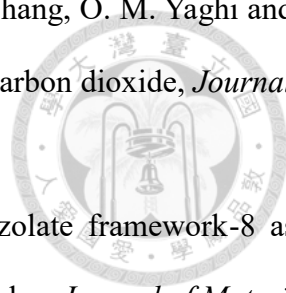


52. R. R. Salunkhe, J. Tang, Y. Kamachi, T. Nakato, J. H. Kim and Y. Yamauchi, Asymmetric supercapacitors using 3D nanoporous carbon and cobalt oxide electrodes synthesized from a single metal–organic framework, *ACS Nano*, 2015, **9**, 6288-6296.
53. L. Wang, D. Wang, X. Y. Dong, Z. J. Zhang, X. F. Pei, X. J. Chen, B. Chen and J. Jin, Layered assembly of graphene oxide and Co–Al layered double hydroxide nanosheets as electrode materials for supercapacitors, *Chemical Communications*, 2011, **47**, 3556-3558.
54. G. Y. Zhao and H. L. Li, Preparation of polyaniline nanowire arrayed electrodes for electrochemical supercapacitors, *Microporous and Mesoporous Materials*, 2008, **110**, 590-594.
55. J. C. Xing, Y. L. Zhu, M. Y. Li and Q. J. Jiao, Hierarchical mesoporous CoS₂ microspheres: morphology-controlled synthesis and their superior pseudocapacitive properties, *Electrochimica Acta*, 2014, **149**, 285-292.
56. X. Han, K. Tao, D. Wang and L. Han, Design of a porous cobalt sulfide nanosheet array on Ni foam from zeolitic imidazolate frameworks as an advanced electrode for supercapacitors, *Nanoscale*, 2018, **10**, 2735-2741.
57. X. Y. Yu, L. Yu and X. W. D. Lou, Metal sulfide hollow nanostructures for electrochemical energy storage, *Advanced Energy Materials*, 2016, **6**, 1501333-1501346.
58. K. J. Huang, J. Z. Zhang, G. W. Shi and Y. M. Liu, Hydrothermal synthesis of molybdenum disulfide nanosheets as supercapacitors electrode material, *Electrochimica Acta*, 2014, **132**, 397-403.
59. X. Y. Yu, L. Yu, H. B. Wu and X. W. D. Lou, Formation of nickel sulfide nanoframes from metal–organic frameworks with enhanced pseudocapacitive and electrocatalytic properties, *Angewandte Chemie*, 2015, **127**, 5421-5425.
60. X. Rui, H. Tan and Q. Yan, Nanostructured metal sulfides for energy storage, *Nanoscale*, 2014, **6**, 9889-9924.

- 
61. M. Ammar, S. Jiang and S. Ji, Heteropoly acid encapsulated into zeolite imidazolate framework (ZIF-67) cage as an efficient heterogeneous catalyst for Friedel–Crafts acylation, *Journal of Solid State Chemistry*, 2016, **233**, 303-310.
62. A. J. Bard and L. R. Faulkner, in *Electrochemical Methods: Fundamentals and applications*, John Wiley & Sons. Inc., 2nd edn., 2001, ch. 9, p. 341.
63. A. J. Bard and L. R. Faulkner, in *Electrochemical Methods: Fundamentals and applications*, John Wiley & Sons. Inc., 2nd edn., 2001, ch. 3, pp. 103-104.
64. M. Grätzel, Photoelectrochemical cells, *Nature*, 2001, **414**, 338-344.
65. L. Tsakalakos, J. Balch, J. Fronheiser, B. Korevaar, O. Sulima and J. Rand, Silicon nanowire solar cells, *Applied Physics Letters*, 2007, **91**, 233117-233119.
66. H. Hoppe and N. S. Sariciftci, Organic solar cells: An overview, *Journal of Materials Research*, 2004, **19**, 1924-1945.
67. A. Kongkanand, K. Tvrđy, K. Takechi, M. Kuno and P. V. Kamat, Quantum dot solar cells. Tuning photoresponse through size and shape control of CdSe–TiO₂ architecture, *Journal of the American Chemical Society*, 2008, **130**, 4007-4015.
68. H. S. Rao, W. Q. Wu, Y. Liu, Y. F. Xu, B. X. Chen, H. Y. Chen, D. B. Kuang and C. Y. Su, CdS/CdSe co-sensitized vertically aligned anatase TiO₂ nanowire arrays for efficient solar cells, *Nano Energy*, 2014, **8**, 1-8.
69. B. O'regan and M. Grätzel, A low-cost, high-efficiency solar cell based on dye-sensitized colloidal TiO₂ films, *Nature*, 1991, **353**, 737-740.
70. M. Kouhnavard, N. A. Ludin, B. V. Ghaffari, K. Sopian and S. Ikeda, Carbonaceous materials and their advances as a counter electrode in dye-sensitized solar cells: challenges and prospects, *ChemSusChem*, 2015, **8**, 1510-1533.
71. J. Mo, C. Zhang, J. Chang, H. Yang, H. Xi, D. Chen, Z. Lin, G. Lu, J. Zhang and Y. Hao, Enhanced efficiency of planar perovskite solar cells via a two-step deposition using DMF as an additive to optimize the crystal growth behavior, *Journal of Materials Chemistry A*, 2017, **5**, 13032-13038.

72. M. Freitag, J. Teuscher, Y. Saygili, X. Zhang, F. Giordano, P. Liska, J. Hua, S. M. Zakeeruddin, J.-E. Moser and M. Grätzel, Dye-sensitized solar cells for efficient power generation under ambient lighting, *Nature Photonics*, 2017, **11**, 372-379.
73. S. Peng, T. Zhang, L. Li, C. Shen, F. Cheng, M. Srinivasan, Q. Yan, S. Ramakrishna and J. Chen, 3D Cu-doped CoS porous nanosheet films as superior counterelectrodes for quantum dot-sensitized solar cells, *Nano Energy*, 2015, **16**, 163-172.
74. R. Zhou, W. Guo, R. Yu and C. Pan, Highly flexible, conductive and catalytic Pt networks as transparent counter electrodes for wearable dye-sensitized solar cells, *Journal of Materials Chemistry A*, 2015, **3**, 23028-23034.
75. Z. Zheng, J. Chen, Y. Hu, W. Wu, J. Hua and H. Tian, Efficient sinter-free nanostructure Pt counter electrode for dye-sensitized solar cells, *Journal of Materials Chemistry C*, 2014, **2**, 8497-8500.
76. D. J. Kim, J. K. Koh, C. S. Lee and J. H. Kim, Mesh-shaped nanopatterning of Pt counter electrodes for dye-sensitized solar cells with enhanced light harvesting, *Advanced Energy Materials*, 2014, **4**, 1400414-1400422.
77. G. r. Li, F. Wang, Q. w. Jiang, X. p. Gao and P. w. Shen, Carbon nanotubes with titanium nitride as a low-cost counter-electrode material for dye-sensitized solar cells, *Angewandte Chemie International Edition*, 2010, **49**, 3653-3656.
78. S. I. Cha, B. K. Koo, S. Seo and D. Y. Lee, Pt-free transparent counter electrodes for dye-sensitized solar cells prepared from carbon nanotube micro-balls, *Journal of Materials Chemistry*, 2010, **20**, 659-662.
79. M. Wu, X. Lin, A. Hagfeldt and T. Ma, Low-cost molybdenum carbide and tungsten carbide counter electrodes for dye-sensitized solar cells, *Angewandte Chemie International Edition*, 2011, **50**, 3520-3524.
80. Q. Tai, B. Chen, F. Guo, S. Xu, H. Hu, B. Sebo and X.-Z. Zhao, In situ prepared transparent polyaniline electrode and its application in bifacial dye-sensitized solar cells, *ACS Nano*, 2011, **5**, 3795-3799.

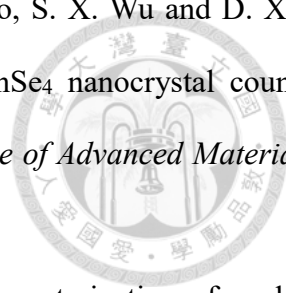
- 
81. M. Wu, X. Lin, Y. Wang, L. Wang, W. Guo, D. Qi, X. Peng, A. Hagfeldt, M. Grätzel and T. Ma, Economical Pt-free catalysts for counter electrodes of dye-sensitized solar cells, *Journal of the American Chemical Society*, 2012, **134**, 3419-3428.
82. F. Gong, H. Wang, X. Xu, G. Zhou and Z. S. Wang, In situ growth of $\text{Co}_{0.85}\text{Se}$ and $\text{Ni}_{0.85}\text{Se}$ on conductive substrates as high-performance counter electrodes for dye-sensitized solar cells, *Journal of the American Chemical Society*, 2012, **134**, 10953-10958.
83. H. J. Lee, W. Cho, E. Lim and M. Oh, One-pot synthesis of magnetic particle-embedded porous carbon composites from metal-organic frameworks and their sorption properties, *Chemical Communications*, 2014, **50**, 5476-5479.
84. G. Srinivas, V. Krungleviciute, Z. X. Guo and T. Yildirim, Exceptional CO_2 capture in a hierarchically porous carbon with simultaneous high surface area and pore volume, *Energy & Environmental Science*, 2014, **7**, 335-342.
85. F. M. Hinterholzinger, A. Ranft, J. M. Feckl, B. Rühle, T. Bein and B. V. Lotsch, One-dimensional metal-organic framework photonic crystals used as platforms for vapor sorption, *Journal of Materials Chemistry*, 2012, **22**, 10356-10362.
86. W. Chaikittisilp, K. Ariga and Y. Yamauchi, A new family of carbon materials: synthesis of MOF-derived nanoporous carbons and their promising applications, *Journal of Materials Chemistry A*, 2013, **1**, 14-19.
87. M. J. C. Ordoñez, K. J. Balkus Jr, J. P. Ferraris and I. H. Musselman, Molecular sieving realized with ZIF-8/Matrimid[®] mixed-matrix membranes, *Journal of Membrane Science*, 2010, **361**, 28-37.
88. Y. Fu, D. Sun, Y. Chen, R. Huang, Z. Ding, X. Fu and Z. Li, An amine-functionalized titanium metal-organic framework photocatalyst with visible-light-induced activity for CO_2 reduction, *Angewandte Chemie*, 2012, **124**, 3420-3423.
89. M. Sabo, A. Henschel, H. Fröde, E. Klemm and S. Kaskel, Solution infiltration of palladium into MOF-5: synthesis, physisorption and catalytic properties, *Journal of Materials Chemistry*, 2007, **17**, 3827-3832.

- 
90. N. Kornienko, Y. Zhao, C. S. Kley, C. Zhu, D. Kim, S. Lin, C. J. Chang, O. M. Yaghi and P. Yang, Metal–organic frameworks for electrocatalytic reduction of carbon dioxide, *Journal of the American Chemical Society*, 2015, **137**, 14129-14135.
91. S. Liu, Z. Xiang, Z. Hu, X. Zheng and D. Cao, Zeolitic imidazolate framework-8 as a luminescent material for the sensing of metal ions and small molecules, *Journal of Materials Chemistry*, 2011, **21**, 6649-6653.
92. P. Zhang, F. Sun, Z. Shen and D. Cao, ZIF-derived porous carbon: a promising supercapacitor electrode material, *Journal of Materials Chemistry A*, 2014, **2**, 12873-12880.
93. R. R. Salunkhe, M. B. Zakaria, Y. Kamachi, S. M. Alshehri, T. Ahamad, N. L. Torad, S. X. Dou, J. H. Kim and Y. Yamauchi, Fabrication of asymmetric supercapacitors based on coordination polymer derived nanoporous materials, *Electrochimica Acta*, 2015, **183**, 94-99.
94. J. S. Li, S. L. Li, Y. J. Tang, K. Li, L. Zhou, N. Kong, Y. Q. Lan, J. C. Bao and Z. H. Dai, Heteroatoms ternary-doped porous carbons derived from MOFs as metal-free electrocatalysts for oxygen reduction reaction, *Scientific Reports*, 2014, **4**, 5130.
95. S. Jun, S. H. Joo, R. Ryoo, M. Kruk, M. Jaroniec, Z. Liu, T. Ohsuna and O. Terasaki, Synthesis of new, nanoporous carbon with hexagonally ordered mesostructure, *Journal of the American Chemical Society*, 2000, **122**, 10712-10713.
96. A. H. Lu, W. Schmidt, B. Spliethoff and F. SCHÜTH, Synthesis of ordered mesoporous carbon with bimodal pore system and high pore volume, *Advanced Materials*, 2003, **15**, 1602-1606.
97. M. Jiang, X. Cao, D. Zhu, Y. Duan and J. Zhang, Hierarchically porous N-doped carbon derived from ZIF-8 nanocomposites for electrochemical applications, *Electrochimica Acta*, 2016, **196**, 699-707.
98. X. Meng, C. Yu, X. Song, Y. Liu, S. Liang, Z. Liu, C. Hao and J. Qiu, Nitrogen-doped graphene nanoribbons with surface enriched active sites and enhanced performance for dye-sensitized solar cells, *Advanced Energy Materials*, 2015, **5**, 1500180-1500188.
99. S. Hou, X. Cai, H. Wu, X. Yu, M. Peng, K. Yan and D. Zou, Nitrogen-doped graphene for dye-sensitized solar cells and the role of nitrogen states in triiodide reduction, *Energy &*

Environmental Science, 2013, **6**, 3356-3362.

100. M. Y. Yen, C. K. Hsieh, C. C. Teng, M. C. Hsiao, P. I. Liu, C. C. M. Ma, M. C. Tsai, C. H. Tsai, Y. R. Lin and T. Y. Chou, Metal-free, nitrogen-doped graphene used as a novel catalyst for dye-sensitized solar cell counter electrodes, *RSC Advances*, 2012, **2**, 2725-2728.
101. Y. Yang, L. Ge, V. Rudolph and Z. Zhu, In situ synthesis of zeolitic imidazolate frameworks/carbon nanotube composites with enhanced CO₂ adsorption, *Dalton Transactions*, 2014, **43**, 7028-7036.
102. Q. Lai, Y. Zhao, Y. Liang, J. He and J. Chen, In situ confinement pyrolysis transformation of ZIF-8 to nitrogen-enriched meso-microporous carbon frameworks for oxygen reduction, *Advanced Functional Materials*, 2016, **26**, 8334-8344.
103. R. R. Salunkhe, J. Tang, N. Kobayashi, J. Kim, Y. Ide, S. Tominaka, J. H. Kim and Y. Yamauchi, Ultrahigh performance supercapacitors utilizing core-shell nanoarchitectures from a metal-organic framework-derived nanoporous carbon and a conducting polymer, *Chemical Science*, 2016, **7**, 5704-5713.
104. R. R. Salunkhe, Y. V. Kaneti, J. Kim, J. H. Kim and Y. Yamauchi, Nanoarchitectures for metal-organic framework-derived nanoporous carbons toward supercapacitor applications, *Accounts of Chemical Research*, 2016, **49**, 2796-2806.
105. J. Kim, C. Young, J. Lee, M.-S. Park, M. Shahabuddin, Y. Yamauchi and J. H. Kim, CNTs grown on nanoporous carbon from zeolitic imidazolate frameworks for supercapacitors, *Chemical Communications*, 2016, **52**, 13016-13019.
106. R. R. Salunkhe, C. Young, J. Tang, T. Takei, Y. Ide, N. Kobayashi and Y. Yamauchi, A high-performance supercapacitor cell based on ZIF-8-derived nanoporous carbon using an organic electrolyte, *Chemical Communications*, 2016, **52**, 4764-4767.
107. X. Sun, Y. Li, J. Dou, D. Shen and M. Wei, Metal-organic frameworks derived carbon as a high-efficiency counter electrode for dye-sensitized solar cells, *Journal of Power Sources*, 2016, **322**, 93-98.
108. H. Jing, X. Song, S. Ren, Y. Shi, Y. An, Y. Yang, M. Feng, S. Ma and C. Hao, ZIF-67 derived

- nanostructures of Co/CoO and Co@N-doped graphitic carbon as counter electrode for highly efficient dye-sensitized solar cells, *Electrochimica Acta*, 2016, **213**, 252-259.
109. X. Cui, Z. Xie and Y. Wang, Novel CoS₂ embedded carbon nanocages by direct sulfurizing metal-organic frameworks for dye-sensitized solar cells, *Nanoscale*, 2016, **8**, 11984-11992.
110. S. Yun, A. Hagfeldt and T. Ma, Pt-Free Counter Electrode for Dye-Sensitized Solar Cells with High Efficiency, *Advanced Materials*, 2014, **26**, 6210-6237.
111. C. T. Li, C. P. Lee, I. T. Chiu, R. Vittal, Y. J. Huang, T. Y. Chen, H. W. Pang, J. T. Lin and K. C. Ho, Hierarchical TiO_{1.1}Se_{0.9}-wrapped carbon cloth as the TCO-free and Pt-free counter electrode for iodide-based and cobalt-based dye-sensitized solar cells, *Journal of Materials Chemistry A*, 2017, **5**, 14079-14091.
112. C. T. Li, Y. L. Tsai and K. C. Ho, Earth abundant silicon composites as the electrocatalytic counter electrodes for dye-sensitized solar cells, *ACS Applied Materials & Interfaces*, 2016, **8**, 7037-7046.
113. L. T. L. Lee, J. He, B. Wang, Y. Ma, K. Y. Wong, Q. Li, X. Xiao and T. Chen, Few-layer MoSe₂ possessing high catalytic activity towards iodide/tri-iodide redox shuttles, *Scientific Reports*, 2014, **4**, 4063-4069.
114. L. Zhu, T. S. Park, K. Y. Cho and W. C. Oh, Facile hydrothermal synthesis of graphene-ZnSe electro-catalytic electrodes for dye sensitized solar cells, *Fullerenes, Nanotubes and Carbon Nanostructures*, 2016, **24**, 324-331.
115. S. H. Hsu, C. T. Li, H. T. Chien, R. R. Salunkhe, N. Suzuki, Y. Yamauchi, K. C. Ho and K. C. W. Wu, Platinum-free counter electrode comprised of metal-organic-framework (MOF)-derived cobalt sulfide nanoparticles for efficient dye-sensitized solar cells (DSSCs), *Scientific Reports*, 2014, **4**, 6983-6988.
116. C. T. Li, H. Y. Chang, Y. Y. Li, Y. J. Huang, Y. L. Tsai, R. Vittal, Y. J. Sheng and K. C. Ho, Electrocatalytic zinc composites as the efficient counter electrodes of dye-sensitized solar cells: study on the electrochemical performances and density functional theory calculations, *ACS Applied Materials & Interfaces*, 2015, **7**, 28254-28263.

- 
117. S. J. Yuan, Z. J. Zhou, Z. L. Hou, W. H. Zhou, R. Y. Yao, Y. Zhao, S. X. Wu and D. Xue, Enhanced efficiency of dye-sensitized solar cells using $\text{Cu}_2\text{ZnSnSe}_4$ nanocrystal counter electrode prepared by in situ synthesis and film deposition, *Science of Advanced Materials*, 2013, **5**, 927-932.
118. X. Wu, M. N. Shahrak, B. Yuan and S. Deng, Synthesis and characterization of zeolitic imidazolate framework ZIF-7 for CO_2 and CH_4 separation, *Microporous and Mesoporous Materials*, 2014, **190**, 189-196.
119. J. Xie, N. Yan, F. Liu, Z. Qu, S. Yang and P. Liu, CO_2 adsorption performance of ZIF-7 and its endurance in flue gas components, *Frontiers of Environmental Science & Engineering*, 2014, **8**, 162-168.
120. W. Morris, N. He, K. G. Ray, P. Klonowski, H. Furukawa, I. N. Daniels, Y. A. Houndonougbo, M. Asta, O. M. Yaghi and B. B. Laird, A combined experimental-computational study on the effect of topology on carbon dioxide adsorption in zeolitic imidazolate frameworks, *The Journal of Physical Chemistry C*, 2012, **116**, 24084-24090.
121. J. D. Roy-Mayhew, D. J. Bozym, C. Punckt and I. A. Aksay, Functionalized graphene as a catalytic counter electrode in dye-sensitized solar cells, *ACS Nano*, 2010, **4**, 6203-6211.
122. L. Lai, J. R. Potts, D. Zhan, L. Wang, C. K. Poh, C. Tang, H. Gong, Z. Shen, J. Lin and R. S. Ruoff, Exploration of the active center structure of nitrogen-doped graphene-based catalysts for oxygen reduction reaction, *Energy & Environmental Science*, 2012, **5**, 7936-7942.
123. M. H. Yeh, L. Y. Lin, C. P. Lee, H. Y. Wei, C. Y. Chen, C. G. Wu, R. Vittal and K. C. Ho, A composite catalytic film of PEDOT: PSS/TiN-NPs on a flexible counter-electrode substrate for a dye-sensitized solar cell, *Journal of Materials Chemistry*, 2011, **21**, 19021-19029.
124. Y. Zhu, S. Murali, M. D. Stoller, K. Ganesh, W. Cai, P. J. Ferreira, A. Pirkle, R. M. Wallace, K. A. Cychoz and M. Thommes, Carbon-based supercapacitors produced by activation of graphene, *Science*, 2011, **332**, 1537-1541.
125. Z. Yu, L. Tetard, L. Zhai and J. Thomas, Supercapacitor electrode materials: nanostructures from 0 to 3 dimensions, *Energy & Environmental Science*, 2015, **8**, 702-730.

126. E. Lim, C. Jo and J. Lee, A mini review of designed mesoporous materials for energy-storage applications: from electric double-layer capacitors to hybrid supercapacitors, *Nanoscale*, 2016, **8**, 7827-7833.
127. L. L. Zhang and X. Zhao, Carbon-based materials as supercapacitor electrodes, *Chemical Society Reviews*, 2009, **38**, 2520-2531.
128. Z. Jiang, W. Lu, Z. Li, K. H. Ho, X. Li, X. Jiao and D. Chen, Synthesis of amorphous cobalt sulfide polyhedral nanocages for high performance supercapacitors, *Journal of Materials Chemistry A*, 2014, **2**, 8603-8606.
129. G. Yilmaz, K. M. Yam, C. Zhang, H. J. Fan and G. W. Ho, In situ transformation of MOFs into layered double hydroxide embedded metal sulfides for improved electrocatalytic and supercapacitive performance, *Advanced Materials*, 2017, **29**, 1606814-1606821.
130. Y. Wang, B. Chen, Y. Zhang, L. Fu, Y. Zhu, L. Zhang and Y. Wu, ZIF-8@MWCNT-derived carbon composite as electrode of high performance for supercapacitor, *Electrochimica Acta*, 2016, **213**, 260-269.
131. Y. Liu, G. Li, Z. Chen and X. Peng, CNT-threaded N-doped porous carbon film as binder-free electrode for high-capacity supercapacitor and Li-S battery, *Journal of Materials Chemistry A*, 2017, **5**, 9775-9784.
132. P. Wu, S. Cheng, M. Yao, L. Yang, Y. Zhu, P. Liu, O. Xing, J. Zhou, M. Wang and H. Luo, A low-cost, self-standing NiCo₂O₄@CNT/CNT multilayer electrode for flexible asymmetric solid-state supercapacitors, *Advanced Functional Materials*, 2017, **27**, 1702160-1702168.
133. Z. Tang, C. h. Tang and H. Gong, A high energy density asymmetric supercapacitor from nano-architected Ni(OH)₂/carbon nanotube electrodes, *Advanced Functional Materials*, 2012, **22**, 1272-1278.
134. X. Wang, X. Han, M. Lim, N. Singh, C. L. Gan, M. Jan and P. S. Lee, Nickel cobalt oxide-single wall carbon nanotube composite material for superior cycling stability and high-performance supercapacitor application, *The Journal of Physical Chemistry C*, 2012, **116**, 12448-12454.

135. R. Wu, X. Qian, X. Rui, H. Liu, B. Yadian, K. Zhou, J. Wei, Q. Yan, X. Q. Feng and Y. Long, Zeolitic imidazolate framework 67-derived high symmetric porous Co_3O_4 hollow dodecahedra with highly enhanced lithium storage capability, *Small*, 2014, **10**, 1932-1938.
136. D. Song, Q. Wang, Y. Wang, Y. Wang, Y. Han, L. Li, G. Liu, L. Jiao and H. Yuan, Liquid phase chemical synthesis of Co-S microspheres with novel structure and their electrochemical properties, *Journal of Power Sources*, 2010, **195**, 7462-7465.
137. Q. Wang, F. Gao, B. Xu, F. Cai, F. Zhan, F. Gao and Q. Wang, ZIF-67 derived amorphous CoNi_2S_4 nanocages with nanosheet arrays on the shell for a high-performance asymmetric supercapacitor, *Chemical Engineering Journal*, 2017, **327**, 387-396.
138. S. Zhang, D. Li, S. Chen, X. Yang, X. Zhao, Q. Zhao, S. Komarneni and D. Yang, Highly stable supercapacitors with MOF-derived Co_9S_8 /carbon electrodes for high rate electrochemical energy storage, *Journal of Materials Chemistry A*, 2017, **5**, 12453-12461.
139. S. Liu, M. Tong, G. Liu, X. Zhang, Z. Wang, G. Wang, W. Cai, H. Zhang and H. Zhao, S, N-containing Co-MOF derived Co_9S_8 @S, N-doped carbon materials as efficient oxygen electrocatalysts and supercapacitor electrode materials, *Inorganic Chemistry Frontiers*, 2017, **4**, 491-498.
140. F. Tao, Y. Q. Zhao, G.-Q. Zhang and H. L. Li, Electrochemical characterization on cobalt sulfide for electrochemical supercapacitors, *Electrochemistry Communications*, 2007, **9**, 1282-1287.
141. B. Qu, Y. Chen, M. Zhang, L. Hu, D. Lei, B. Lu, Q. Li, Y. Wang, L. Chen and T. Wang, β -Cobalt sulfide nanoparticles decorated graphene composite electrodes for high capacity and power supercapacitors, *Nanoscale*, 2012, **4**, 7810-7816.
142. A. Mohammadi, N. Arsalani, A. G. Tabrizi, S. E. Moosavifard, Z. Naqshbandi and L. S. Ghadimi, Engineering rGO-CNT wrapped Co_3S_4 nanocomposites for high-performance asymmetric supercapacitors, *Chemical Engineering Journal*, 2018, **334**, 66-80.
143. J. P. C. Trigueiro, R. L. Lavall and G. G. Silva, Nanocomposites of graphene nanosheets/multiwalled carbon nanotubes as electrodes for in-plane supercapacitors,

Electrochimica Acta, 2016, **187**, 312-322.

144. A. Burke and M. Miller, Testing of electrochemical capacitors: Capacitance, resistance, energy density, and power capability, *Electrochimica Acta*, 2010, **55**, 7538-7548.
145. P. Zhang, B. Y. Guan, L. Yu and X. W. D. Lou, Formation of double-shelled zinc–cobalt sulfide dodecahedral cages from bimetallic zeolitic imidazolate frameworks for hybrid supercapacitors, *Angewandte Chemie International Edition*, 2017, **56**, 7141-7145.
146. H. Hu, B. Y. Guan and X. W. D. Lou, Construction of complex CoS hollow structures with enhanced electrochemical properties for hybrid supercapacitors, *Chem*, 2016, **1**, 102-113.
147. F. Cao, M. Zhao, Y. Yu, B. Chen, Y. Huang, J. Yang, X. Cao, Q. Lu, X. Zhang and Z. Zhang, Synthesis of two-dimensional CoS_{1.097}/nitrogen-doped carbon nanocomposites using metal–organic framework nanosheets as precursors for supercapacitor application, *Journal of the American Chemical Society*, 2016, **138**, 6924-6927.
148. Y. Wang, B. Chen, Z. Chang, X. Wang, F. Wang, L. Zhang, Y. Zhu, L. Fu and Y. Wu, Enhancing performance of sandwich-like cobalt sulfide and carbon for quasi-solid-state hybrid electrochemical capacitors, *Journal of Materials Chemistry A*, 2017, **5**, 8981-8988.
149. C. Yuan, L. Shen, F. Zhang, X. Lu, D. Li and X. Zhang, Interface-hydrothermal synthesis and electrochemical properties of CoS_x nanodots/poly (sodium-4-styrene sulfonate) functionalized multi-walled carbon nanotubes nanocomposite, *Journal of Colloid and Interface Science*, 2010, **349**, 181-185.
150. C.-Y. Chen, Z.-Y. Shih, Z. Yang and H.-T. Chang, Carbon nanotubes/cobalt sulfide composites as potential high-rate and high-efficiency supercapacitors, *Journal of Power Sources*, 2012, **215**, 43-47.
151. K. Dai, L. Lu, C. Liang, L. Geng and G. Zhu, Large-scale synthesis of cobalt sulfide/carbon nanotube hybrid and its excellent electrochemical capacitance performance, *Materials Letters*, 2016, **176**, 42-45.
152. K. Dai, D. Li, L. Lu, Q. Liu, J. Lv and G. Zhu, Facile synthesis of a reduced graphene oxide/cobalt sulfide hybrid and its electrochemical capacitance performance, *RSC Advances*,

2014, **4**, 29216-29222.

153. T. Yao, Y. Li, D. Liu, Y. Gu, S. Qin, X. Guo, H. Guo, Y. Ding, Q. Liu and Q. Chen, High-performance free-standing capacitor electrodes of multilayered Co_9S_8 plates wrapped by carbonized poly (3, 4-ethylenedioxythiophene): poly (styrene sulfonate)/reduced graphene oxide, *Journal of Power Sources*, 2018, **379**, 167-173.
154. X. Song, L. Tan, X. Wang, L. Zhu, X. Yi and Q. Dong, Synthesis of $\text{CoS}@r\text{GO}$ composites with excellent electrochemical performance for supercapacitors, *Journal of Electroanalytical Chemistry*, 2017, **794**, 132-138.
155. Q. Wang, L. Jiao, H. Du, Y. Si, Y. Wang and H. Yuan, Co_3S_4 hollow nanospheres grown on graphene as advanced electrode materials for supercapacitors, *Journal of Materials Chemistry*, 2012, **22**, 21387-21391.
156. L. Xu and Y. Lu, One-step synthesis of a cobalt sulfide/reduced graphene oxide composite used as an electrode material for supercapacitors, *RSC Advances*, 2015, **5**, 67518-67523.
157. S. J. Patil, J. H. Kim and D. W. Lee, Graphene-nanosheet wrapped cobalt sulphide as a binder free hybrid electrode for asymmetric solid-state supercapacitor, *Journal of Power Sources*, 2017, **342**, 652-665.
158. M. Jana, P. Samanta, N. C. Murmu, N. H. Kim, T. Kuila and J. H. Lee, Development of cobalt sulfide-graphene composite for supercapacitor applications, *Composites Research*, 2016, **29**, 167-172.
159. M. Jana, S. Saha, P. Samanta, N. C. Murmu, N. H. Kim, T. Kuila and J. H. Lee, Development of high energy density supercapacitor through hydrothermal synthesis of RGO/nano-structured cobalt sulphide composites, *Nanotechnology*, 2015, **26**, 75402-75415.
160. H. Heydari and M. B. Gholivand, Polyaniline/reduced graphene oxide–cobalt sulfide ternary composite for high-performance supercapacitors, *Journal of Materials Science: Materials in Electronics*, 2017, **28**, 3607-3615.
161. J. Shi, X. Li, G. He, L. Zhang and M. Li, Electrodeposition of high-capacitance 3D $\text{CoS}/\text{graphene}$ nanosheets on nickel foam for high-performance aqueous asymmetric

- supercapacitors, *Journal of Materials Chemistry A*, 2015, **3**, 20619-20626.
162. X. Meng, J. Deng, J. Zhu, H. Bi, E. Kan and X. Wang, Cobalt sulfide/graphene composite hydrogel as electrode for high-performance pseudocapacitors, *Scientific Reports*, 2016, **6**, 21717-21725.
163. R. Ramachandran, S. Felix, M. Saranya, C. Santhosh, V. Velmurugan, B. P. C. Ragupathy, S. K. Jeong and A. N. Grace, Synthesis of cobalt sulfide–graphene (CoS/G) nanocomposites for supercapacitor applications, *IEEE Transactions on Nanotechnology*, 2013, **12**, 985-990.
164. T. W. Lin, C. S. Dai, T. T. Tasi, S. W. Chou, J. Y. Lin and H. H. Shen, High-performance asymmetric supercapacitor based on Co₉S₈/3D graphene composite and graphene hydrogel, *Chemical Engineering Journal*, 2015, **279**, 241-249.
165. Y. Wang, J. Tang, B. Kong, D. Jia, Y. Wang, T. An, L. Zhang and G. Zheng, Freestanding 3D graphene/cobalt sulfide composites for supercapacitors and hydrogen evolution reaction, *RSC Advances*, 2015, **5**, 6886-6891.
166. A. N. Grace, R. Ramachandran, M. Vinoba, S. Y. Choi, D. H. Chu, Y. Yoon, S. C. Nam and S. K. Jeong, Facile synthesis and electrochemical properties of Co₃S₄-nitrogen-doped graphene nanocomposites for supercapacitor applications, *Electroanalysis*, 2014, **26**, 199-208.
167. D. Jiang, Q. Xu, S. Meng, C. Xia and M. Chen, Construction of cobalt sulfide/graphitic carbon nitride hybrid nanosheet composites for high performance supercapacitor electrodes, *Journal of Alloys and Compounds*, 2017, **706**, 41-47.
168. Y. Zhao, Z. Song, X. Li, Q. Sun, N. Cheng, S. Lawes and X. Sun, Metal organic frameworks for energy storage and conversion, *Energy Storage Materials*, 2016, **2**, 35-62.
169. W. Xia, A. Mahmood, R. Zou and Q. Xu, Metal–organic frameworks and their derived nanostructures for electrochemical energy storage and conversion, *Energy & Environmental Science*, 2015, **8**, 1837-1866.